REALIZATION OF TWO DIMENSIONAL MEMS BASED DISPLAYS USING POLYMER COMPOSITE MICRO-SCANNERS INTEGRATED WITH ONE DIMENSIONAL POLYMER LED ARRAYS

by
Yiğit Dağhan Gökdel
B.S., in Electrical & Electronics Eng., Bilkent University, 2004
M.S., in Electrical & Electronics Eng., Boğaziçi University, 2007

Submitted to the Institute for Graduate Studies in
Science and Engineering in partial fulfillment of
the requirements for the degree of
Doctor of Philosophy

Graduate Program in Electrical and Electronics Engineering
Boğaziçi University
2011

ACKNOWLEDGEMENTS

This work would not have been possible without the help and influence of many people some of which I would like to mention here.

First of all, I owe my deepest gratitude to my thesis supervisor, Prof. Arda Deniz Yalçınkaya for accepting me as his student and teaching me on almost everything in the course of my PhD studies. His intuition, keen perception and vast knowledge guided my research to a fruitful and productive conclusion.

I would like to express my utmost gratitude to my former supervisor Prof. Günhan Dündar for giving me the opportunity to be a part of this research group in the first place. His manners, his knowledge and his wisdom on just about everything makes him a true role model for every student in Beta Lab including me.

I was also really fortunate to have the opportunity to work with Prof. Şenol Mutlu. His expertise on micro-fabrication techniques, his countless bright and inspiring ideas helped me to complete this thesis work. Being a true gentleman, he taught me the meaning of hard work and professionalism.

I would like to particulary thank Prof. Hakan Urey who has made significant contributions to my research. Being one of the most important researchers on the field, he always pointed me to the right direction and shared his invaluable ideas which have been extremely important for me and for my development.

I would like to sincerely thank Prof. Haluk Külah for kindly taking part in my thesis jury and sharing his ideas on my research.

I would like to also thank Baykal Sarioglu for countless reasons. Most importantly, he was like a brother to me throughout all my graduate studies in Bogazici University in the past 7 years. His sophisticated and pleasant character, his intelligence and

comradeship helped me to survive in this period of my life.

I am indebted to many of my colleagues in Beta Lab for their continuous support and friendship in all those years. I would like to thank Okan Z. Batur for his kind heart and friendship. He was always generously helped me. I also thank to Orhan Mert with whom I share many of the same passions for life and sports, Iskender Haydaroglu who always surprises me with his ideas and who introduced me to a new way of thinking on sports and biology, Melih Akcakaya who help me tremendously on my research and on my assistant duties during the preparations of my thesis and whom I always enjoyed our conversations, Gurkan Sonmez who is my sharp-witted officemate for the past two years and who, together with Melih, provided me with the latest movies and computer games.

My special thank goes also to my cheerful research partner Betul Kucukakarsu Usta with whom I worked four countless hours in clean room and in characterization lab, to Umut Cindemir who worked on the LED driver ICs in our projects and helped me to keep my sanity during painful working hours thanks to his sense of humor and to Selim Ölçer for helping me with great patience in pcb fabrication.

I am also grateful to my furry, bravehearted and playful friend Achilles for being literally by my side throughout all those long hours work and sleepless nights.

I would like to also thank to my parents-in-law, Guzin and Engin Kasarci and my sister-in-law Busra Kasarci for supporting me in every way they can.

I owe my deepest gratitude to my beloved family, Şule, Erkan and Damla Gokdel. I always knew that they were there to help me and always felt their love. Without them, it would be impossible to complete this work.

Finally, I would like to express my gratitude and my love to my wife, Merve for her continuous support, understanding and compassion. Her love is the most meaningful and important thing in my life.

ABSTRACT

REALIZATION OF TWO DIMENSIONAL MEMS BASED DISPLAYS USING POLYMER COMPOSITE MICRO-SCANNERS INTEGRATED WITH ONE DIMENSIONAL POLYMER LED ARRAYS

A novel type of displays are realized by hybrid and monolithic integration of optoelectronic devices with micro electro mechanical systems (MEMS). MEMS platform, with mechanical quality factor (20-50 in air) enhanced displacement, defines the refresh rate of the two-dimensional display. Vertical resolution of the display is increased by operating the MEMS device at its fundamental resonance mode. Actuation of this mechanical mode is accomplished by generating a time and frequency dependant electromagnetic force or torque on the MEMS platform. Horizontal scan of the display is performed by modulation of a one dimensional array of light emitting diodes. In effect, a LED emitter moving in the direction of vertical scan, generates a virtual pixel whose brightness is electronically modulated. First prototype which is realized in this thesis work is an inorganic LED integrated FR4 display, where modulation of light sources is synchronized with FR4 movement. Performance metrics of this prototype with LED driving integrated circuits on, are 3.4 mm of peak resonant displacement, two orders of magnitude suppression of the second parasitic mode. The prototype, composed of all polymer materials utilizes ITO - PEDOT:PSS - MEH-PPV and FR4. Magnetic actuator is integrated with the polymer LED devices and two-dimensional display functionality is demonstrated. Realized display has 20 $\times$ 7 resolution with a screen size of 9 mm $\times$ 3.4 mm. Polymer LED pixels can supply a brightness level of 0.3 cd/m^2 and an efficiency of %1.

ÖZET

TEK BOYUTLU POLİMER LED DİZİLERİ İLE TÜMLEŞTİRİLMİŞ KOMPOZİT POLİMER MİKRO TARAYICILAR KULLANILARAK OLUŞTURULAN MEMS TABANLI EKRANLAR

Polimer bazlı mikro elektro mekanik sistemler (MEMS) ile optoelektronik aygıtların monolitik ve hibrid yöntemler ile tümleştirilmesi sonucunda yeni nesil görüntü cihazları elde edilmiştir. Bu iki boyutlu görüntü cihazlarında yavaş tarama işlevi MEMS yapının tazeleme frekansındaki yerdeğiştirmesi ile gerçeklenmiştir. Ekranın çözünürlüğünü artırabilmek için yapının rezonansında oluşan yerdeğiştirme kullanılmış ve 20-50 civarındaki kalite faktörünün getirdiği mekanik yükseltmeden faydalanılmıştır. Yapının mekanik yerdeğiştirmesi, sürücü elektrik akımının kontrol ettiği bir elektro bobinin oluşturduğu elektromanyetik kuvvet ile sağlanmıştır. Ekranın diğer ekseni ise ışık kaynaklarından (inorganik LED kırmıkları veya polimer LED dizini) oluşan bir satırın elektronik olarak modüle edilmesi ile oluşturulmuştur. Böylelikle bir LED aygıtı MEMS cihazının hareket doğrultusunda elektronik olarak parlaklığı kontrol edilebilen sanal pikseller oluşturur. Tez kapsamında, ilk olarak inorganik LED kırmıkları ile FR4 bazlı elektromekanik sistemlerin hibrid tümleştirilmesi sonucu, mekanik hareketi elektronik modülasyon ile senkronize olan iki boyutlu ekran geliştiril- miştir. Rezonans halinde tepe yerdeğiştirmesi 3.4 mm seviyesinde, ikincil parazitik modu iki mertebe ve üstünde bastırabilme kabiliyetine sahip FR4 yapılar elektronik sürücü devre ile birlikte gerçeklenmiştir. Tezin ilerleyen bölümünde, tamamen polimer malzemelerden üretilen ekran prototipi, ITO-PEDOT:PSS-MEH-PPV ve FR4 malzemeleri kullanılarak oluşturulmuş, manyetik tahrik mekanizması ile polimer LED aygıtları entegre edilmiş ve iki-boyutlu ekran kullanımında işlevselliği kanıtlanmıştır. Gerçeklenen ekran 20×7 çözünürlüğünde, 9 mm $\times$ 3.4 mm büyüklüğünde olup, polimer ışık kaynaklarının 0.3 cd/m^2 civarında tepe parlaklık, %1 verimlilik ile çalıştığı gözlenmiştir.

TABLE OF CONTENTS

ACKNOWLEDGEMENTS . . . iii
ABSTRACT . . . v
ÖZET . . . vi
LIST OF FIGURES . . . x
LIST OF TABLES . . . xviii
LIST OF SYMBOLS . . . xix
LIST OF ABBREVIATIONS . . . xxi
1. INTRODUCTION . . . 1
1.1. History of Projection Displays and Related Work . . . 1
1.2. Summary and Contribution of the Thesis . . . 5
1.3. Organization of the Thesis . . . 7
2. THEORETICAL FOUNDATIONS . . . 9
2.1. Performance Criteria of Scanner Based Display Systems and Design Considerations . . . 9
2.2. Micromechanics of Mechanical Scanners . . . 13
2.2.1. Cantilever Beams . . . 14
2.2.2. Fixed-Free Beams Connected in Parallel With a Concentrated End-Loading . . . 22
2.2.3. Double-Clamped Beam With a Central Mass . . . 23
2.3. Structural Materials Used in Thesis Work . . . 25
2.4. Magnetic Actuation . . . 27
2.4.1. Magnetization and Hysteresis Curve . . . 29
2.5. Lumped-Element Modeling & Equivalent Magnetic Circuit . . . 31
2.5.1. Magnetic Actuation of Stainless Steel Scanners . . . 34
2.5.2. Magnetic Actuation of FR4 Scanners . . . 38
3. LED INTEGRATED MEMS DISPLAYS . . . 41
3.1. Operation Principles of FR4 Scanner-Based Displays . . . 43
3.2. Solid State LED Integrated FR4 Scanners . . . 44
3.2.1. Design of the Proposed Structure . . . 44

3.2.2. Solid-State LEDs and the LED Driving Scheme 48
3.2.3. Position Sensor and Modulation 54
3.2.4. Realization of Solid-State LED Integrated FR4 Scanners 56
3.2.5. Power Considerations 59
3.2.6. Characterization and Experimental Results 61
3.2.7. Concluding Remarks and Discussion on Solid-State LED Array Integrated FR4 Scanner Based Displays 64
3.3. Polymer LED Integrated FR4 Scanner-Based Display 65
3.3.1. Design and Operation Principles of PLED integrated FR4 scanners 66
3.3.2. Polymer LEDs 66
3.3.3. Fabrication of PLEDs and PLED Integrated FR4 Scanners . . . 68
3.3.4. Characterization and Experimental Results of PLED Array Integrated FR4 Scanner 75
3.3.5. Concluding Remarks and Discussion on Scanner Based All-Polymer Display 79
4. STAINLESS STEEL TORSIONAL RASTER-SCANNING DISPLAYS . . . 80
4.1. Design and Fabrication of Two-Axis Micromachined Steel Scanners . . 80
4.1.1. Device Operation 80
4.1.2. Fabrication of Stainless Steel Scanners 84
4.1.3. Test and Characterization Results 88
4.1.4. Simultaneous Actuation Control 92
4.1.5. Modulation of the Laser Source 93
4.1.6. Concluding Remarks on Two-Axis Micromachined Steel Scanners 94
4.2. Performance Enhancement in Micro-scanners Through Depth-Profile Shaping 95
4.2.1. Self-Terminating Fabrication Process of Stainless Steel Scanners 97
4.2.2. Proposed Improvement in Device Operation 102
4.2.3. Experimental Results and Measurement 105
4.2.4. Concluding Remarks on Self-Terminating Fabrication Method . 107
5. CONCLUSIONS AND FUTURE WORK 109
APPENDIX A: FPGA Code 114
APPENDIX B: List of Publications 118

B.1. Journal Publications 118
B.2. Conference Publications 118
REFERENCES 120

LIST OF FIGURES

Figure 1.1. Kinescope developed in 1929 by V. Zworykin. After [15]. 1

Figure 1.2. (a) Schematic drawing of the Eidophor system. (b) Operation principle of the Eidophor. After [13] and [17]. 2

Figure 1.3. Top view and cross-section of mirror matrix tube. After [19]. . . . 3

Figure 1.4. Simplified view of the cross-section of DMD. After [13]. 4

Figure 1.5. Two pixels of digital micromirror device. After [13]. 4

Figure 1.6. 2D MEMS scanner which is used in laser PicoProjector of Microvision Inc. After [29]. 5

Figure 2.1. Torsional scanner of diameter of D with a mechanical scan angle of θ_{mech}. 10

Figure 2.2. Types of flexural beams used. (a) fixed-free beams connected in parallel with a concentrated end-loading. (b) the double-clamped beam with a central mass. 14

Figure 2.3. Displacement of a cantilever beam experiencing a point force or torque. 15

Figure 2.4. Simple harmonic oscillator model of 1D MEMS actuator. 18

Figure 2.5. (a) Pole plot for an under-damped second-order system. (b) Second-order under-damped time domain responses for different damping ratio values. 21

Figure 2.6. Frequency response of a generic fixed-free beam. 21

Figure 2.7. Five fundamental vibration modes for the torsional scanner [51]. . 24

Figure 2.8. Ferromagnetic domains. No magnetic field is applied on the left. External fields orient the domains on the right. After [72]. 30

Figure 2.9. Magnetization hysteresis curve of (a) soft magnet and (b) permanent magnet. 30

Figure 2.10. (a) Schematic drawing of magnetic actuation setup (b) magnetic circuit equivalent (c) electro-mechanical analogy. 31

Figure 2.11. Schematic representation of forces and torques under non-uniform H-field in torsional scanners. 35

Figure 2.12. Schematic illustration of magnetic actuator mechanism used in FR4 scanners. 39

Figure 2.13. Different types of magnets used in the design process. After [79]. . 39

Figure 3.1. 1D array of LEDs creating virtual pixels due to MEMS-actuation in a direction perpendicular to electronic modulation axis. 42

Figure 3.2. Conceptual drawing of the proposed solid-state LED integrated FR4 display. 45

Figure 3.3. Automatized excel sheet used for designing the proposed structures. 46

Figure 3.4. Finite element simulation of the mechanical scanner. (a) Out-of-plane bending movement as the fundamental mode at 96 Hz (b) Second mode due to out-of-phase deflection of springs at 672 Hz. . 46

Figure 3.5. Top side picture of a bare LED die used in the fabrication. 49

Figure 3.6. LED IV characteristics. 50

Figure 3.7. (a) Schematic drawing of the optical characterization setup (b) picture of the integrating sphere used in the characterization process. 50

Figure 3.8. (a) Luminance-wavelength relation of a green/yellow LED (b) luminance-current plot of (b) green/yellow and (c) red LEDs, respectively. . . 52

Figure 3.9. Different luminance values acquired using PWM. 53

Figure 3.10. Feedback circuitry used to acquire the position data. 55

Figure 3.11. Waveforms of the position feedback circuit (a) Electro-coil drive signal (b) Output of the transimpedance amplifier (c) Output of the comparator. 56

Figure 3.12. Fabrication of profile of solid-state LED integrated FR4 Scanners. 56

Figure 3.13. Integration steps of LED dies on FR4 actuator. (a) SU8 trenches of 300×300 μm for LED placement. (b) LED placement with 130 μm gap in between them. (c) LEDs wirebonded to Cu pads. 57

Figure 3.14. Profile of the proposed structure after LED die placement. 58

Figure 3.15. (a) Fabricated device, a close-up view. (b) Device picture with dimensions. 58

Figure 3.16. Current-voltage characteristic of a LED device used in the implementation of the display. Inset: ratio of the powers consumed by the light sources of the present display and a dot-matrix LED display for I_1=10 mA and I_S = 10 pA. 60

Figure 3.17. Employed characterization Setup. 61

Figure 3.18. Displacement-frequency plot of the FR4 scanner. Resonance at approximately 99 Hz. 62

Figure 3.19. Reliability test results of the fabricated display. The device is kept at resonance for about 3 million cycles. 63

Figure 3.20. Some modulation examples: (a) With no actuation and modulation. (b) MNL (c) Checker box image. (d) Gray scale image. . . . 64

Figure 3.21. Schematics of the proposed PLED integrated FR4 scanner-based display. 65

Figure 3.22. Finite-element analysis of the MEMS actuator. (a) Slow-scan (refresh rate at 49.8 Hz) movement as the fundamental mode. (b) Unused torsional movement mode at 193.4 Hz (dimensions in meter). 67

Figure 3.23. Process sequence of FR4 actuator fabrication. 69

Figure 3.24. (a) Front-side and (b) backside views of FR4 actuator. 70

Figure 3.25. Process sequence of PLED fabrication. 71

Figure 3.26. Photograph of fabricated dies of 1D array of PLEDs on PET substrate, temporarily attached to a glass wafer. 72

Figure 3.27. (a) Integration of 1D PLED array and MEMS actuator and (b) Zoomed view. 73

Figure 3.28. (a) Front-side and (b) backside views of MEMS display after integration with 1D PLED array. 74

Figure 3.29. Displacement-frequency and power-resonance (inset) plots of MEMS display. 75

Figure 3.30. Luminance−current−voltage (L−I−V)characteristic of the fabricated PLEDs. 77

Figure 3.31. Generated MEMS display image examples. (a) No actuation and no modulation. (b) Actuated but no modulation. (c) PLED array is modulated to give a checkerboard image. (d) Pattern obtained by selectively turning off several PLEDs. 78

Figure 4.1. Schematics and operation of the 2D scanner devices. (a) Gimballed cantilever scanner (Type-A) (b) Gimballed torsional scanner (Type-B) (c) Magnetic actuation scheme used for both types of the devices. 81

Figure 4.2. Automatized design sheet created in Excel. (SI units are used). . . 83

Figure 4.3. FEA results of the scanning mirrors (a) Type-A, movable frame bending mode (slow scan) (b) Type-A, Mirror bending mode (fast scan). (c) Type-B, movable frame torsion mode (slow scan)(d) Type-B, mirror torsion mode (fast scan). 84

Figure 4.4. (a) 100 μm thick SS301, spin coated and patterned with 6 μm PR mould (b) Schematics of the electrochemical cell (c) Standard electrochemical etching mask (d) Electrochemical etching mask maximizing the current density. 86

Figure 4.5. Pictures of the two different designs. Type-A, gimballed cantilever scanner. Type-B, gimballed torsional scanner. 87

Figure 4.6. Vibration displacement of (a) the movable frame and (b) the mirror of the Type-A scanner as a function of frequency. 88

Figure 4.7. (a) Out of plane displacement resonant peak of the movable frame (b) Out of plane displacement resonant peak of the mirror for the Type-A device. 89

Figure 4.8. Scan line characterization results for Type-A device: (a) Horizontal total optical scan line is 11.7° at a drive power of 42 mW (b) Vertical total optical scan angle is 23.2° at a drive power of 30.6 mW(c) Lissajous pattern. 90

Figure 4.9. Drive power versus total optical scan angle (TOSA) relationship for the cantilever type gimballed (Type-A) scanner and the torsional type gimballed (Type-B) scanner (a) Slow scan characteristics (b) Fast scan characteristics. 91

Figure 4.10. Test setup used for modulation of the light source and the drive control of the electro-coil. 92

Figure 4.11. Two examples of the displayed character patterns; the left one is "MNL" text (size: 4 mm×12 mm) and the right one is the "A" character. 94

Figure 4.12. Photo of the experimental control setup. 94

Figure 4.13. Test wafer used in the characterization of the etching process. . . . 97

Figure 4.14. Electrochemical etch setup used in the proposed process. 98

Figure 4.15. Etch depth as a function of square opening widths for different electrode gaps at a current density of 3 A/cm^2 and for an etch time of 5 min. 99

Figure 4.16. (a) Etch depth versus width of square openings for NaCl solution (b) Anisotropy versus width of square openings for NaCl solution for an electrode gap of 6 mm. 101

Figure 4.17. Process Profile, (a) openings in the photoresist (PR) mask are formed both to etch-through the substrate and to thin the mirror mass. (b) Profile of the device after electrochemical etching. . 101

Figure 4.18. Masking schemes: (a) Typical electrochemical etching mask, (b) Proposed masking scheme. 102

Figure 4.19. Schematic diagram of the targeted mirror structure (a) Device-1: a typical torsional micro-mirror with uniform thickness (b) Device-2: the proposed 1D micro-scanner with thinned mirror mass. 103

Figure 4.20. Finite element simulations of the designed micro-scanner showing the mode shape (inset) and the resonance peak of the torsional movement (fundamental mode) that occurs at 4380 Hz. 104

Figure 4.21. Close-up view of the thinned micro-mirror. 105

Figure 4.22. Closer view of the mirror masses of produced scanners (a) thinned device (b) unthinned device. 106

Figure 4.23. Frequency response of fabricated mirrors. 107

LIST OF TABLES

Table 2.1. Mechanical properties of selected materials. 26

Table 2.2. Different Magnetic Actuation Schemes. 29

Table 2.3. Properties of the used magnets. 40

Table 3.1. Dimensions of the LED integrated FR4 Scanner. 45

Table 3.2. Dimensions of the PLED integrated FR4 Scanner. 66

Table 4.1. Dimensions (in mm) of the Type-A and Type-B scanners. 84

Table 4.2. Dimensions and simulated resonance frequencies of the test devices. 103

LIST OF SYMBOLS

B_{r}	Remnant magnetization
E	Young's Modulus
F_{fast}	Fast scan frequency
F_{MM}	Magnetomotive force
F_{slow}	Slow scan frequency
F_r	Refresh rate of the display
G	Shear Modulus
H	Magnetic field intensity
H_{c}	Coercivity field
J	Mass moment of inertia
K_{bit}	Depth of gray scale image
K_{os}	Over-scan constant
K_{ϕ}	Torsional spring constant
K_{sp}	Spot size to pixel size ratio
K_{s}	Linear spring constant
K_{T}	Beam clipping constant
K_{ub}	Directionality factor
M_{s}	Saturation magnetization
N_H	Horizontal resolution
N_H	Vertical resolution
Q	Quality factor
R_{air}	Reluctance of air
R_{mag}	Reluctance of the permanent magnet
v	Poisson's ratio
δ	Vertical displacement
ζ	Damping ratio
θ	Angular displacement
θ_{mech}	Mechanical scan angle

θ_{opt}	Optical scan angle
λ	Wavelength of the light-source
μ	Shape anisotropy factor
μ_0	Permeability of space
μ_r	Relative permeability
ϕ	Magnetic flux
ϕ_T	Angle of twist of the fixed-free flexural beam
χ	Susceptibility

LIST OF ABBREVIATIONS

1D	One Dimensional
2D	Two Dimensional
AC	Alternative Current
ASIC	Aim Specific Integrated Circuit
CRT	Cathode Ray Tube
DC	Direct Current
DLP	Digital Light Processor
DMD	Deformable Mirror Device
FR4	Fire Resistant 4
IC	Integrated Circuit
LCD	Liquid Crystal Display
LED	Light Emitting Diode
MEMS	Microelectromechanical System
VGA	Video Graphics Array
PCB	Printed Circuit Board
PD	Photodiode
PLED	Polymer Light Emitting Diode
PET	Polyethylene terephthalate
PDA	Personal Digital Assistant
PWM	Pulse Width Modulation
QVGA	Quarter Video Graphics Array
TOSA	Total Optical Scan Angle
UV	Ultraviolet

1. INTRODUCTION

The field of optical microelectromechanical systems (MEMS) is one of the earliest and most active research areas of MEMS technology. It merges various scientific disciplines like micro-optics, microelectronics and micromechanics in order to create new, rich enabling technologies [1]. Several different applications inherent to Optical MEMS can be stated as Digital Light Projection [2], digital displays like grating-light valves [3], adaptive optics [4], fiber optic switches [5], spectrometers [6, 7], confocal microscopes [8, 9], barcode readers [10] and retina raster-scanning displays [11, 12] etc.

1.1. History of Projection Displays and Related Work

Despite this broad range of usage, application and implementation of optical MEMS technology to display elements can be considered as a relatively new concept compared to conventional display technologies like the cathode ray tube (CRT), plasma display, liquid crystal display (LCD) and so on. The emergence of projection display technologies dates back to early years of 20th century [13]. The first practical CRT called Kinescope, was developed by V. Zworykin in 1929 [14]. Zworykin's kinescope which is illustrated in Fig. 1.1 [15] can be considered as the first example of a scanning beam display where an electron beam is scanned onto a fluorescent screen.

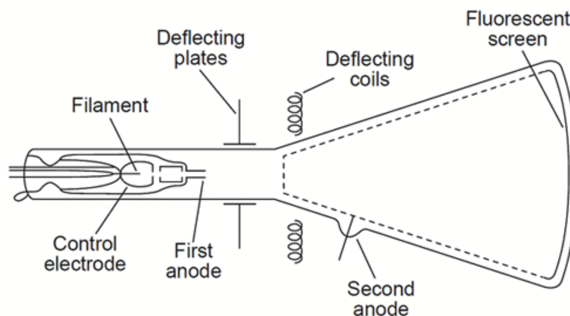

Figure 1.1. Kinescope developed in 1929 by V. Zworykin. After [15].

Later on, in 1939, F. Fischer invented a new projection display system mainly for the large screens found in movie theaters. In order to increase light output and to get

a high-brightness projection display, he proposed the first spatial light modulator or light-valve technology in which the functions of light generation and light control are separated [16, 17]. This device is called *Eidophor* and its system schematics are shown in Fig.1.2 (a).

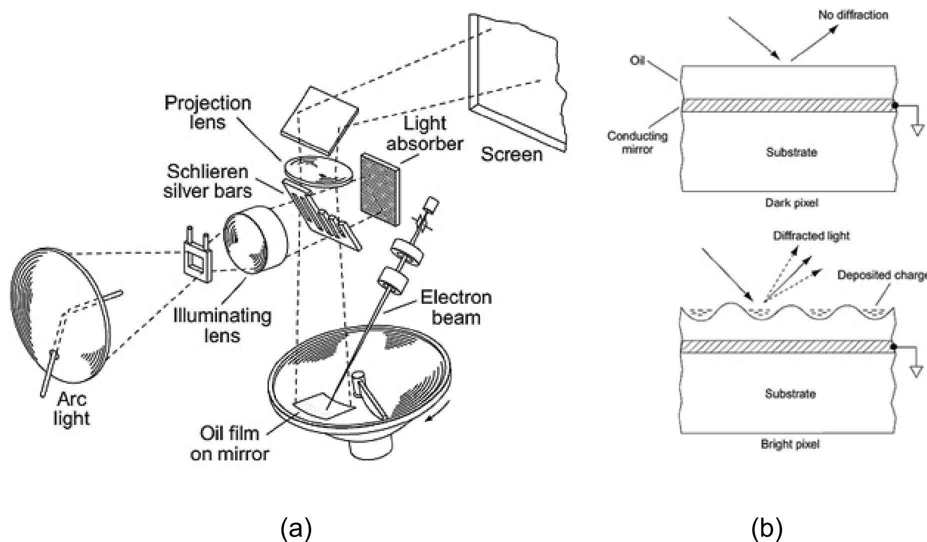

Figure 1.2. (a) Schematic drawing of the Eidophor system. (b) Operation principle of the Eidophor. After [13] and [17].

In this system, the surface of a conducting mirror is covered by a thin layer of oil film. This mirror can be addressed by a rastered electron-beam (e-beam) which scans the oil surface and deposits a charge pattern as illustrated in Fig.1.2 (b). Occuring charge pattern is electrostatically attracted to the conducting substrate and creates a deformation in the oil film, acting as a phase diffraction grating [16, 17].

Subsequently, different kinds of projection display technologies were invented with a gradually increasing pace as in the case of the Scophony projector in which a laser beam whose amplitude is modulated by a video using a acousto-optic modulator [18]. Later on, during 70's, the first micromechanical projection display device known, the mirror matrix tube was developed at Westinghouse Research Labs [19].

One pixel of the mirror matrix tube has four cantilevers as shown in Fig. 1.3 which are electrostatically attracted by the edge forces towards aluminum grid since

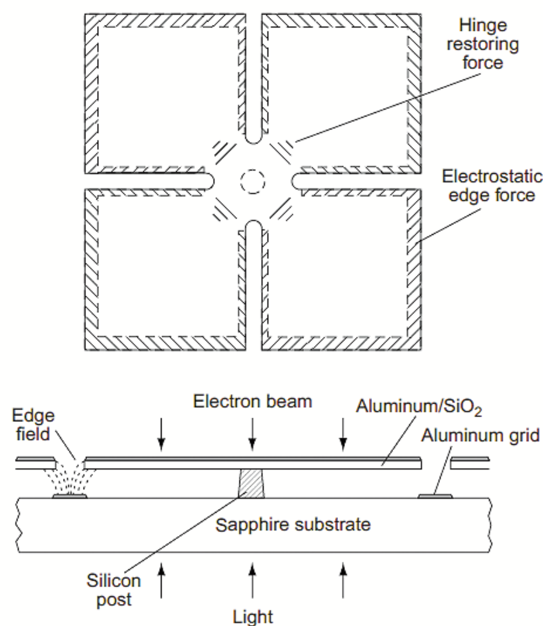

Figure 1.3. Top view and cross-section of mirror matrix tube. After [19].

they are charged with a rastered and modulated e-beam. In this structure, light is beam steered around a cross-shaped Schlieren stop according to the cantilever deflection angle which is a maximum of 4 degrees [13]. Later on, K.E. Petersen at IBM demonstrated a projection display using a 16×1 array of single-crystal cantilever beams that micromechanically modulate the light. In this work, Petersen decribed a micromechanical device which consists of thin metal-coated SiO_2 membrane fabricated on an ordinary silicon wafer using techniques compatible with IC processing [20].

The first commercially available high-volume MEMS based projection display device can be considered as deformable mirror device, DMD, of Texas Instruments. This device was proposed in 1977 and used a membrane-based spatial light modulator which is fabricated on the backside of a thinned CCD address circuit as shown in Fig. 1.4 [13].

In 1996, Texas Instruments launched Digital Micro-mirror Device (DMD) being the first MEMS display device which is monolithically integrated on a digital chip as illustrated in Fig. 1.5. DMD is the first all-digital projection display without any analog links in the electronic chain between the source material and viewer [13].

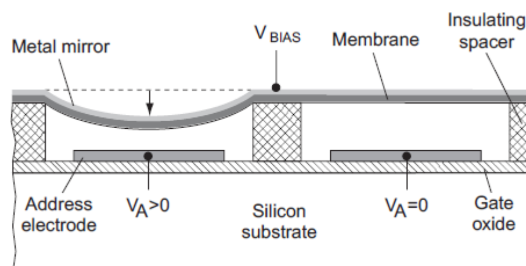

Figure 1.4. Simplified view of the cross-section of DMD. After [13].

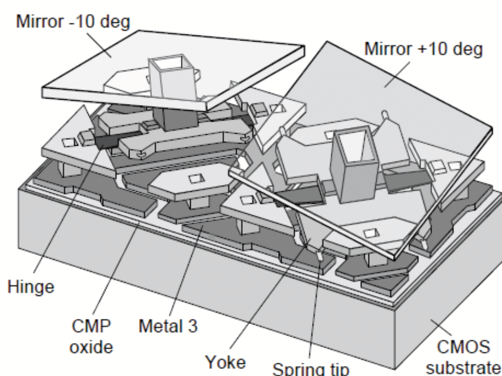

Figure 1.5. Two pixels of digital micromirror device. After [13].

Today, there are various works devoted to projection display technologies and especially on the development of micro-scanner based two-dimensional (2D) displays [21–28] since this new generation of displays have the potential of being smaller, cheaper and more portable than existing displays. For instance, an image can be formed using 2D micro-scanner that raster-scans a properly modulated light. Lately, micromachined scanners that steers the incident light beam in horizontal and vertical directions are used in high resolution display applications as in the case of the picoprojector created by Microvision Inc. In this example, as shown in Fig. 1.6, a gimballed 2D MEMS laser scanner is designed and fabricated to produce a see-through head mounted retinal scanner display device [29]. Device scans a light beam onto the user's retina and successfully display a video content [30].

As it is briefly explained above, there are many possible techniques and technologies to implement two-dimensional micro-scanner based displays. One can utilize (1) a 2D micro-scanner array (one reflective element for each pixel) as in Digital Light Processor [2]. Another technique is to employ (2) one bidirectional or two unidirectional

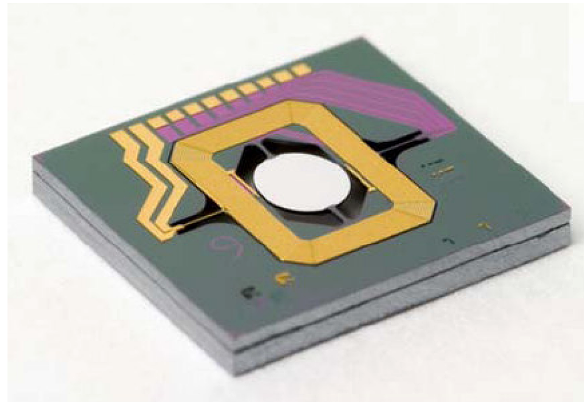

Figure 1.6. 2D MEMS scanner which is used in laser PicoProjector of Microvision Inc. After [29].

raster-scanning mirrors [11, 21] as in high-resolution micromachined silicon based projection displays [22]. It is also possible to use (3) a scanned 1D array as in grating light valve displays [3] to produce a 2D image plane. A similar technique which benefits from a inorganic light emitting diode (LED) array that is put on a torsional scanning platform is also presented in order to realize a three-dimensional (3D) volumetric display [31]. Another work integrating a LED array with double-sided scanning mirrors to produce an auto-stereoscopic display exist in literature [32].

1.2. Summary and Contribution of the Thesis

This thesis work basically explores and employs two different techniques mentioned above to create scanner-based low-resolution display systems. In the first part, a novel all-polymer integrated microsystem, which realizes a 2D display by integrating a 1D array of polymer light-emitting diodes (PLEDs) with a polymer scanner of microelectromechanical system is presented. Electronic modulation of PLEDs forms the first dimension of the display (fast scan), and the scanner actuation orthogonal to the direction of PLED lineup forms the second one (slow scan). Polymer scanner (actuator) is fabricated on a polymer composite (FR4 material) with a double-sided process using lithography to pattern copper lines and laser micromachining to cut the scanner outline. PLEDs are fabricated on polyethylene terephthalate sheets. They have a thin-film structure of indium tin oxide, poly (3,4-ethylenedioxythiophene) poly (styrenesulfonate), poly [2-methoxy-5-(2'-ethyl-hexyloxy)-1,4-phenylene vinylene], and

aluminum.

Subsequently, a gimballed mirror based system is fabricated out of the stainless steel to create a raster-scanned 2D display together with a a novel, self-terminating electrochemical etch process is proposed for the fabrication of scanning steel micro-mirrors. The process uses single mask photolithography, and the etching step is terminated automatically, which at the same time enables the depth profile shaping of the fabricated structure. The proposed process is characterized and then used to fabricate two versions of 1D steel micro-scanners: one with selective thinning of the predefined parts and one without thinning. The fabricated devices are characterized and compared with respect to their resonance frequencies and mechanical quality factors. The thickness of the starting substrate is selectively thinned down in order to decrease the mass of the mirror and eventually to increase the resonance frequency of the fundamental mode.

Major contributions of the work presented in this thesis are summarized below.

- *Realization of an all-polymer, scanner-based low-resolution low-cost optoelectronic display*: A novel type of display which is realized for the first time by hybrid and monolithic integration of polymer optoelectronic devices with MEMS is presented. Polymer LEDs which are employed as the light-sources in this type of display were fabricated under standard room conditions without using any glove boxes. A post-fabrication treatment consisting of thermal and electric field treatments, was used to revive them. After the packaging process, fabricated one dimensional PLED array were integrated on a polymer scanner that is magnetically actuated into its out-of-plane bending mode to create a 9 mm $\times$ 3.4 mm display with a resolution of 20 $\times$ 7. Using an FPGA development board, both the actuation in slow-scan axis and the electronic modulation in fast-scan axis are simultaneously controlled in order to provide a 2D image plane. A similar structure was also realized using this time solid-state LEDs as the light sources. The design, fabrication and integration of the proposed displays are discussed through Chapter 3. An article presenting the all-polymer scanner-based display was published in *IEEE Transaction on Electron Devices* [33]. Another publica-

tion which elaborates solid-state LED integrated polymer scanner based display was made on *Elsevier, Sensors and Actuator A: Physical* [34].

- *A raster-scanning projection display system based on two-dimensional gimballed stainless steel scanners that are fabricated using an electrochemical etching process*: Two-dimensional gimballed scanners were fabricated using a conventional lithography and electrochemical etching process out of stainless steel. Scanners fabricated using this novel cheap and batch compatible fabrication technique were magnetically actuated to create a 2D projection display. An article discussing the novel fabrication method and the proposed display system was published in *IOP, Journal of Micromechanics and Microengineering* [35].

- *Proposing a cheap, self-terminating, batch compatible fabrication process that enables depth profile shaping of steel substrates*: A novel masking scheme which is used in electrochemical etching process was proposed to shape the profile of the structures. One dimensional torsional stainless steel 301 and 420 scanners were thinned down using this novel fabrication method to enhance the performance of the structures. A normalized frequency shift of 15% is calculated out of the experimental data acquired after the thinning process. Proposed method is very cheap and batch process compatible. This fabrication method can be used in high resolution one or two dimensional micro-scanners where a thinned mirror mass and set of thinned slow-scan suspensions result in high fast-scan frequency and a low slow-scan frequency, respectively. A paper elaborating the proposed fabrication method is published in *IOP, Journal of Micromechanics and Microengineering* [36].

1.3. Organization of the Thesis

This thesis is organized in following manner. In the second chapter, theoretical foundations of scanner-based display system are discussed in a detailed way. In this chapter, performance criteria and micromechanics of the scanner-based systems are elaborated. Information about the utilized fabrication materials and magnetic actua-

tion method are also given. In the subsequent chapter, details about the LED/PLED integrated FR4 scanner based display systems are shared. Then, in Chapter 3, stainless steel scanners and the proposed fabrication method are elaborated. Finally, conclusions and outlook for the future works are supplied in the last chapter.

2. THEORETICAL FOUNDATIONS

In this chapter, theoretical foundations which are required to understand MEMS scanner based display structures are presented. Theoretical concepts, definitions and results given in this chapter will make the design and realization of micro-scanner based low-resolution displays possible. First, a brief summary of performance and design criteria of MEMS scanner based display structures will be given in order to get an overall picture on the subject. Then, mechanics of proposed structures will be reported. Afterwards, information about the structural materials preferred in the realization of the display systems will be given. Finally, the chapter will conclude with an elaboration of magnetic actuation method and especially with preferred magnetic actuation schemes.

2.1. Performance Criteria of Scanner Based Display Systems and Design Considerations

The performance of MEMS scanner based display systems and the quality of the images formed by these displays are determined by various parameters. Some of these parameters are the design of mechanical scanner, employed light sources, operation of electronic modulation circuitry, optical system design, etc. There is a vast literature describing the performance issues of MEMS scanner based display systems [30, 37–43]. In this section, these performance and design criteria of such displays will be briefly explained.

The most important performance metrics which help to evaluate and differentiate micro-scanners among many others can be stated as (1) scan angle-scan mirror size product, (2) operation frequency of the scanner, (3) the dynamic surface flatness, (4) scan repeatability (robustness) and (5) scanner position sensor accuracy [30]. In the course of this thesis, proposed structures are designed and realized considering these metrics.

Resolution can be regarded as one of the most crucial properties of a display. It can be defined as the number of pixels, or number of resolvable spots, that the scanner can support [39]. Assuming that the aberrations of the optical system is controlled, the resolution of scanning display systems is mainly determined by the mechanical scanner or more precisely by the product of scan-angle and scan mirror-size which we can shortly signify as θD-product. Once the required number of resolvable spots is determined depending on the targeted application, the scanner and the optical systems can be specified/designed accordingly. In-depth discussion and details on optical design of scanner based systems can be found in [39] and in [40].

The basic formulation which gives the scan resolution N along a specific axis in terms of scanners' physical parameters, can be given as [41]

$$N = \frac{\theta_{\text{opt}} D}{a\lambda} = \frac{4\theta_{\text{mech}} D}{a\lambda} \tag{2.1}$$

where λ is the wavelength of the employed light source, a is the shape factor of the mirror which equals to 1 for square/rectangular mirrors, D is size of the scan mirror along the preferred axis, θ_{opt} is the optical scan angle of the mirror and θ_{mech} is the maximum mechanical scan angle amplitude as depicted in Fig. 2.1. Given the wavelength of the laser source, using this simple equation, one can start to design and to define scanners' parameters by computing the required $\theta_{\text{opt}} D$ values or relatedly the displacement and total optical scan angle (TOSA) of the targeted display format.

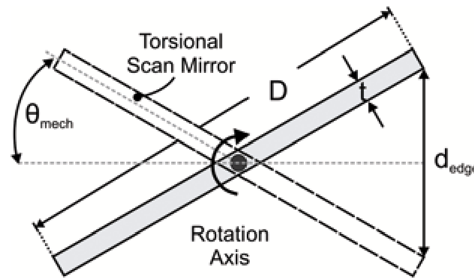

Figure 2.1. Torsional scanner of diameter of D with a mechanical scan angle of θ_{mech}.

Moreover, for a biaxial scanner, Eq. 2.1 can be computed independently for each horizontal and vertical axis. For instance, the governing equation which relates the

parameters of mechanical scanner to the horizontal resolution N_H of the scanner-based display can be given in a more explicit way as [30, 43]

$$N_H = \frac{4\theta_{\text{mech}} D K_{\text{sp}} K_{\text{osh}} \cos\alpha}{K_T a \lambda} \tag{2.2}$$

where K_{sp} and K_{osh} symbolize the spot size to pixel size ratio and the over-scan constant for horizontal axis, respectively. K_T defines the beam clipping constant and α is the angle of incoming laser beam onto the scanner surface.

For instance, in our proposed steel scanners (2D), the typical value of K_{sp} changes between 0.5 and 2. Moreover, in a generic raster-scanning display, scan process comes to a stop at the extremities of the scan line since there is a speed variation at the edges compared to the mid-regions. This value of over-scan factor is taken as 0.8 in the designs in order to cope with the pixel size and brightness variations. The beam clipping factor K_T is presumed to be 1.5 assuming a full gaussian scanned beam shape and the laser wavelength λ is approximately 650 nm since a red laser is utilized for instance in the steel scanner projection display systems.

On the other hand, the vertical resolution N_V can be expanded as [30, 43]

$$N_V = \frac{4\theta_{\text{mech}} D' K_{\text{sp}} K_{\text{osv}} K_{\text{ub}} \cos\alpha}{K_T a \lambda} \tag{2.3}$$

where D' is size of the scan mirror along vertical axis and K_{ub} is directionality factor which equals to two since bidirectional scanning is employed. It is possible to scan two lines onto the screen during one cycle as opposed to unidirectional scanning if bidirectional one is preferred. This mode of scanning doubles the display line rate of the system [40]. However, one should note that in bidirectional scanning, it is required to buffer one line of data and display it in reverse order while sweeping backwards. Bidirectional scanning has also some constraints on phase control between forward and backward scan lines and can produce non-uniform line-to-line spacing across the scan line [30].

Another important issue regarding the performance of mechanical scanners is defining fast scan frequency, f_{fast}, of the system. Fast scan frequency can be computed as [40]

$$f_{\text{fast}} = \frac{F_r N_V}{K_{\text{ub}} K_{\text{osv}}} \tag{2.4}$$

where K_{osv} is the over-scan constant for vertical axis which is usually changes between 0.9 and 0.95. In Eq. 2.4, F_r (or f_{slow}) is the refresh rate of the system. Bidirectional scanners are generally actuated in off-resonance for slow-scan movement, making F_r conventionally equal to 50 to or 60 Hz. Here it is important to note that it is extremely difficult to synchronize two resonant modes of one 2D scanner for display applications. That is why, a master-slave configuration is preferred for fast and slow axis.

Once these basic parameters of the targeted display like N_V, N_H, F_r and f_{fast} are set, the value of θD-product of the display can be computed. The choice of θD-product can be based on performance criteria like dynamic mirror flatness, mechanical stress limitations, requirements of driving circuitry and cost [37]. For instance using a large value of D and therefore having a large scan mirror facilitates the alignment of the laser beam and optical interface. It also increases the acquired displacement assuming the dimensions of flexural beam constant.

On the other hand, larger values of D augment the moment of inertia value depending on Eq. 2.32 which can be found below and deteriorate the dynamic mirror flatness which, in total, affects the optical quality of the display system. Conversely, even though smaller diameters give the designer opportunity to increase the scan frequency, it is very difficult to obtain larger values of scan angle or displacement by using small mirrors in the system if one considers the maximum allowable flexure stress together with the yield stress of the fabrication material. These tradeoffs are explained in an explicit, well-elaborated fashion in the literature and can be referred further in [37] and in [38].

For instance, using above reasoning, θD-product required for a QVGA (320×240)

display is 3.75 deg · mm. Moreover, one should attain a θD-product of 7.5 deg · mm for a VGA (640 × 480) display. Using Eq. 2.4, designer can calculate that the needed fast-scan frequency is approximately 15.7 KHz for a refresh rate (slow-scan frequency) of 60 Hz.

Another crucial factor that a designer should definitely consider while designing a scanner based display systems is the dynamic mirror flatness. High acceleration forces occurring while actuating the mechanical scanner result in bending of the scan mirror. At the edges of the actuation cycle, the profile of the scan mirror becomes deformed. This deviation eventually creates an optical distortion on the image created by the scanner. The maximum mirror deformation for 1D rectangular block mirror can be approximated as [42, 44].

$$\delta_{\text{max}} = 0.217 \frac{\rho f_{\text{scan}}^2 D^5 \theta_{\text{mech}}}{E t^2} \tag{2.5}$$

where ρ is the density of the material used, E is the Young's modulus, t is the thickness of the scan mirror and f_{scan} is the scanning frequency.

Finally, designer should definitely consider the robustness of the system. Adjustment enhancing the scan repeatability must be completed while designing prior to fabrication. Tapering and rounding the regions that are exposed to an overloading stress during actuation or increasing the stiffness of the moving parts that can create metal fatigue problems [33] can be listed as some precautions taken to increase the robustness of the proposed structures. Additionally, fabricated devices should be exposed to cyclic aging during characterization for at least 2×10^6 cycles in order to test their robustness [45].

2.2. Micromechanics of Mechanical Scanners

In proposed micro-scanner based display systems, the most basic mechanical structures that are employed are flexural beams with shuttle mass. These beams are commonly encountered in MEMS as spring elements. Calculating their bending under

simple loading conditions and determining their associated resonant frequency along with their quality factor are essential skills in a design perspective. Flexural beams are usually classified according to their support type. The combination of the two mechanical boundary conditions associated with them help us to name the structures. In this thesis work, for the proposed display systems, two types of flexural beams are commonly used. These are the fixed-free beams (or cantilever beams) connected in parallel with a concentrated end-loading and the double-clamped beam with a central mass as illustrated in Fig. 2.2 (a) and (b), respectively.

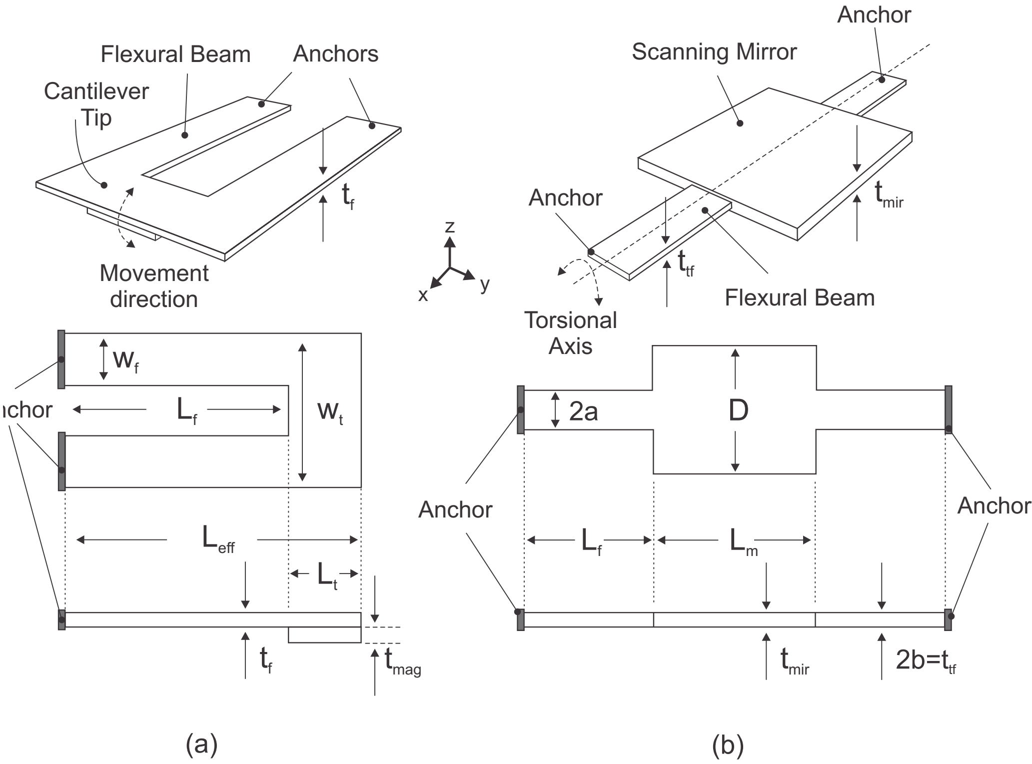

Figure 2.2. Types of flexural beams used. (a) fixed-free beams connected in parallel with a concentrated end-loading. (b) the double-clamped beam with a central mass.

2.2.1. Cantilever Beams

In order to understand 1D scanners given in Fig. 2.2, one must first be able to analyze the fixed-free flexural beam with a rectangular cross-section in other words the cantilever beam which is the most basic mechanical unit in proposed MEMS designs throughout the thesis. Very detailed mathematical relationships and governing expressions predicting the behavior of cantilever beams have been well established in

the literature [44, 46–49] therefore they will be briefly explained in this report. In the subsequent part of this section, the most crucial parameters of the cantilever beams will be defined.

The linear and torsional spring constants k_s and k_ϕ are the most basic parameters of a cantilever beam. They are defined by Hooke's law which states that there is a linear dependence between the applied force/torque and the extension of the spring as long as large displacements are not experienced. The linear and angular form of Hooke's law are given in Eq. 2.6 and Eq. 2.7.

$$F = -k_s y \tag{2.6}$$

$$T = -k_\phi \phi_T \tag{2.7}$$

where F and T are applied force and torque, y is the displacement and ϕ_T is the angle of twist of the fixed-free flexural beam from its equilibrium position.

Initially, translational motion of the cantilever beams is investigated. Translational displacement of a cantilever beam experiencing a point force or torque is depicted in Fig. 2.3. As can be understood from the illustration, vertical displacement or simply bending can stem from the force or torque applied to the cantilever beam.

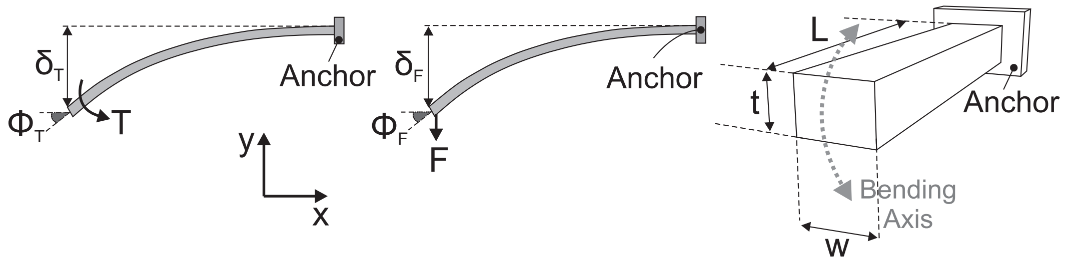

Figure 2.3. Displacement of a cantilever beam experiencing a point force or torque.

Assuming that the external force/torque is applied right to the tip of the cantilever

beam, the linear and torsional spring constants of the beam become equal to [44],

$$k_s = \frac{3EI}{L^3} \tag{2.8}$$

$$k_\phi = \frac{EI}{L} \tag{2.9}$$

where I is the moment of inertia, L is the length of the cantilever beam and E is the Modulus of Elasticity (Young's Modulus). Young's Modulus is an intrinsic property of a material and is constant irrespective of the shape and dimensions of the mechanical structure assuming the material is an isotropic one. Provided that the cantilever beam bends in the direction of the thickness and that it has a rectangular cross section as illustrated in Fig. 2.3 which is usually the case, the moment of inertia I can be computed as

$$I = \frac{wt^3}{12} \tag{2.10}$$

where w and t are the width and thickness of the cantilever, respectively. Combining these equations, the linear and torsional spring constants of a cantilever beam become

$$k_s = \frac{Ewt^3}{4L^3} \tag{2.11}$$

$$k_\phi = \frac{Ewt^3}{12L} \tag{2.12}$$

As can be noticed from Eq. 2.11 and Eq. 2.12, the stiffness of the beam depends on the direction of bending and it provides a compliance to movement in one direction and resistance in another depending on the geometry of the cantilever beam. Moreover, maximum vertical displacements of a cantilever beam's tip, δ_F and δ_T stemming from

the applied force and torque are given in Eq. 2.13 and Eq. 2.14, respectively [44, 46].

$$\delta_F = \frac{4F_{\mathrm{NET}}L^3}{Ewt^3} \tag{2.13}$$

$$\delta_T = \frac{6TL^2}{Ewt^3} \tag{2.14}$$

In addition to the vertical displacements defined in Fig. 2.3, a maximum angular displacement, ϕ_T originating from the applied torque can be stated as in Eq. 2.15.

$$\phi_T = \frac{12TL}{Ewt^3} \tag{2.15}$$

Besides the translational motion explained above, cantilever beams can also exhibit rotational motion and correspondingly an angular displacement. The rotation θ created by the torque applied right to the end of the cantilever can be approximated as [50]

$$\theta = \frac{TL}{Gcwt^3} \tag{2.16}$$

where G is the Shear Modulus and c is a constant whose value depends on the cross-section of the cantilever beam. Shear Modulus G can be expanded as $G = \frac{E}{2(1+\nu)}$ where ν is the Poisson's ratio of the preferred bulk fabrication material. In Eq. 2.16, the value of c depends on the ratio of t/w and equals to 0.14068 for a cantilever beam with a square cross-section.

By using the angular form of Hooke's law given in Eq. 2.7, the torsional stiffness of the cantilever can be computed as

$$k_\theta = \frac{T}{\theta} = \frac{Gcwt^3}{L} \tag{2.17}$$

Hence, the ratio of bending stiffness to torsional stiffness of a generic cantilever beam having a rectangular cross-section is [38]

$$\frac{k_S}{k_\theta} = \frac{1+\nu}{2cL^2} \tag{2.18}$$

Eq. 2.18 means that by just shortening the length L of a cantilever beam, one can increase the translational spring constant over the torsional stiffness or vice versa. This fact is extensively used as a practical method in the design process throughout the thesis in order to provide a safe mode separation for the proposed structures.

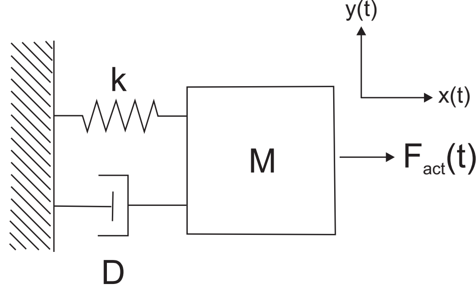

Figure 2.4. Simple harmonic oscillator model of 1D MEMS actuator.

The mechanical structure of a cantilever beam can be simplified to a mass-spring model as shown in Fig. 2.4. The resonance frequency of a cantilever beam can be calculated by solving the characteristic equation of this system. The equation of motion of this system is

$$M\frac{d^2x(t)}{dt^2} + D\frac{dx(t)}{dt} + kx(t) = 0 \tag{2.19}$$

where M is the effective mass, D is the damping coefficient and k is the spring constant of the system. The general solution to Eq. 2.19 is a sinusoidal of the form

$$x(t) = A\sin(\omega t + \alpha) \tag{2.20}$$

where ω is the radial frequency of the vibration, A is the vibration amplitude and α is the phase angle lag. Radial frequency ω can be found by inserting Eq. 2.20 into

Eq. 2.19. Hence, the resonant frequency of a cantilever beam becomes

$$f_0 = \frac{1}{2\pi}\sqrt{\frac{k}{M}} \tag{2.21}$$

For rotational movements of cantilever beams, a similar model and analysis can be used. However, this time, instead of effective mass M, effective polar moment of inertia of mass J_f is used along with actuation torque T_{act} in lieu of F_{act}. The moment of inertia plays much the same role in rotational dynamics as mass does in linear dynamics and for a cantilever beam with a rectangular cross-section, it is equal to

$$J_f = \frac{1}{12}M_f(w^2 + t^2) \tag{2.22}$$

where M_f is the mass of the fixed-free flexural beam depicted in Fig. 2.3. By following similar computation steps, the resonance frequency of a torsion beam can be obtained as

$$f_T = \frac{1}{2\pi}\sqrt{\frac{k_\theta}{J_f}} \tag{2.23}$$

where k_θ was given explicitly in Eq. 2.17.

Damping process which is inevitable in any system, takes energy from the vibration system. In our case, dissipation is mainly dominated by air flow around the moving structures and even though this can be classified as a much weaker damping effect, it will make the system an under-damped one. A damped vibration system is modeled in Fig. 2.4. In frequency domain, the equation of motion becomes:

$$F_{\text{act}}(s) = X(s)(Ms^2 + Ds + k) \tag{2.24}$$

where $F_{act}(s)$ is the actuation force (in our case magnetic actuation force) applied to the cantilever beam and D is the damping coefficient. Applied actuation force and

the displacement created by it are related to each other with the mechanical transfer function $H_m(s)$.

$$H_m(s) = \frac{X(s)}{F_{\text{act}}(s)} = \frac{\frac{1}{M}}{s^2 + \frac{D}{M}s + \frac{k}{M}} \equiv \frac{A\omega_0^2}{s^2 + 2\zeta\omega_0 s + \omega_0^2} \tag{2.25}$$

This transfer function corresponds to a second-order low-pass filter (LPF) characteristics where ω_0 is the undamped natural frequency and ζ is the damping ratio. It is a well-known fact that systems requiring large displacement and that operate at resonance as in the case of micro-scanner based display systems doing a fast-scan movement, are designed as under-damped systems since in these type of systems the response is drastically enhanced around the resonance frequency unlike over-damped and critically damped systems.

Fig. 2.5 shows the pole plot of an under-damped second-order system on a complex-plane together with its time domain response. As it can be noted, there are two complex poles at $-\zeta\omega_0 \pm j\omega_0\sqrt{1-\zeta^2}$. The natural response of a cantilever beam is basically a damped sinusoid with an exponential envelope whose time constant is equal to the pole's real part. The time domain response of this system can be given as $y(t) = Ae^{-\zeta\omega_0 t}cos(\omega_0\sqrt{1-\zeta^2}t - \phi)$ where $\phi = tan^{-1}(\zeta/\sqrt{1-\zeta^2})$. As illustrated in Fig. 2.5(b), the ideal case for a resonant-mode microelectromechanical system is when $\zeta = 0$. It means that the poles of the system do not have any real part and lie on the imaginary axis. More importantly, the structure doesn't dissipate any energy at all and continues to oscillate indefinitely with an initial infinitesimal actuation force.

Fig. 2.6 depicts the frequency response of a second-order under-damped system. At low frequencies, due to the steady-state loading, displacement remains constant. Near the resonance frequency, f_0, the mechanical vibration amplitude increases drastically. The sharpness of the resonant peak is characterized by the quality factor (Q). Quality factor is a dimensionless parameter to model the loss in a specific system and

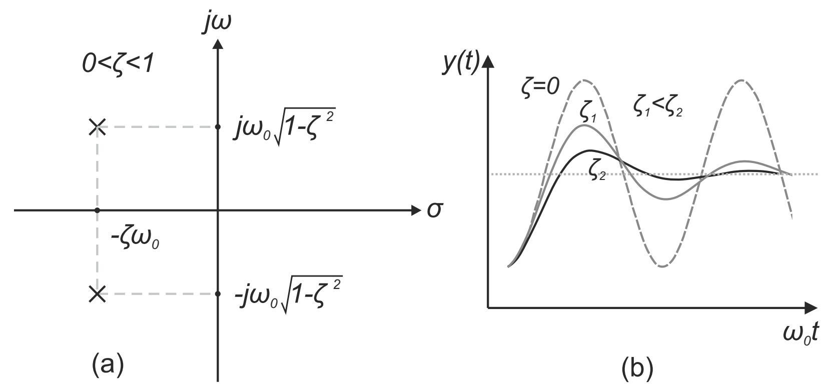

Figure 2.5. (a) Pole plot for an under-damped second-order system. (b) Second-order under-damped time domain responses for different damping ratio values.

it is governed with the following equations.

$$Q = 2\pi \frac{\text{Energy stored per cycle}}{\text{Energy dissipated per cycle}} = \frac{f_0}{\Delta f} = \frac{1}{2\zeta} \cong \frac{\sqrt{kM}}{D} \tag{2.26}$$

The quality factor is proportional to the reciprocal of aforementioned damping coefficient ζ and has a profound effect on the mechanical response of the spring-mass system. This second order system response becomes under-damped for $Q > 0.5$. Even though the system shows a second-order LPF characteristics, for higher values of quality factor ($Q > 10$), the poles of the system goes towards the imaginary axis on the complex-plane and the system starts to act like a band-pass filter as shown in Fig. 2.6 after [47].

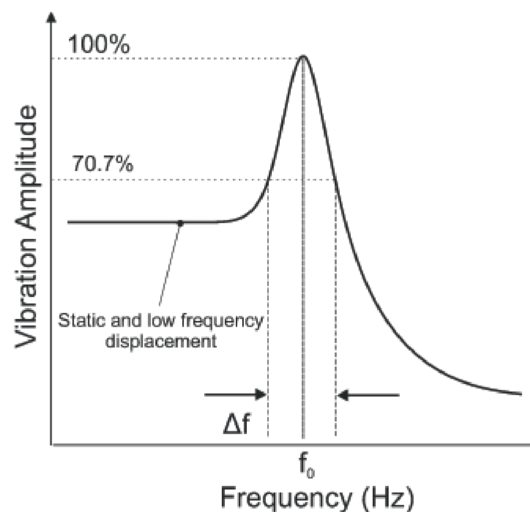

Figure 2.6. Frequency response of a generic fixed-free beam.

Accordingly, the value of the displacement will increase drastically depending on the value of the quality factor once the frequency of the actuation force enters into the pass-band of the cantilever beam if the Q-factor is enough. This situation is formulized in Eq. 2.27 where Z_{res} is the displacement in resonance and Z_{DC} is the static displacement.

$$Z_{\mathrm{res}} \cong Q \cdot Z_{\mathrm{DC}} \tag{2.27}$$

In other words, depending on Eq. 2.27, one can get the targeted displacement out of the actuator by spending Q times less power if the resonant movement is preferred. Therefore, resonant-mode microelectromechanical systems dissipate small amounts of power and enable the design of low-power systems.

2.2.2. Fixed-Free Beams Connected in Parallel With a Concentrated End-Loading

Preferred fixed-free beam geometry is previously depicted in Fig. 2.2 (a) together with the width, length and thickness of the flexure beam as W_f, L_f and t_f, respectively. This system consists of a U-shaped composite polymer actuator that is suspended with two flexures beams to the anchor. The most crucial parameters that define the resonance frequency of the proposed structure can be listed as the geometry and the effective mass of the structure. By combining Eq. 2.11 and Eq. 2.21, the resonance frequency of the proposed structure for the targeted out-of-plane linear displacement mode can be approximated as

$$f_0 \cong 0.16\sqrt{\frac{nE_{\mathrm{eff}}w_f t_f^3}{4L_f^3(m_{\mathrm{L}} + m_{\mathrm{eff}} + m_{\mathrm{M}})}} \tag{2.28}$$

In this relation, n is the number of cantilever beams used in the proposed design which is equal to two in our case as can be seen from Fig. 2.2 (a). The effective total

mass of the cantilever tip in the proposed design has three different components. The first component m_{L} is the total mass of the LEDs (solid-state or polymer) integrated on the actuator. The second one, m_{eff}, is the effective mass of the moving composite (FR4 and Cu) structure (the mass of SU8 layer is also included for the solid-state LED case). The third and the final one, m_{M}, is the mass of the permanent magnet and is the dominant mass among these three terms. E_{eff} is the Young's modulus of the composite material and it can be expanded as:

$$E_{\mathrm{eff}} \cong 0.1304 E_{\mathrm{CU}} + 0.8695 E_{\mathrm{FR4}} \tag{2.29}$$

since the bulk fabrication material is composed of 200 μm thick FR4 substrate which is covered with 30 μm thick copper film on the back side. The resonance frequency of the FR4 scanner is designed according to the equation 2.28 by proper sizing of the structure.

The design with two suspended flexures facilitates placing other mechanical vibration modes of the devices to a frequency sufficiently far away on the spectrum and increases the resonance frequency which had dropped to a lower value due to the relatively heavy permanent magnet that dominates the denominator of the fraction in Equation 2.28. The total vertical displacement formula for this type of actuators can be given as

$$\delta_{\mathrm{TOTAL}} = \frac{2L^2(2F_{\mathrm{NET}}L + 3T)}{Ewt^3} \tag{2.30}$$

The total amount of displacements for the proposed structures can be computed using above equations once the magnetic actuation force and torque are known.

2.2.3. Double-Clamped Beam With a Central Mass

This subsection briefly summarizes the mechanical working principles of double-clamped beam with a central mass which is the key element of the stainless steel

gimballed micro-scanner based projection display. Fig. 2.2 (b) illustrates a scanning mirror which is suspended by torsion beams. These beams are designed such that they are compliant to twisting but resistive to bending. Similar to aforementioned cantilever beams, both a linear translational force and torque are exerted on the scanning mirror during the actuation process. However this time, applied force has a negligible effect and creates a very small amount of out-of-plane bending because of the geometry of the proposed scanning mirror assuming a large enough thickness. The dominant movement of the micro-scanner is rotation due to the applied torque.

Targeted micro-scanner has multiple resonant modes and the first five of them are depicted in Fig. 2.7 after [51]. In this figure, the lowest order fundamental resonant mode (1) is the rotation around the torsion beams. The other mode can be listed as (2) out-of-plane linear translation in z-axis (3) in-plane linear translation in y-axis (4) out-of-plane rotation around y-axis and (5) in-plane rotation around z-axis.

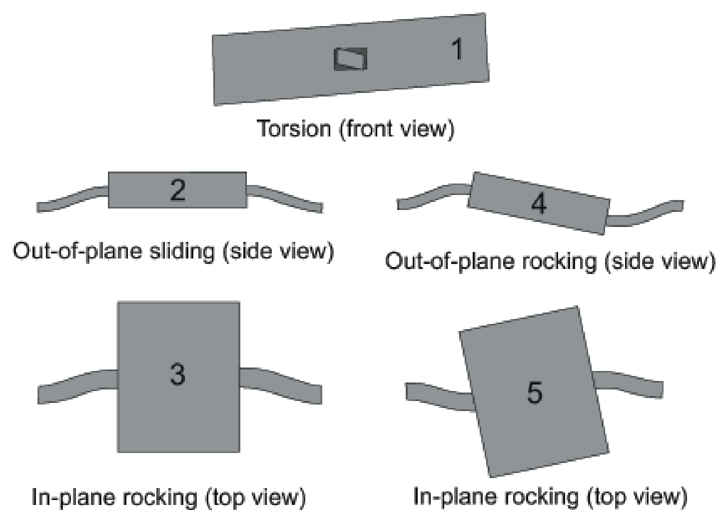

Figure 2.7. Five fundamental vibration modes for the torsional scanner [51].

Design process should be completed such that targeted torsional mode illustrated in Fig. 2.7 (1) appears as the lowest fundamental resonant mode of the scanner. The adjacent mode should be placed to frequencies sufficiently far away from each other in order to provide a safe mode separation and avoid strong coupling between modes. Here, it is crucial to note that microelectromechanical systems have various complicated movement modes at different resonance frequencies. Especially, in under-damped

microsystems, it is almost impossible to attenuate undesired resonant modes of motion by inserting damping structures into the system. What we do basically is to prefer relatively simple micro-structures in the design process so that preventing energy coupling to undesired modes becomes an easier task.

Common form of resonant frequency for torsional micro-system is previously given in Eq. 2.23. The structure illustrated in Fig. 2.2 (b), has a torsional resonance frequency k_θ of [44]

$$k_\theta = \frac{2}{L_f} G a b^3 \left(5.33 - 3.36 \frac{b}{a\mu} (1 - \frac{b^4}{12 a^4 \mu}) \right) \tag{2.31}$$

and an effective mass moment of inertia J_{eff} of [51]

$$J_{eff} = \frac{\rho L_m D t_{mir}}{12} (D^2 + t_{mir}^2) + 0.88 \rho a b L_f (a^2 + b^2) \tag{2.32}$$

where μ is the shape anisotropy constant which is equal to unity for isotropic materials and ρ is the density of the used bulk fabrication material. Further computations of the resonance frequencies of other fundamental oscillation modes for torsional scanner are given in detail in [51].

2.3. Structural Materials Used in Thesis Work

Choosing a suitable fabrication material for a specific MEMS application is one of the most crucial phase of the design process. A diverse range of structural material is so far used in the fabrication of optical MEMS and micro-scanners such as silicon [11, 21–23, 28, 52], stainless steel [35, 36] and polymer materials [53] like Polyimide [54], Epocore [55] and Fire-Resistant 4 (FR4) [33, 34, 56], to name just a few.

Fabrication materials are selected mainly based on their stiffness, strength, suitability for fabrication and cost. Unlike macro-scale structures which are fabricated out of abundant and inexpensive substances, micro-scale structures are constructed of materials such as single crystal Si, SiO_2, diamond and polymers. Table 2.1 lists the

properties of some selected materials [48, 57–60] .

Table 2.1. Mechanical properties of selected materials.

Material	Young's Modulus	Shear Modulus	Density
	E[GPa]	G[GPa]	ρ[kg/m^3]
Al	69	26	2.7
Au	80	30	19.32
Cu	115	44	8.96
Diamond	1035	398	3.5
Epoxy	3	1.2	1.15
FR4	15	6.5	1900
Polystrene	2.8 - 4.1	1.1 - 1.6	1.1
PVC	2.8	1.1	1.4
Si	190	73	2.33
Stainless Steel	210	80	7.9

Today, silicon is the predominant material choice in MEMS. However, in recent years, polymers have started to be used more frequently as a fabrication material. The mechanical properties of polymer materials and epoxy-fiber composites like FR4 are quite different from those of metals and semiconductors. Firstly, the modulus of elasticity of a polymer and FR4 may be as low as several GPa as shown in Table 2.1. This allows scanners made out of these materials a larger value of displacement over scanners fabricated out of materials like Si, stainless steel, Cu and so on, considering Eq. 2.13 and Eq. 2.14. Secondly, polymers provide low-cost, batch compatible fabrication and packaging techniques. Another important property of polymers is that they offer electrical, physical and chemical properties which are not available in other materials like mechanical shock tolerance [54]. Finally, the cost of material is much lower than other fabrication materials. Further information can be found in [60], where an in-depth review of the mechanical properties of polymers are presented.

Among various polymers, FR4 which is the most commonly used material in today's printed circuit board (PCB) technology, is preferred as the structural material of the proposed structures throughout the first part of this thesis work. The power and

the suitability of FR4 stems basically from their capability to acquire large displacement/deflections at low-frequencies. Moreover, various actuators having any kind of geometry can be fabricated out from a sheet of FR4 using standard PCB technology. Besides, readily available Cu layer on FR4 sheets facilitates the electrical connection and modulation of electronic devices integrated on the actuator. Additionally, these electrical connection paths for the electronic components that are created using wet etching or physical carving can be also employed as well as for magnetic actuation (external permanent magnet, integrated coil scheme). Having all these unique properties, FR4 becomes a perfect material of choice to realize proposed scanner-based display.

Another material that is used as a bulk fabrication material during the second part of this thesis work is stainless steel. Stainless steel is a extensively used, well-known structural material in macro-world and there is no need to evaluate its properties in a detailed fashion. A comparison of the mechanical properties of a single-crystalline silicon with conventional manufacturing material like stainless steel exists in literature [59].

Steel is an alternative structural material to traditionally used silicon: it offers a higher Young's modulus (E), a higher torsional modulus (G), a comparable flexural mode frequency coefficient (defined as the ratio between Young's modulus and the material density: $\sqrt{E/\rho}$) and a comparable torsion mode frequency coefficient (defined as the ratio between the torsional modulus and the material density: $\sqrt{G/\rho}$) [41]. These properties make steel an important candidate for resonant mode actuator applications. Additionally, since steel is a soft magnetic material (ferromagnet), magnetic actuation can inherently be utilized to generate excitation force/torque. As a result, similar performances in terms of total optical scan angle, mechanical quality factors and mode frequencies can be obtained by using steel as the structural material.

2.4. Magnetic Actuation

Targeted micro-scanners for the proposed 2D display systems can be actuated by various techniques. This section elaborates the principles of magnetic actuation and

provides both insight and formulations required in the design process.

A detailed comparison among the available actuation methods stating the various advantages of magnetic actuation compared to other ones can be found in [47, 61] and [62]. Magnetic actuation is an advantageous method for optical microsystems in various aspects. Firstly, magnetic actuation method can be designed in a manner not needing any electrical wires on the micro-structures which is an unavoidable situation in electrostatic, thermal and piezoelectric actuation methods. This wireless structure makes the fabrication and packaging processes of the targeted system considerably less complex and grants the method a longer operational range. Secondly, this method is very suitable for display applications because it can deliver very large amounts of loading force for medium sized micro-structures which is a must in such MEMS display systems desiring large angular displacements. Moreover, with the magnetic actuation, one can easily create a torque component in addition to force in order to get a large angular displacement which is a crucial performance criteria for micro-scanners. Finally, external magnetic fields that are able to generate the necessary force and torque are provided by passive elements like permanent magnets that do not consume any power at all by definition.

In order to form a magnetic actuation system, two basic components are required at the two sides of the system. These are the magnetic flux generator and the force generating structure. It is possible to categorize magnetic actuators among themselves depending on the types of magnetic sources and the force generating micro-structures integrated on actuators. The source of the magnetic field can be a permanent magnet, an integrated electromagnetic coil or an external solenoid. Additionally, multiple sources can be used in a hybrid fashion. On the other hand, force generating structures located on the actuator side can be (1) a permanent magnet (2) a soft ferromagnet or (3) an integrated electromagnetic coil on the structure. Table 2.2 illustrates and classifies some different magnetic actuation schemes available in the literature.

In this thesis work, for the proposed systems, two different magnetic actuation schemes are used. Both of them employ an off-the-shelf external coil to produce a

Table 2.2. Different Magnetic Actuation Schemes.

		Force Generating Elements on Microstructure		
		Integrated Coil	Soft Magnet	Permanent Magnet
Field Sources	Hard Magnet	[27,63]		
	External Coil		[35,64–66]	[67]
	Integrated Coil		[68]	
	Hybrid Source		[69]	

magnetizing H-field. They also consist of a force generating integrated permanent magnet for FR4 scanners and a soft-ferromagnet for stainless steel scanners. Similar magnetic micro-actuators using soft-ferromagnets [35,65] or using permanent magnets that are integrated [67] or manually attached [70] have been previously reported in the literature. In the following parts of this section, the operation principles and the governing equations of these proposed magnetic actuation schemes are investigated.

2.4.1. Magnetization and Hysteresis Curve

It is a known fact that interaction between an external magnetic field and a ferromagnetic material can produce magnetic actuation. A magnetizing field (H-field) created by the external coil magnetizes the ferromagnetic layer on the actuator (or the ferromagnetic actuator itself in the case of stainless steel scanners). In other words, when a magnetic field H is applied to a ferromagnetic material, a magnetic induction B is formed inside the material. The relationship between B and H is an intrinsic property of the material. The equation relating B to H is [47,71]

$$B = \mu_0 H + M = \mu_0(H + \chi H) = \mu_r \mu_0 H \tag{2.33}$$

where μ_0 is the magnetic permeability of space, μ_r is the relative permeability of the magnetic material, M is the internal magnetization of the ferromagnetic material and χ is the susceptibility. χ is defined as the ratio of M to H and it indicates how responsive a material to a magnetizing H-field [71].

Ferromagnetic materials are composed of ferromagnetic domains which are small regions in the material. Initial magnetization M of a ferromagnet is zero. In other words, ferromagnetic materials do not have a definite average magnetization direction in the absence of an external magnetic field. The process of magnetization causes the domains to orient/align themselves in the same direction with the external magnetizing field as shown in Fig. 2.8 [72].

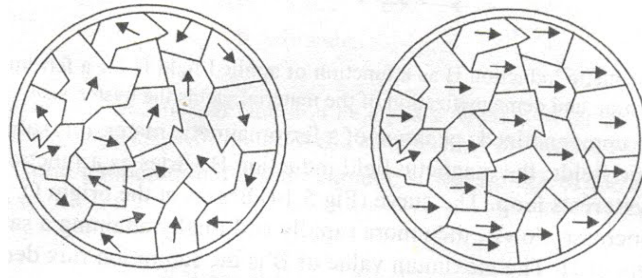

Figure 2.8. Ferromagnetic domains. No magnetic field is applied on the left. External fields orient the domains on the right. After [72].

However, the linear relationship between induced B and magnetizing H is only valid within certain range. The magnetization curve of a ferromagnetic material display a hysteresis behavior as illustrated in Fig. 2.9.

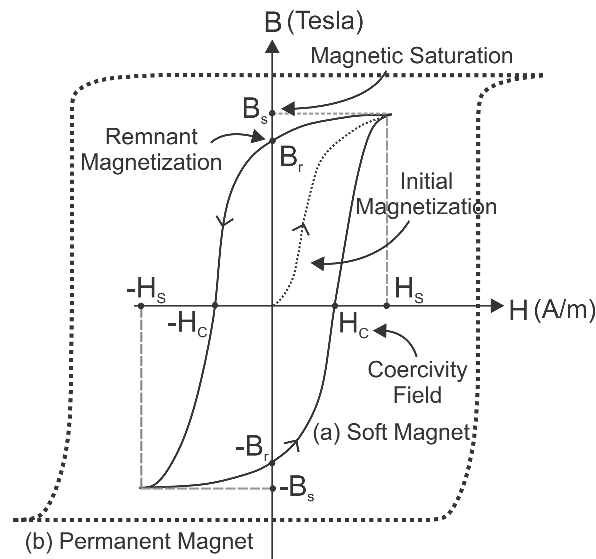

Figure 2.9. Magnetization hysteresis curve of (a) soft magnet and (b) permanent magnet.

As can be seen from Fig. 2.9, the total magnetization of a material cannot increase indefinitely with the applied external field. This phenomenon is called magnetic

saturation. At saturation, all available domains within a piece of magnetic material become aligned to one other. Additionally, ferromagnet loses a portion of its magnetization once we remove the external field. The portion of the saturation magnetization that is kept after this removal is the remnant magnetization. Once the material reached to the saturation, it needs a reverse H-field to make the value of magnetization equal to zero. This negative field is called the coercivity field. Finally, the area enclosed by this curve represents the amount of magnetic energy stored in the material.

Ferromagnets can be classified into two groups depending on their hysteresis curve behavior as hard magnets and soft magnets. Compared to hard magnetic materials, as depicted in Fig. 2.9, soft magnetic material has a very low remnant magnetization level and it exhibits internal magnetization only when an external field is present.

2.5. Lumped-Element Modeling & Equivalent Magnetic Circuit

A schematic view of the magnetic actuation setup is depicted in Fig. 2.10 (a) in which a cantilever beam making an out-of-plane bending movement together with an electro-coil providing NI ampere-turn magnetomotive force (MMF) and a permanent magnet with a magnetic path length of L_{mag} are present.

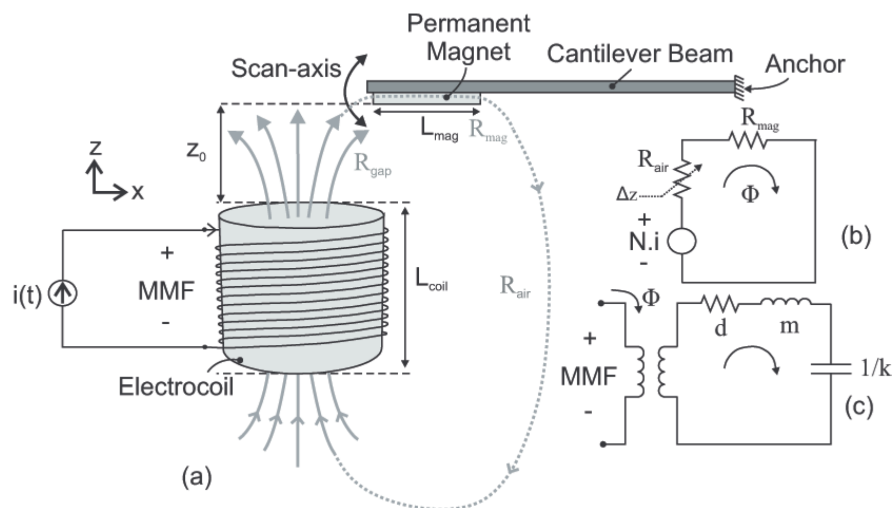

Figure 2.10. (a) Schematic drawing of magnetic actuation setup (b) magnetic circuit equivalent (c) electro-mechanical analogy.

Assuming the fringing fields are negligible in the system, the current applied to the electro-coil creates a magnetic field which is equal to

$$H \cong \frac{NI}{L} \tag{2.34}$$

This magnetic field H, provides a flux ϕ in the magnetic circuit which is illustrated in Fig. 2.10 (a). In lumped element modeling [73], the line integral of H around a suitable closed path is called the magnetomotive force and it is symbolized as F_{MM}. In this magnetic circuit F_{MM} becomes equal to [74].

$$F_{\mathrm{MM}} = NI = H_{\mathrm{mag}} L_{\mathrm{mag}} + H_{\mathrm{gap}} L_{\mathrm{gap}}(\Delta z) + H_{\mathrm{air}} L_{\mathrm{air}} \tag{2.35}$$

where H_{mag} is the H-field in the permanent magnet, H_{gap} is the H-field in the gap between the actuator and the electro-coil and H_{air} is the H-field in between the permanent magnet and the far-side of the electro-coil as illustrated in Fig. 2.10 (a). At this point, it is important to note that L_{gap} is the distance between the permanent magnet and the electro-coil. It is a function that changes with the bending cantilever Δz.

$$L_{\mathrm{gap}} = z_0 - \Delta z \tag{2.36}$$

and L_{air} is the effective distance between the permanent magnet and and the far-side of the electro-coil. To a first order approximation, it is equal to

$$L_{\mathrm{air}} \cong 2z_0 + L_{\mathrm{coil}} \tag{2.37}$$

It is a known fact that the flux in a magnetic circuit is always the same. Thus one can say that in this magnetic circuit, ϕ=ϕ_{mag}=ϕ_{air}=ϕ_{gap}. The flux through any

cross-sectional surface S in the magnetic circuit can be defined as

$$\phi = \int_S B \cdot dA = B_{\text{air}} A \tag{2.38}$$

Therefore, it is possible to write down the magnetic flux densities in term of the flux ϕ as below

$$B_{\text{mag}} = \frac{\phi}{A_{\text{mag}}} \tag{2.39}$$

$$B_{\text{air}} = \frac{\phi}{A_{\text{air}}} \tag{2.40}$$

$$B_{\text{gap}} = \frac{\phi}{A_{\text{gap}}} \tag{2.41}$$

where A_{mag}, A_{air} and A_{gap} are the areas of the related regions as illustrated in Fig. 2.10 (a), respectively. Here, A_{gap} is approximately equal to A_{air}. Having also known that in the permeable material, B_{mag}=$\mu_{mag}H_{mag}$ and in the air B_{air}=$\mu_0 H_{air}$ where μ_0 is the permeability of the free space, one can rewrite Eq. 2.35 as

$$F_{\text{MM}} = NI = \frac{\phi}{\mu_{mag}A_{mag}} L_{\text{mag}} + \frac{\phi}{\mu_0 A_{air}} L_{\text{gap}}(\Delta z) + \frac{\phi}{\mu_0 A_{air}} L_{\text{air}} \tag{2.42}$$

Combining Eq. 2.42 with Eq. 2.36 and Eq. 2.37, the magnetomotive force becomes equal to

$$F_{\text{MM}} = NI = \phi \left[\frac{L_{\text{mag}}}{\mu_{mag}A_{mag}} + \frac{L_{coil} + 3z_0 - \Delta z}{\mu_{mag}A_{air}} \right] \tag{2.43}$$

In this equation, the term in square brackets give the reluctances of the magnet

and the total air gap in series. It can be said that since the leakage flux in neglected, this equation gives the upper limit of ϕ. The above magnetic actuation system can be represented as a magnetic circuit diagram as shown in Fig. 2.10 (b). In this circuit, Ampere's circuital law can be applied as an analog to Kirchoff's voltage law. Therefore, we can rewritten Eq. 2.43 in a more compact form as

$$F_{MM} = NI = \sum_k R_k \phi_k = \phi(R_{mag} + R_{air}) \tag{2.44}$$

where R_{mag} and R_{air} are equal to Eq. 2.45 and Eq. 2.46 below, respectively.

$$R_{mag} = \frac{L_{mag}}{\mu_{mag} A_{mag}} \tag{2.45}$$

and

$$R_{air} = \frac{3z_0 + L_{coil} - \Delta z}{\mu_0 A_{air}} \tag{2.46}$$

where F_{MM}, R_k and ϕ_k are the analog of electromotive force, resistance and current passing through the circuit, respectively. In Fig. 2.10 (c), the mechanical equivalent circuit of the system is illustrated. The governing equations and the response of this circuit was previously investigated in Section 2.2.

In other words, the displacement of the actuator Δz is directly related to the applied current I of the electro-coil with Eq 2.43.

2.5.1. Magnetic Actuation of Stainless Steel Scanners

Briefly, when the external H-field is non-existent, the stainless steel torsional mirror depicted in Fig. 2.11 can be considered non-magnetized because of its low remnant magnetization. Stainless steel structure generates mechanical force and torque when it is placed within a magnetic field gradient.

It is previously mentioned that stainless steel is a soft-ferromagnetic material

and when an external magnetic field is applied to a ferromagnetic material, internal magnetic fields of the domain structures are aligned along a specific axis [47, 71]. More precisely, if the substrate is not spherical (the thickness to length ratio t/D of the proposed ferromagnetic mirror is smaller than 0.02), then there exists a long axis (easy-axis) easy to magnetize along [75]. This phenomenon is known as shape anisotropy. The magnetization vector in the ferromagnetic material remains in-plane due to the shape anisotropy and its out-of-plane component is neglected.

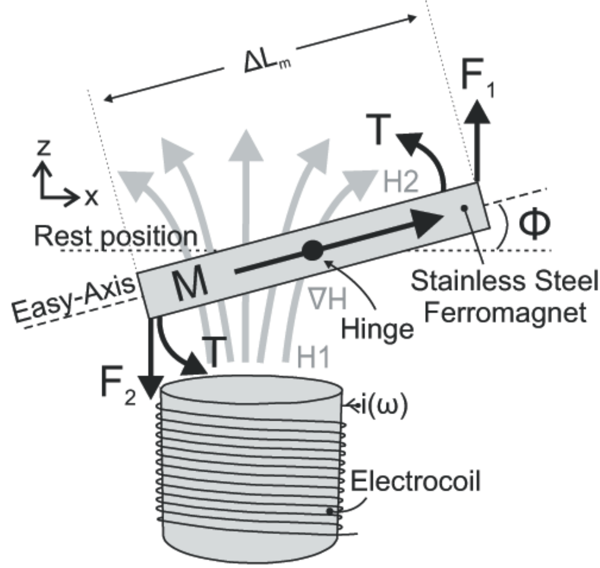

Figure 2.11. Schematic representation of forces and torques under non-uniform H-field in torsional scanners.

A conceptual drawing about the preferred magnetic actuation scheme is shown in Fig. 2.11. The applied H-field magnetizes the ferromagnetic material and creates a magnetization vector M that remains in-plane due to the shape anisotropy and whose magnitude and direction is dependent on the applied external field. North and south poles of the magnetized ferromagnet experience forces F_1 and F_2. The magnitude of these two forces can be computed by

$$F = MDt_m H \cos\phi \tag{2.47}$$

where D and t_m are the width and the thickness of the mirror, respectively. A net force $F_{\mathrm{NET}} = F_2 - F_1$ is exerted on the mirror. This resulting net force stemming from the H-field gradient is pulling the magnet to the coil as a function of the distance between the

centers of the magnet and the coil. This net force triggers the structure to an unwanted out-of-plane pumping mode. However, the structure is specifically designed as a double clamped torsional beam with a central mass as previously illustrated in Fig. 2.2. Thus, thanks to its geometry, structure is inclined to make a torsional movement at its fundamental mode and moreover, at that operation frequency the out-of-plane pumping movement has a quite low displacement which can be easily neglected compared to the torsional movement.

This implication suggests that we can simply ignore the effect of F_{NET} while actuating desired torsional steel scanners. However, there exists also a torque component acting on the structure which tends to minimize the overall energy in an actuator system by aligning the magnetization with the field lines of the external magnetic field. Torque created in counter-clockwise direction can be calculated as [76].

$$T = F_2 \frac{\Delta L_m}{2} \cos\phi + F_1 \frac{\Delta L_m}{2} \cos\phi \tag{2.48}$$

where ϕ is the angle between the easy-axis of the scanner and the upper-surface of the electro-coil and L_m is the length of the magnetic material. If we combine Eq. 2.47 with Eq. 2.48, torque T becomes

$$T = MH[Dt_m \Delta L_m] \cos\theta = MHV \cos\theta \tag{2.49}$$

where V is the volume of the magnetic material.

As we can see from Eq. 2.49, torque T is dependent on both magnetization M and applied external H-field. It is important to note that these two parameters are also functions of the electro-coil driving current $i(t)=I\sin(\omega t)$. If the offset level of the applied electro-coil current is zero and if a magnetic DC field created by a permanent magnet is absent in the system, then the torque T created by a small, non-saturation external H-field ($H \sin\omega t$) can be approximated to

$$T = M\sin(\omega t) H \sin(\omega t) V \cos\theta = \frac{MHV}{2}(1 - \cos(2\omega t))\cos\theta \tag{2.50}$$

This equation tells us that created torque has two components: A DC component of $MHV/2$ and an AC component whose value is changing with $cos(2\omega t)$. It is important to note that the frequency of the AC component is twice the drive current frequency ω. It means that in order to trigger the structure into its designed fundamental resonant mode, a coil driving frequency which is exactly half of the designed value $f = f_0/2$ must be used. Moreover, the resulting torque is a unidirectional one since the sign of the equation is always positive [26].

The displacement created on the scanner is directly dependent on the applied current as in Eq. 2.44 and on torque as shown in Eq. 2.16. In order to increase the torque and eventually the displacement, related M and H values of the system must be increased. A permanent magnet creating a strong DC external field (increase in H-field) can be used to magnetize the ferromagnet into saturation (increase in the magnetization M) in the actuation of the scanners. Another approach is to use a bigger ferromagnet to increase the volume V. Depending on the case and used bulk material, this approach requires to use a thicker magnetic layer on the scanner or to simply use a bigger ferromagnet providing a higher value of V. If a permanent magnet is preferred to magnetize the ferromagnet as we do in our designs, the torque equation becomes

$$T = M_s[H \sin(\omega t)]V \cos\theta \tag{2.51}$$

A direct results of this new torque equation is that the torque and eventually the actuation is now bidirectional since the direction of M_s does not change at all because of the added permanent magnet in the system. Moreover, the frequency of the forcing function becomes equal to the electro-coil driving frequency. Further discussion on this types of magnetic actuation scheme along with its scaling effect can be found in [58] and in [77].

2.5.2. Magnetic Actuation of FR4 Scanners

As the actuation scheme of the FR4 scanner, a moving magnet actuation is preferred. This scheme constitutes an external electro-coil that is used an integrated permanent magnet as the force generating unit. Similar actuation schemes are previously reported in literature [65, 78]. There are several advantages of using a moving magnet actuation over other magnetic actuation schemes. Firstly, permanent magnets can produce large actuation forces and therefore large displacements since the volume of a permanent magnet is greater than the volume of any generic permalloy layer. Proposed displays are millimeter scale devices and creating a ferromagnetic layer with volumes comparable to permanent magnets on these structures is difficult. Moreover, they have a very low-power consumption compared to soft-magnetic actuators. Additionally, neither the magnitude nor the direction of the magnetization vector in an ideal hard magnetic material is changing during the actuation process in contrast to soft-magnetic materials. Finally, permanent magnets possess a bigger value of remnant magnetization and magnetic saturation level as illustrated in Fig. 2.9.

The trade off of using this magnetic actuation scheme is that one should integrate the permanent magnet and the actuator in a hybrid fashion. Adding a manual integration step to the fabrication process complicates the realization of such structures. Moreover, the mass of the magnets is nearly always dominant compared to the mass of the actuator even though they are in millimeter scale. This phenomenon reduces the targeted resonant frequency depending on Eq. 2.21 and can create other movement modes for the structure.

Similar to the case with stainless steel scanners, there exists both a force and a torque component acting on the FR4 scanner in the preferred magnetic actuation scheme as illustrated in Fig. 2.12.

The net force that is created due to the magnetic field gradient of the external

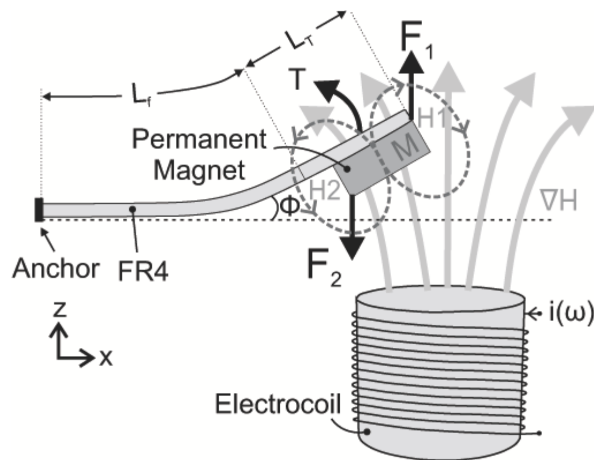

Figure 2.12. Schematic illustration of magnetic actuator mechanism used in FR4 scanners.

electro-coil can be expressed as [58]

$$F_{NET} = M_s(H_2 - H_1)V \tag{2.52}$$

In addition to the net force created thanks to the applied H-field gradient, similar to the actuation of stainless steel scanners, there exists also a torque component whose value is equal to Eq. 2.49. Therefore, considering Eq. 2.52, Eq. 2.49 together with Eq. 2.30, one can compute the related displacement value.

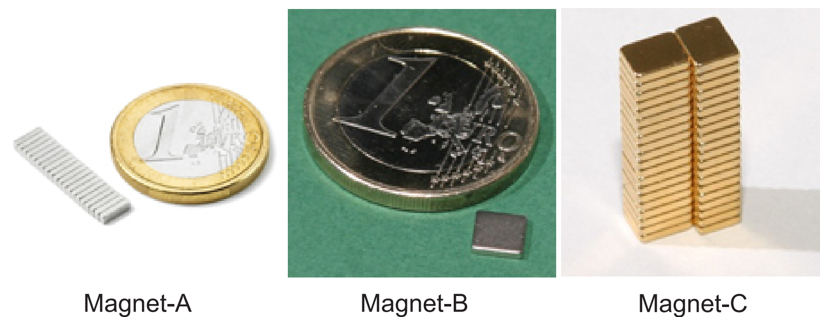

Figure 2.13. Different types of magnets used in the design process. After [79].

Finally, mini permanent magnets that are used in the actuation of FR4 scanners are shown in Fig. 2.13 [79]. These magnets are purchased from Supermagnet.de. The most crucial properties of these magnets are listed in Table 2.3. Once again it is

important to note that the weight of the magnets are larger compared to the weight of scanner itself and therefore, dominate the resonance frequency equation of FR4 scanners given in Section 2.28.

Table 2.3. Properties of the used magnets.

Magnets	Coating	Weight	Length	Width	Thickness	Strength	Flux
		[gr]	[mm]	[mm]	[mm]	[gr]	[Tesla]
Type A	Nickel	0.0514	5	1.5	1	140	1.32-1.37
Type B	Nickel	0.2202	5	5	1	350	1.32-1.36
Type C	Gold	0.1793	5	5	1	350	1.37-1.42

3. LED INTEGRATED MEMS DISPLAYS

In this part of thesis work, light-source integrated FR4 scanners are thoroughly investigated. Proposed integration of microelectromechanical systems with LEDs in order to produce 2D displays is a promising alternative to aforementioned conventional display technologies in Chapter 1. Today, there are various studies on semiconductor (solid-state or organic) LED-based dot matrix displays, which can be considered as a mature technology [80–83]. These conventional solutions incorporate modulation of 2D LED matrix with a driver electronic circuitry [84, 85].

Resolution of such displays depend on the number of LEDs used in the 2D matrix, which becomes excessively large in terms of device count and expensive for high-resolution systems. Such a conventional realization technique for 2D matrix displays has some major disadvantages. It does not only suffer from the large number of LEDs used in the system but also from the following conditions: 1) low yield due to difficulties in high-density semiconductor optoelectronic device fabrication, 2) reliability problems like dead pixels and 3) high fabrication and material cost.

Proposed system offers a novel method for realization of 2D displays by integrating the light sources with the polymer actuators. The basic idea is to employ a scanned 1D array as in grating light valve displays [3, 86] to produce a 2D image plane. The operation of the system relies on the modulation of the light sources in one axis (called fast-scan axis) and the resonant movement of the LED-integrated MEMS platform in the axis perpendicular to the fast-scan axis (called slow-scan axis) as depicted in Fig. 3.1.

This method has a number of advantages over the conventional techniques. These can be listed as follows: 1) usage of just one row of LED array leads to severe reduction in the cost of light sources; 2) due to reduced number of light sources, reliability is expected to increase significantly, having much smaller number of dead pixels and lower amount of LED-to-LED variation. Depending on the resolution, this enhancement is

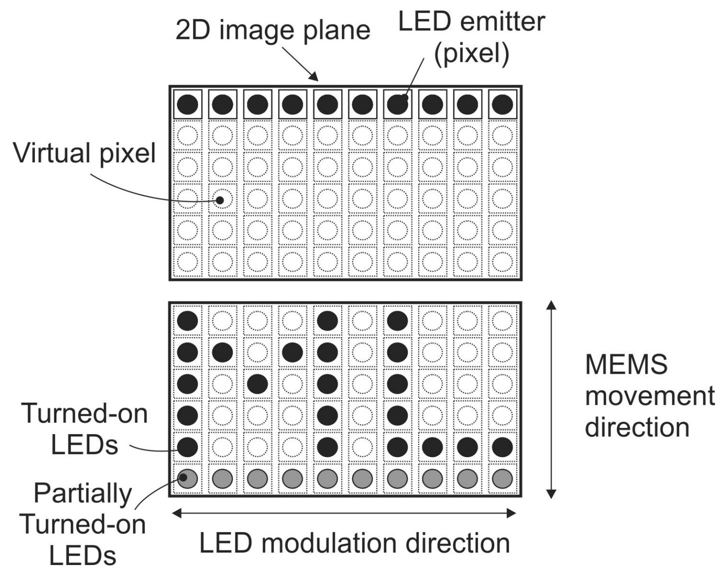

Figure 3.1. 1D array of LEDs creating virtual pixels due to MEMS-actuation in a direction perpendicular to electronic modulation axis.

expected to be around the number of rows; 3) Reduction in number of light-sources and the choice of polymer as the structural layer of MEMS actuator solve the difficulties in fabrication process which are present in conventional displays; 4) the present display represents a technologically new class, and it is, in principal, possible to perform full monolithic integration with polymer LEDs (PLEDs); 5) traditional LED-based 2D displays, excluding organic and/or polymer LEDs and electronics, cannot use active matrix addressing and are limited to passive matrix addressing [80], which in turn puts limitations on the resolution and size of the displays. Present method, however, alleviates this problem significantly, due to 1D array addressing simplicity, even if the passive array addressing is used. This interdisciplinary study claims to yield a highly original 2D display, merging two fields, namely, MEMS and electro-optics.

Moreover, there is no similar system previously reported in the literature that enables the integration of polymer MEMS actuators with especially PLEDs to implement medium-resolution, e.g., QVGA (320×256), VGA (640×512) miniaturized 2D displays. Representative numbers for a potential VGA realization are as follows: a LED emitter size of 50 μm$\times$50 μm, a LED pitch of 100 μm, and an actuator width of 65 mm. These numbers show that it is realistic to have a display in a common video format. Such a display component can be used in low-resolution consumer electronics

products like mobile phones, MP3 players, digital cameras and hand-held PDAs, etc., representing an alternative class of display as a reliable, robust and low-cost system.

In this chapter, operation principles, design processes, fabrication methods, experimental works and measurements of the proposed scanner-based displays are presented. At first, the displays are realized by integrating solid-state LEDs on the FR4 actuator. Subsequently, similar techniques and principles are used to fabricate this time a fully polymer scanner-based display using polymer LEDs.

3.1. Operation Principles of FR4 Scanner-Based Displays

The operation principles of the proposed structure including the material selection for fabrication and the preferred actuation method are very briefly summarized in this section. Schematic of the proposed system is illustrated in Fig. 3.2, where an actuator suspended with two springs at the anchoring regions and a 1D array of LEDs (PLED or solid-state) placed on the actuator surface can be identified.

Basic operation of the device relies on the electronic modulation of the light sources in the fast-scan axis and the mechanical resonance vibration of the actuator at a designed frequency (refresh rate of the display) in the slow-scan axis which is perpendicular to fast-scan axis, as depicted in Fig. 3.2. Simultaneous and precise control of the slow-scan movement of the FR4 actuator and the electronic modulation of the LEDs in the fast-scan axis form virtual pixels and thus generate a 2D image, as enclosed by the 2D image plane illustrated in Fig. 3.1. The height and the width, in other words the resolution of the proposed 2D display consisting of virtual pixels, depend directly on the number of utilized LEDs and on the displacement of the mechanical actuator.

The choice of the structural layer for the mechanical actuator is crucial since the preferred material should provide a high mechanical displacement for low-resonance frequencies. For this reason, as explained in Section 2.3, polymer composite materials are chosen as the structural layer of this scanning display since their spring constants

are one orders of magnitude smaller than the ones of inorganic materials. Additionally, the slow-scan motion of this scanning display is realized by magnetically actuating the FR4 structure at its fundamental resonant mode. Resonant movement is preferred in these structures since their displacements are drastically increased depending on their Q-factors as demonstrated in Eq. 2.27.

It is previously declared that magnetic actuation (a field generating external electro-coil and a force generating integrated permanent magnet) is preferred in the proposed display system. As elaborated in Section 2.4, magnetic actuation method needs no electrical connection to the mechanical structure and produces large actuation forces and large displacement. Other actuation methods like electrostatic and piezoelectric actuation are not preferred since the former requires very small capacitive air gaps and very low atmospheric pressure whereas the latter one is a method which requires a large area coverage.

3.2. Solid State LED Integrated FR4 Scanners

Targeted display is first realized by integrating solid-state LEDs onto the designed polymer actuator illustrated in Fig. 2.2 (a). Proposed display structure is depicted in Fig. 3.2. This system consists of a U-shaped composite polymer (FR4) actuator that is suspended with two flexures to the anchor. The underlying operation principles of this structure are previously summarized in Section 3.1. In the following subsections, design, fabrication and experimental measurements of the targeted scanner-based display will be explained. Information on employed LEDs and preferred position sensing circuitry will be also given in the following sections.

3.2.1. Design of the Proposed Structure

Resolution and frequency calculations, mechanical design methodology and the related actuation force computation are explained in a detailed fashion through Chapter 2 of this thesis. We know that the refresh rate and the resolution of the targeted 2D display is defined by the mechanical actuator and the number of LEDs integrated

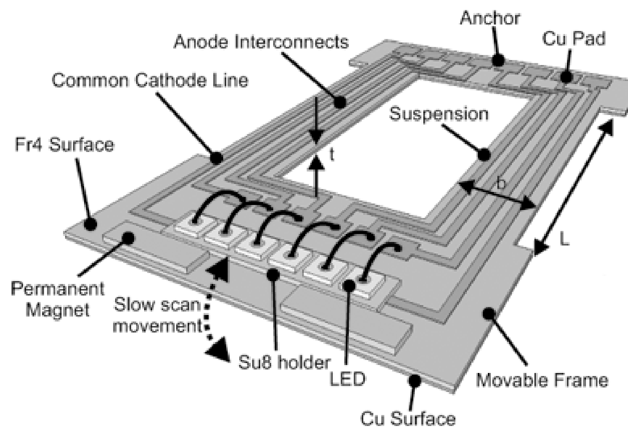

Figure 3.2. Conceptual drawing of the proposed solid-state LED integrated FR4 display.

(20 solid-state LEDs in this case) onto the surface of this actuator. Therefore, it is crucial to design the actuator such that it will have a reasonable refresh rate as well as a large shuttle deflection.

Considering the actuator as a combination a lumped shuttle mass at the tip of two cantilever beams, the resonance frequency (slow-scan mode) related to the out-of-plane movement of the mechanical platform can be approximated as in Eq. 2.28. The resonance frequency given in this equation is designed to be 100 Hz by proper sizing of the springs for the refresh rate (slow scan) of the 2D display. By taking also Eq. 2.5 and Eq. 2.30 into consideration during this design part, required structure dimensions are determined. In order to make the design part easier, automatized excel sheets are prepared containing the derived formulas in previous chapter. A sample of these sheets is given in Fig. 3.3. Tailored dimensions are listed in Table 3.1 using the parameters illustrated in Fig. 2.2 (a).

Table 3.1. Dimensions of the LED integrated FR4 Scanner.

Parameter	t_f	L_f	L_t	L_{eff}	W_f	W_t
Dimension(mm)	0.23	23	6	29	5	12

The design with two suspended flexures facilitates placing other mechanical vibration modes of the devices to a sufficiently far frequency on the spectrum and increases the resonance frequency which drops to a lower value due to the relatively heavy permanent magnet that dominates the denominator of the fraction in equation 2.28. Once

MEMS display design sheet for both S.S. Leds (December 2008)
The material used is 200um FR4 coated with 30um Copper, Maximum 3 flexures are available for design

Parameters	Symbol	Unit	Design 1	Design 2	Design 3	Design 4	Design 5
DESIGN							
Number of Flexures	n_flex		3	2	2	2	2
Number of LEDs	N		241	51	11	11	11
LED Dimension	L_Dim	(um)	260	260	260	300	300
LED Gap	L_Gap	(um)	70	100	100	1000	
Side Gap (Scanner)	S_Gap	(um)	60	50	1500	3000	
Top-Down Gap (Scanner)	T_Gap	(um)	60	900	1500	2000	
Path Width	P_Width	(um)	50	50	100	300	
Path Gap	P_Gap	(um)	70	70	70	1000	
Side Gap (Path)	S_Gap_pth	(um)	40	50	110	300	
Length of Beam	L_Beam	(um)	25000	25000	25000	26000	26000
DIMENSIONS							
Length of Scanner	L_Scanner	(um)	14970	5250	4350	13100	14600
Width of Scanner	W_Scanner	(um)	79580	18360	6860	19300	24200
Width of Beam	W_Beam	(um)	9730	3150	1170	7400	7400
MASS							
Scanner mass	M_Scanner	(gr)	1.10E+00	8.86E-02	2.74E-02	2.33E-01	3.25E-01
Flexure mass	M_Flexure	(gr)	6.71E-01	1.45E-01	5.38E-02	3.54E-01	3.54E-01
Silicon mass	M_Silicon	(gr)					
Magnet mass	M_Magnet	(gr)	gold coated	no magnet	no magnet	nickel coated	nickel coated
Magnet mass coefficient	K_Magnet	(gr)	6	2	2	2	2
Driver mass	D_mass	(gr)					
Total mass	M_Total	(kg)	2.17E-03	8.86E-05	2.74E-05	6.73E-04	7.65E-04
Inertia (out of plane)	In	m4	1.42E-14	4.61E-15	1.71E-15	1.08E-14	1.08E-14
Inertia (in plane)	In	m4	2.00E-11	6.77E-13	3.47E-14	8.78E-12	8.78E-12
Spring constant (out of plane)	k	(N/m)	332.63	71.79	26.67	149.93	149.93
Spring constant (in plane)	k	(N/m)	465850.55	10537.76	539.98	121454.04	121454.04
Frequency (out of plane)	f	(Hz)	**62.27**	**143.18**	**156.83**	**75.10**	**70.42**
Frequency (in plane)	f	(Hz)	**2330.40**	**1734.72**	**705.75**	**2137.47**	**2004.27**

Figure 3.3. Automatized excel sheet used for designing the proposed structures.

the structure topology and rough dimensions have been chosen as above, finite element analysis is used for more accurate results. The resonance frequency is in vicinity of 100 Hz and finite element simulations reveal an out-of-plane deflection at f_0=96 Hz, as shown in Fig. 3.4 (a). Adjacent mode in the frequency spectrum occurs at f_1=672 Hz, as given in Fig. 3.4 (b), where the actuator shuttle is deformed because of the out-of-phase movements of each suspension.

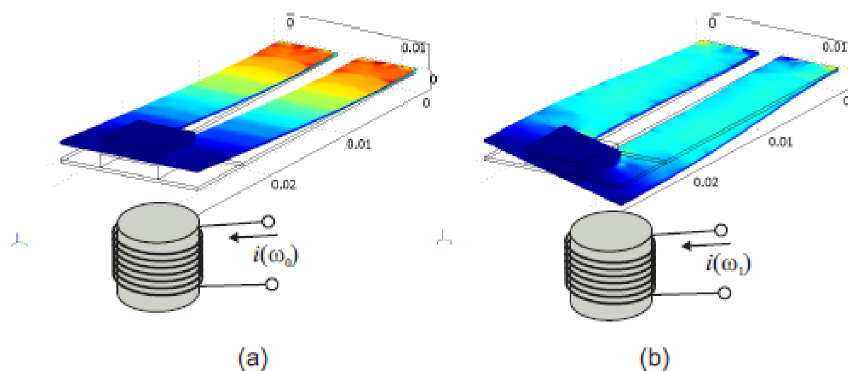

Figure 3.4. Finite element simulation of the mechanical scanner. (a) Out-of-plane bending movement as the fundamental mode at 96 Hz (b) Second mode due to out-of-phase deflection of springs at 672 Hz.

FR4 scanner is set in scanning motion at its fundamental resonant mode using magnetic actuation principles explained in Section 2.5.2. Mechanical platform is excited in the slow-scan axis by utilizing electromagnetic force induced due to interaction of an off-chip electro-coil and a mini permanent magnet. An alternating current passing through off-chip electro-coil and the DC magnetic field develops a frequency-dependent actuation force. This magnetic force acts against the spring force and bends the flexure resulting in deflection of the fabricated cantilevers. When the frequency of the sinusoidal current passing through the electro-coil enters into the pass band of the FR4 scanner, a drastic increase in displacement is observed due to quality factor of the scanner. This effect helps to decrease the power consumption stemming from the actuation.

The scanner is driven only at the frequency of the out-of-plane bending mode which is sufficiently far away from the adjacent modes in the frequency spectrum. The actuation setup, briefly sketched in Fig. 3.4, does not favor the excitation of in-plane modes, because of the negligible electromagnetic interaction between the permanent magnet and the anchored coil. Therefore parasitic vibrations parallel to the surface of the coil are eliminated both by mechanical spring design through w_f/L_f ratio and by the coil arrangement that induces the electromagnetic force.

For the generation of fast-scan modulation signal, unidirectional writing is preferred over bidirectional writing scheme, because of its immunity to phase variations of the drive signal. A sinusoidal driving signal at 100 Hz is applied to the external electro-coil for resonant operation of the scanner. The device moves faster around the center of the generated scan pattern and slower at the edges of scan pattern. Therefore, the implication of varying actuator velocity must be considered while creating the modulation signal in order to have the same effective dimensions for the virtual pixels.

A simple solution to this problem is to scan a long 1D line using the resonant motion of the scanner and to use only a portion of the scanned line for the display. This over-scan factor concepts is previously explained in Section 2.1. When 100% of the total scan line is used in a display ($K_o = 1$), the speed variation would produces

considerable pixel size and brightness variations as it is explained. In a typical scanning display, writing is stopped at the extremities of the scan to cope with this phenomena. This halting period ranges from 10% to 30% of a total scan in a generic writing process [30]. In this work, a relatively moderate value $K_o = 0.8$ is utilized in unidirectional writing in order to minimize unwanted variations without further decreasing the vertical resolution given as

$$N_V = \frac{f_{\text{fast}} \cdot K_o \cdot K_{ub}}{f_{\text{slow}} \cdot 2^{K_{\text{bit}}}} \tag{3.1}$$

where N_V is the vertical resolution of the display, f_{fast} is the fast scan frequency, K_o is the over scan factor, K_{ub} is the scanning scheme factor which is 1 for unidirectional and 2 for bidirectional scanning, f_{slow} is the slow-scan frequency and K_{bit} is the bit depth of the targeted gray scale image. For the present case, the parameters are chosen as $f_{\text{fast}} = 250$ kHz, $K_o = 0.8$, $K_{ub} = 1$, $K_{\text{bit}} = 5$ and $f_{\text{slow}} = 100$ Hz, resulting in a vertical resolution of approximately 62 whereas the horizontal resolution of the proposed display, N_H is set by the number of LEDs in the array (in our case $N_H = 20$).

3.2.2. Solid-State LEDs and the LED Driving Scheme

One of the most crucial parts of this project is the integration of light sources on the polymer actuator. The main aim of this integration part is to put as many LEDs as possible on a limited surface in the most easiest and cheapest way. Therefore, first, smallest LEDs available in the market are investigated. Surface mounted devices (SMDs) are not utilized since the smallest device dimension available in the market is 0.5 mm $\times$ 1 mm. Thus, bare LED die having much smaller dimensions are preferred and purchased.

A conceptual drawing of the employed solid-state LEDs in this thesis together with their pictures taken under microscope are shown in Fig. 3.5. The width and the length of these LED dies are both 250 μm whereas their thickness is approximately 200 μm. In this LED, the top contact provides a pad for the bonding wire. The pad is

circular with a diameter of 100 μm. This top contact pad also provides a low-resistance ohmic contact to the current-spreading layer [87]. With the help of this Au contact, the anodes of the LEDs are easily wedge-bonded to the related cathode lines using a TPT HB05 wirebonder.

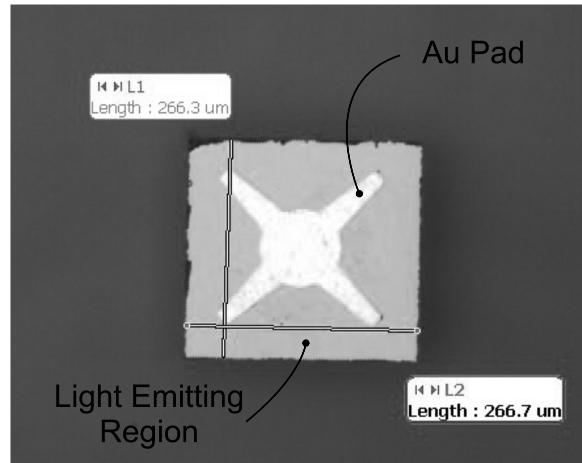

Figure 3.5. Top side picture of a bare LED die used in the fabrication.

A cross-shaped contact as shown in Fig. 3.5 provides a more uniform current distribution over the entire area of the active region. The area of the top contact is deliberately kept small so that the light emanating from the active regions is not hindered by the opaque contact. For LEDs, it is desirable to maximize luminous intensity and luminous flux while keeping the LED chip area minimal.

The DC current-voltage (IV) characteristic of the LEDs used in the system are extracted using a Keithley 4200 SCS semiconductor parameter analyzer as shown in Fig. 3.6. As can be understood from this plot, in order to pass a meaningful amount of current through the LED, approximately 1.5 V is required.

Luminance-current characteristic of the utilized LEDs is acquired by using a characterization setup shown in Fig. 3.7 (a). In this setup, LED die is driven with a power supply by limiting the current that passes through the LED with the help of an external resistor. LED die which is put into the integrating sphere shown in Fig. 3.7 (b) is swept for different current values. The related luminance values at LED's emitting wavelength are monitored and recorded using a spectrometer. At this point, it is

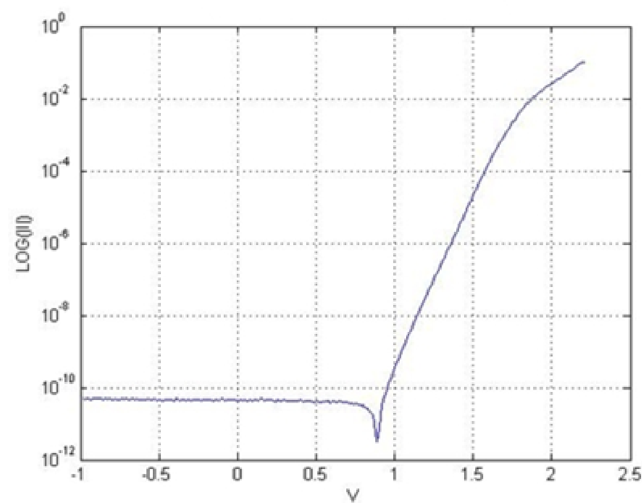

Figure 3.6. LED IV characteristics.

important to note that the amount of luminance changing with the applied current is a crucial information in order to reach to the desired luminance value/contrast ratio and eventually to design the desired electronic driving circuitry.

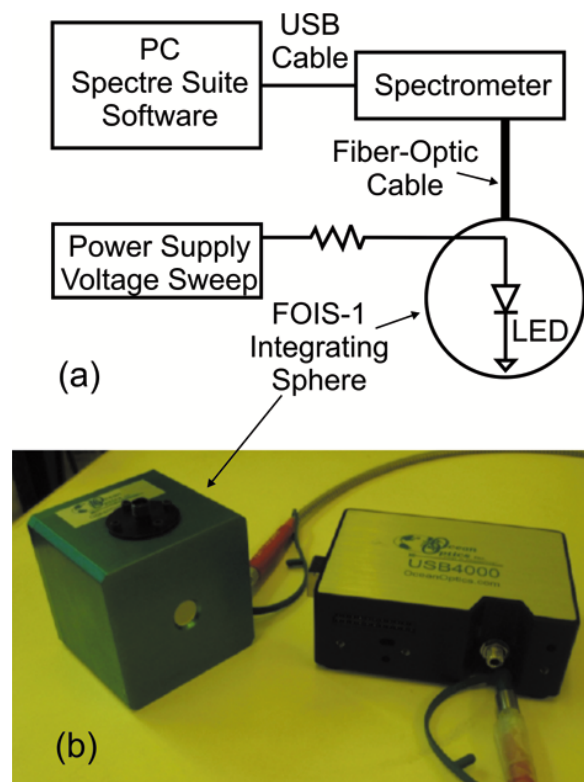

Figure 3.7. (a) Schematic drawing of the optical characterization setup (b) picture of the integrating sphere used in the characterization process.

Fig. 3.8 (a) shows the luminance-wavelength relation of a green/yellow LED for a constant driving-current. The device under test mostly emits light at a wavelength of approximately 560 nm which corresponds to a color of yellowish-green. Moreover, luminance-current (LI) plots of the green/yellow and red LEDs are given in Fig. 3.8 (b) and (c), respectively. These plots show that there is a linear relation between the luminance and the current passing through the devices. However, as the applied driving current gets larger, deviations from the linear behavior are started to be observed, especially after 45 mA for the green/yellow LED and after 32 mA for the red LED due to the existing parasitic resistances in the devices.

As a result, it is possible to get sufficient luminance values out of the LEDs by simply modulating the current passing through them. It should be noted that one of the most important factors defining the contrast ratio of a display is the ratio of the luminance formed with the application of the maximum amount of allowable current, to the parasitic luminance formed while no driving current is exerted at all. These facts are extensively referred while designing the Pulse Width Modulation (PWM) LED driver circuitry and tested on a 1D LED array as shown in Fig 3.9.

Analog luminous intensity control is one of the most basic and simple methods of control. In this method, luminosity is controlled with the current passing through the LEDs. It can be assumed that there is a linear relation between the luminous intensity and the current passing through the light emitting devices as mentioned above. The most important advantage of this type of driving is to create virtually an infinite number of luminance levels. This level of luminance intensity is directly related to the current/voltage control of analog power supply. However, in this type of driving scheme, one should continuously apply the driving signal which at the end, increases the power consumption. Therefore, a digital driving scheme is preferred over the analog one.

Electronic modulation of the LEDs is performed digitally by Spartan 3AN Field Programmable Gate Array (FPGA) development board. LEDs are connected to the output ports of the FPGA development board via resistors. Since the logic high output

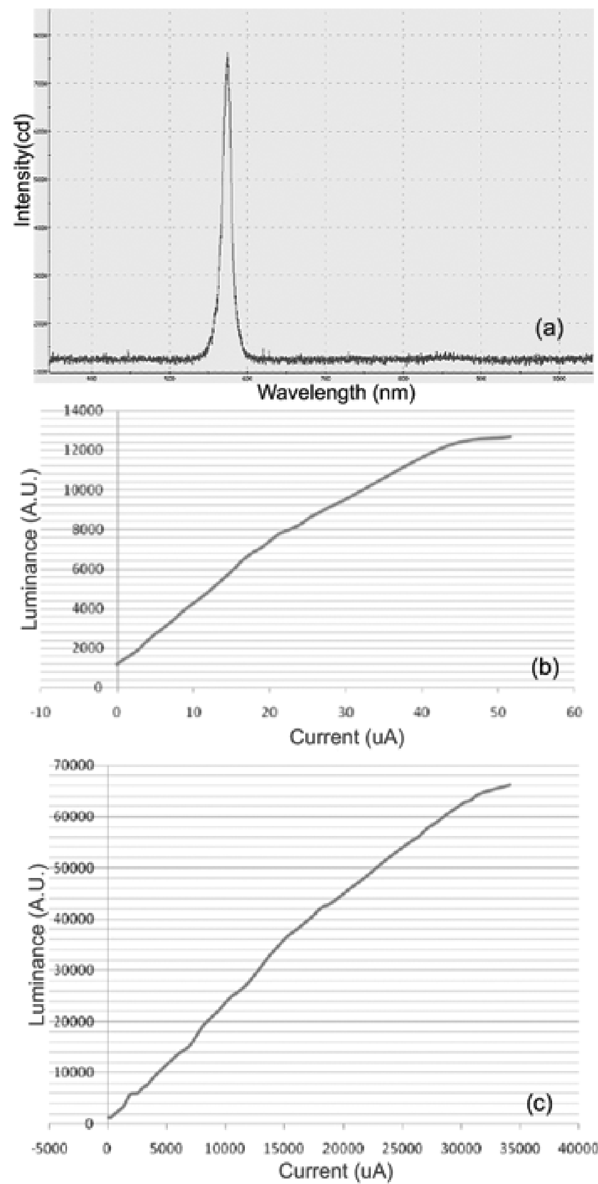

Figure 3.8. (a) Luminance-wavelength relation of a green/yellow LED (b) luminance-current plot of (b) green/yellow and (c) red LEDs, respectively.

value of the FPGA is assigned as 3.3 V and the turn-on voltage of the LED is taken as 2 V, the resistors can be used for limiting the current to 10 mA. A software code digitally driving the LEDs using pulse width modulation (PWM) is written for this FPGA (Appendix A). This specific code creates pulse signals out of the FPGA at the desired frequency and with the intended pulse widths. Therefore, driving the LED array using PWM principle becomes a possibility. PWM is a modulation principle which is frequently used in the control of DC motors and in determining the luminance levels of light sources. The duty cycle of the driving signal determines the luminance

intensity of light source with the following formulation:

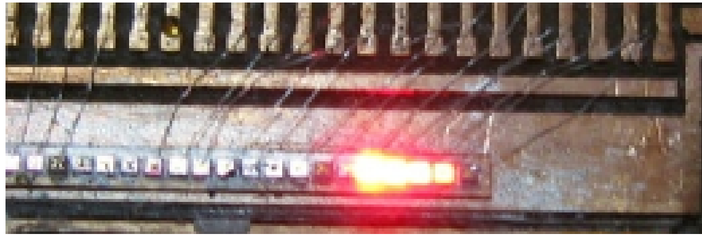

Figure 3.9. Different luminance values acquired using PWM.

$$\eta = \frac{t_{\text{pulse}}}{T} \tag{3.2}$$

where t_{pulse} symbolizes the pulse width and T determine the period of the created signal. The character patterns that are desired to be displayed are stored in the FPGA via a look-up table. The look up table data is sent to LEDs in a row by row fashion, therefore all LEDs are modulated in parallel.

The modulation frequency for fast scan is chosen with respect to the fundamental resonant frequency in order to maximize the number of pixels. The chosen fast scan modulation frequency determines the number of rows obtained on the display. Hence, the fast scan modulation frequency value can be changed to obtain the desired number of rows. The ratio of the fast scan modulation frequency to the fundamental frequency is equal to the number of rows obtained, therefore the fast scan modulation frequency has to be an integer multiple of the resonant frequency in order to maintain a stable image.

On the other hand, even if the ratio is an integer value, the precision of the FPGA clock frequency and the jitter of the FPGA output signal may cause some shifts and distortions on the produced image. FPGA related distortions can either be minimized by synchronization between the electrical and the mechanical parts of the MEMS display or by manually adjusting the FPGA settings. The first technique requires, a feedback signal created by a motion sensor which will be elaborated in Section 3.2.3.

Scanning operation can be done unidirectionally or bidirectionally. In the presented scanner-based display device, bidirectional scanning results in two times more intense pixel level than the level obtained in the unidirectional scanning. On the other hand a synchronization problem in the device results ghosting effect or blurry pixels as previously explained in Section 2.1 and should be treated accordingly. The intensity of the emitted light is set by implementing PWM technique which is based on changing the duty cycle ratio of the modulation signal. The duty cycle ratio changes the total amount of current injected to the LEDs per period changes proportionally. Therefore, smaller duty cycle ratios create darker pixels, while the larger ones create brighter ones. To get minimum and maximum pulse widths, clock frequency is multiplied by the depth of PWM signal. Therefore, the pixel clock frequency, f_{pixel} can be given as

$$f_{\mathrm{pixel}} = f_{\mathrm{slow}} \times n_{\mathrm{row}} \times n_{\mathrm{PWM}} \tag{3.3}$$

where f_{slow} is the slow-scan frequency or the refresh rate of the display, n_{row} is the number of rows and n_{PWM} is the level of the PWM signal. The level of the PWM signal was limited by the FPGA clock and the maximum output signal frequency.

3.2.3. Position Sensor and Modulation

The light sources that are integrated onto the surface of the FR4 scanner are modulated along the fast-scan axis using a modulation circuitry that is composed of a Spartan 3AN FPGA development board together with additional active and passive components. This board is electrically connected to the light sources via Cu interconnects and generates the necessary modulation signal of still images intended for display. However, in order to synchronize this modulation signal with the actuation signal of FR4 scanner, the position data of the scanner in slow-scan movement must be acquired.

Schematics of the circuitry that is used to acquire the position data of the mechanical scanner is depicted in Fig. 3.10. This circuit comprises a 660 nm laser diode which is aligned with a photodiode (PD) having a peak response at about the same wave-

length, a transimpedance amplifier for PD current amplification and an open-circuit collector comparator (LM311) for digitization of the signal for further processing in FPGA board.

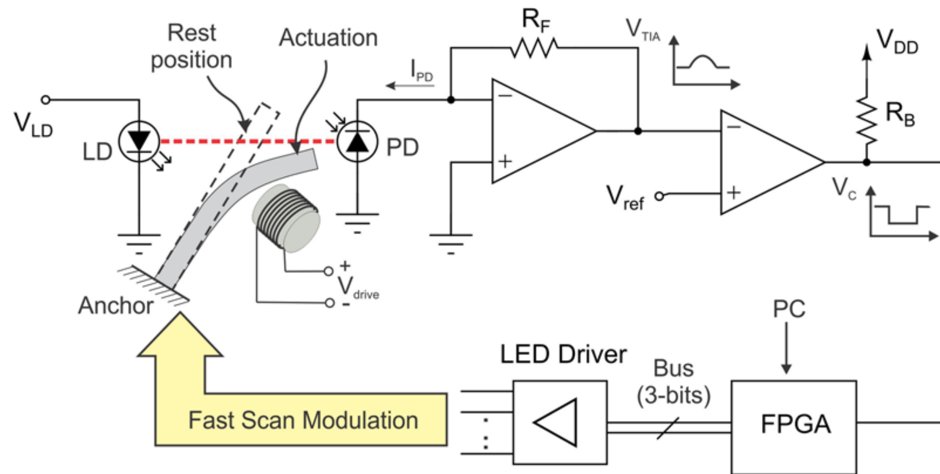

Figure 3.10. Feedback circuitry used to acquire the position data.

Optical components of Fig. 3.10, are aligned altogether in such way that when the scanner is at its rest position no light is received by the PD. PD begins to collect light from the laser source and produce current at its output when the mechanical structure is actuated. Amplitude of the output voltage of the transimpedance amplifier is proportional to the shuttle deflection. Every cycle of the scanner vibration therefore generates a digital signal at the comparator output corresponding to the vertical synchronization pulse. The FPGA collects and uses this sync signal and prompts the simultaneous output, shown as fast scan modulation in Fig. 3.10, for the modulation of display LEDs along the fast-scan axis. Fig. 3.11 shows the waveforms at the particular nodes of the position detection circuit. The optical feedback signal (I_{PD}) carries the position information of the mechanical actuator which is driven by the signal V_{drive} shown in Fig. 3.11 (a). At the output of the transimpedance amplifier, half wave clipped signal is observed due to inclined positioning of the actuator, as shown in Fig. 3.11 (b). This signal is compared with a reference voltage of V_{ref} and an inverted digital version of the sync signal to be fed to the FPGA block is created, as given in Fig. 3.11 (c).

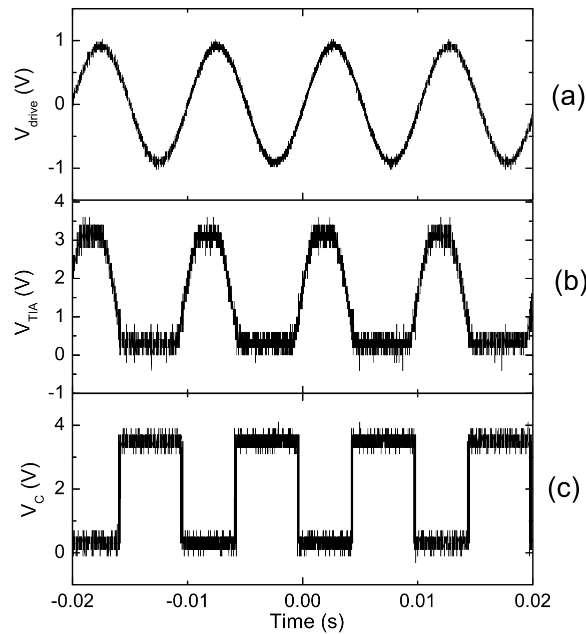

Figure 3.11. Waveforms of the position feedback circuit (a) Electro-coil drive signal (b) Output of the transimpedance amplifier (c) Output of the comparator.

3.2.4. Realization of Solid-State LED Integrated FR4 Scanners

Realization of the display is briefly outlined in Fig. 3.12. A 200 μm thick FR4 substrate which has 30 μm thick copper films on both sides is used as the starting material. Electrical paths and the common cathode line to LEDs are formed on the Cu film using an industrial PCB cutter.

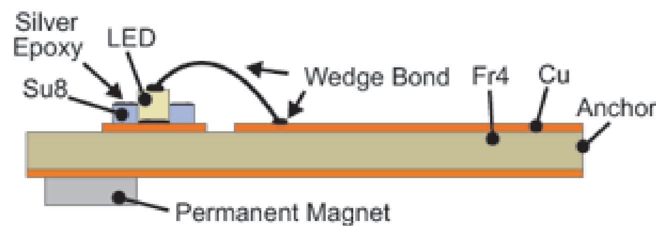

Figure 3.12. Fabrication of profile of solid-state LED integrated FR4 Scanners.

The back side of the platform is completely covered with Cu and is not removed at all to increase the stiffness and the quality factor of the mechanical actuator. It also alleviates the problem of metal fatigue due to large amplitude deflection of the

actuator happening at the Cu electrical paths.

Afterwards, the front side of substrate is coated with 10 μm thick SU8 layer. This layer is patterned lithographically after proper alignment and then developed to form 300 μm $\times$300 μm trenches that are needed for LED placement as shown in Fig. 3.13 (a).

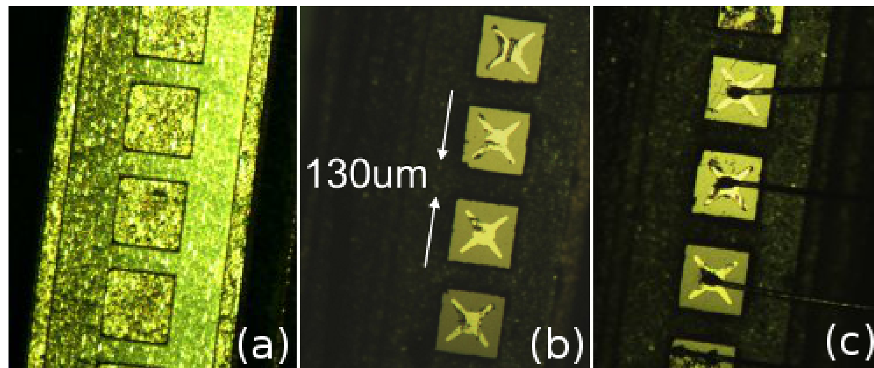

Figure 3.13. Integration steps of LED dies on FR4 actuator. (a) SU8 trenches of 300×300 μm for LED placement. (b) LED placement with 130 μm gap in between them. (c) LEDs wirebonded to Cu pads.

Subsequently, silver epoxy is applied inside the trenches to provide the necessary stickiness and electrical connectivity between LEDs and Cu interconnects. In this process, silver epoxy is preferred to ordinary solder due to its superior wetting and removal properties. Afterwards, LEDs are carefully placed as a one dimensional array into the trenches with a 130 μm gap between each other as shown in Fig. 3.13 (b) and left to dry for approximately 12 hours. Subsequently, placed LEDs are wedge-bonded to anode interconnects to complete the electrical circuitry as can be seen in Fig. 3.13 (c).

A stylus-type surface profiler (Veeco Dektak 8M Stylus Profiler) is used to characterize the topography of the resulting structure. The profile can be seen in Fig. 4.4, where in between 250 μm and 500 μm of the horizontal axis, an SU8 opening in the form of a valley (cathode pad) is visible which will then be used for wire bonding. Fabrication step is concluded by attaching gold-plated permanent magnets which have the

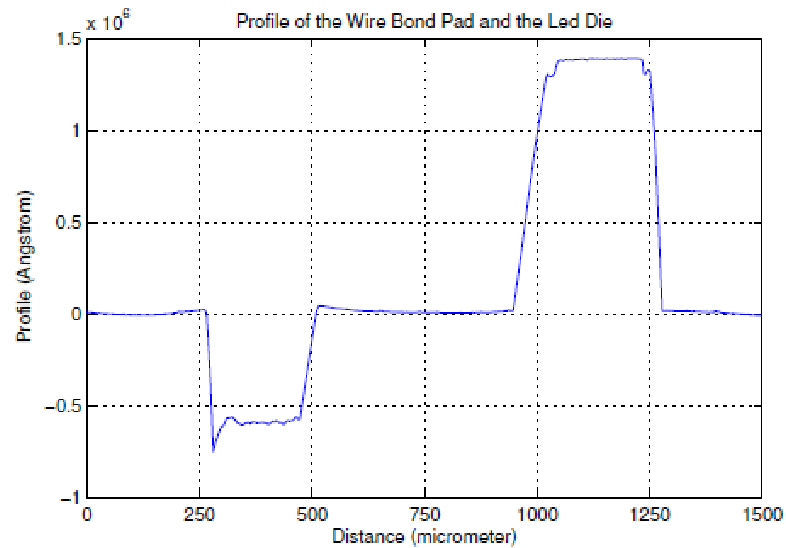

Figure 3.14. Profile of the proposed structure after LED die placement.

dimensions of 5 mm× 5 mm ×1 mm and a weight of approximately 180 mg (Type C magnet in Section 2.5.2) onto the FR4 actuator in order to define a magnetization vector on the movable parts. Finally, an off-the-shelf coil is placed beneath the mechanical device to complete actuation set-up.

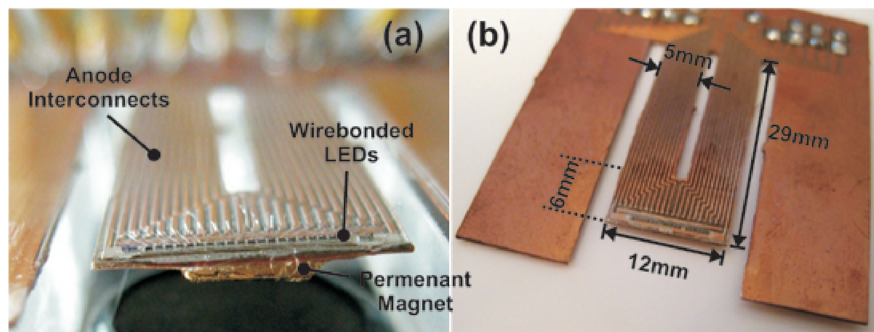

Figure 3.15. (a) Fabricated device, a close-up view. (b) Device picture with dimensions.

Fabricated device photographs are given in Fig. 3.15. As it is designed, proposed structure has two beams with a length and width of 23 mm and 5 mm, respectively. The tip of the structure is a rectangle with a dimension of 12 mm× 6 mm.

3.2.5. Power Considerations

The total power consumed in the proposed display is due to two components; the power that is required to turn-on 1D LED array and the power required to actuate the mechanical scanner. As explained earlier, the displacement of the scanner is enhanced by the quality factor when the actuation frequency enters into the pass band of the mechanical resonator. This property decreases the power consumption of the resonant type actuator. Power consumed by the LED array can be estimated by considering the current-voltage relationship of a forward biased diode, which is given as

$$I_D \simeq I_s \cdot \exp\left(\frac{V_D}{n \cdot V_T}\right) \tag{3.4}$$

where I_s is the saturation current, $V_T = kT/q$ is the thermal voltage, n is the ideality factor, V_D is the voltage across the diode and I_D is the diode current. Assuming that all the LEDs in the array are tuned on, the power consumption P_1 of a conventional dot-matrix LED display with a resolution of $N_H \times N_V$ can be calculated by using

$$P_1 = N_H \cdot N_V \cdot I_1 \cdot V_1 \tag{3.5}$$

where I_1 and V_1 are the current and the voltage of a single LED of the 2D display. Combination of equations 3.4 and 3.5 gives the power consumption of a dot-matrix LED display as

$$P_1 = N_H \cdot N_V \cdot n \cdot I_1 \cdot V_T \cdot \ln\left(\frac{I_1}{I_s}\right). \tag{3.6}$$

The proposed display uses one-dimensional LED array of $N_H \times 1$ which is scanned in the vertical axis in order to form a virtual image plane with the same resolution of $N_H \times N_V$ as the dot-matrix LED display. In the present arrangement, a single LED device is used for generation of N_H number of virtual pixels. Since there is a linear relationship between the current and the luminous intensity of LEDs [88], same levels of display luminance and contrast ratio can be achieved for both displays if each of the

LEDs of the present display is fed by a current value of $I_2 = N_V \cdot I_1$. Consequently, the power consumption the proposed display is given as

$$P_2 = N_H \cdot N_V \cdot n \cdot I_1 \cdot V_T \cdot \ln\left(\frac{N_V \cdot I_1}{I_S}\right). \tag{3.7}$$

Essentially, LED integrated scanner display of same performance consumes more power than the dot-matrix LED display. The ratio of these power levels is

$$\frac{P_2}{P_1} = 1 + \frac{\ln N_V}{\ln\left(\frac{I_1}{I_S}\right)} \tag{3.8}$$

which is plotted in the inset of Fig. 3.16. LED current-voltage characteristic is measured with Keithley 4200 Semiconductor Parameter Analyzer as shown in Fig. 3.16.

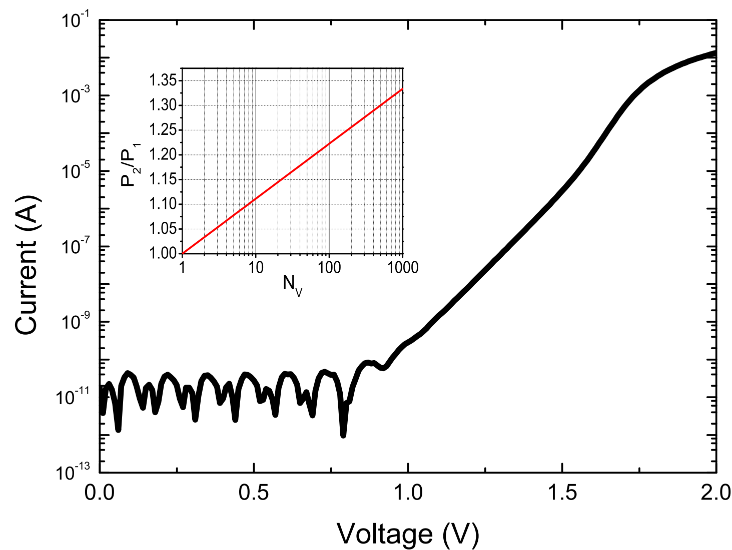

Figure 3.16. Current-voltage characteristic of a LED device used in the implementation of the display. Inset: ratio of the powers consumed by the light sources of the present display and a dot-matrix LED display for I_1=10 mA and I_S = 10 pA.

The saturation current of the LED is extracted to be approximately 10^{-11} A. As

an example, a pixel with full brightness conducts a current of 10 mA, which results in $\frac{P_2}{P_1} = 1.14$ for a row number of $N_V = 20$ and $I_S \approx 10^{-11}$. In other words, the present display consumes roughly 14% more power than a dot-matrix LED display of same size and performance. When the power consumed by the actuator is taken in to account, the power difference increases to 42%, in order to drive the 1D LED array to at its peak displacement. This extra power becomes less effective as the horizontal resolution (or equivalently the number of LEDs in the array) of the display increases.

3.2.6. Characterization and Experimental Results

The frequency response of the mechanical scanner is measured using a vibration-velocity characterization setup which consists a laser Doppler vibrometer (LDV), a function generator and an oscilloscope as shown in Fig. 3.17. Communication between the oscilloscope and the function generator is accomplished by GPIB interface. LDV sends a laser beam to the section of interest and measures the Doppler shift of the returning beam to give a voltage at its output which carries the signature of the vibration velocity of that particular section.

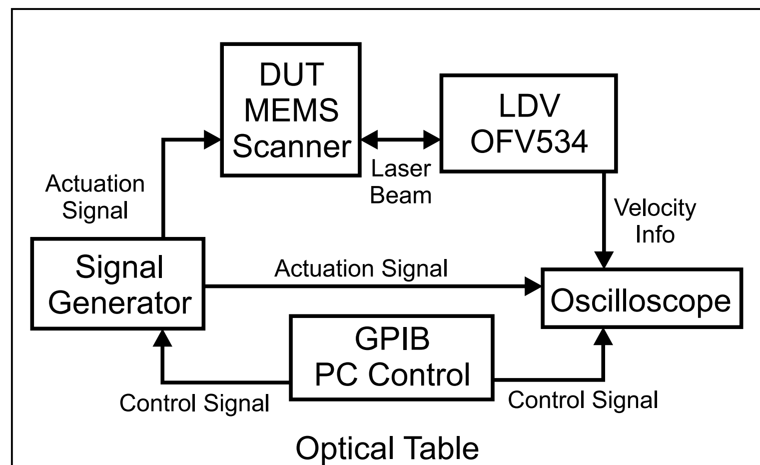

Figure 3.17. Employed characterization Setup.

Fig. 3.17 shows the mechanical transfer characteristics of the device as a function of the operation frequency. This plot is obtained by driving the electro-coil with a signal of constant power and varying frequency and collecting the vibration velocity by the LDV in ambient air. As can be seen from this figure, the slow-scan resonance peak

is approximately at 99 Hz and it corresponds to the out of plane bending resonance mode of the actuator. At this frequency, the device produces a peak displacement of approximately 2.45 mm at a drive power of 85 mW with a quality factor of 21 which is an expected value both due to relatively low elastic modulus of the FR4 material and due to the heavy effective mass of the actuator.

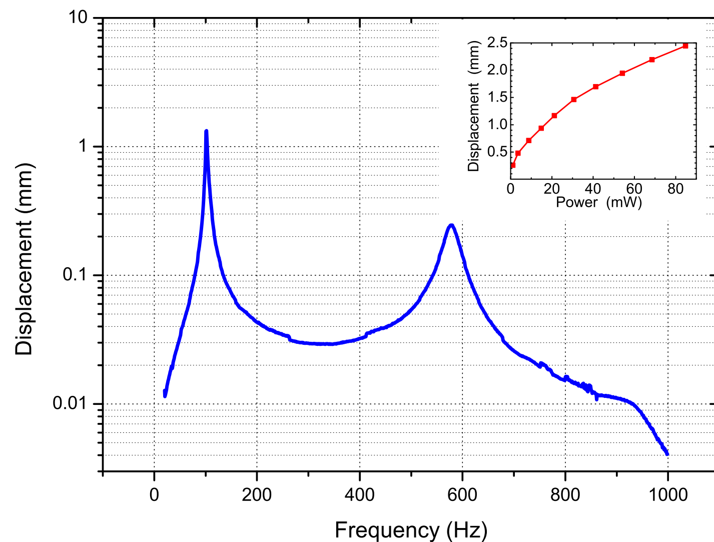

Figure 3.18. Displacement-frequency plot of the FR4 scanner. Resonance at approximately 99 Hz.

Air damping reduces the quality factor as well, but its effect is not as dominant as the aforementioned effects. The next resonance peak occurs at around 580 Hz which is sufficiently far away from the fundamental frequency such that a safe mode separation in the frequency spectrum is accomplished. Inset of Fig. 3.18 plots the peak displacement of the actuator as a function of the drive power level. As can be seen from this plot, actuator displacement is proportional to the square root of the drive power, due to the linear relationship between the displacement and the electro-coil drive current.

Since long-term reliability is a crucial issue for a composite material like FR4, reliability of the proposed display structure is validated by operating it for an extended period of time. The LED integrated mechanical scanner was operated at its resonant frequency for approximately 3×10^6 cycles at a drive power of 40 mW, in ambient air.

Scanners' resonant frequency, quality factor and displacement are measured periodically throughout the experiment within a laboratory environment open to humidity and temperature variations. Fig. 3.19 shows the measured percentage change in each measured parameter. The quality factor, Q, and the peak displacement, Z, of the scanner changes less than 5% over 3 million cycles of operation whereas the maximum deviation exhibited in resonant frequency, f_0, is less than 0.2%. It can be concluded that the important performance parameters are rather insensitive to cyclic aging [45].

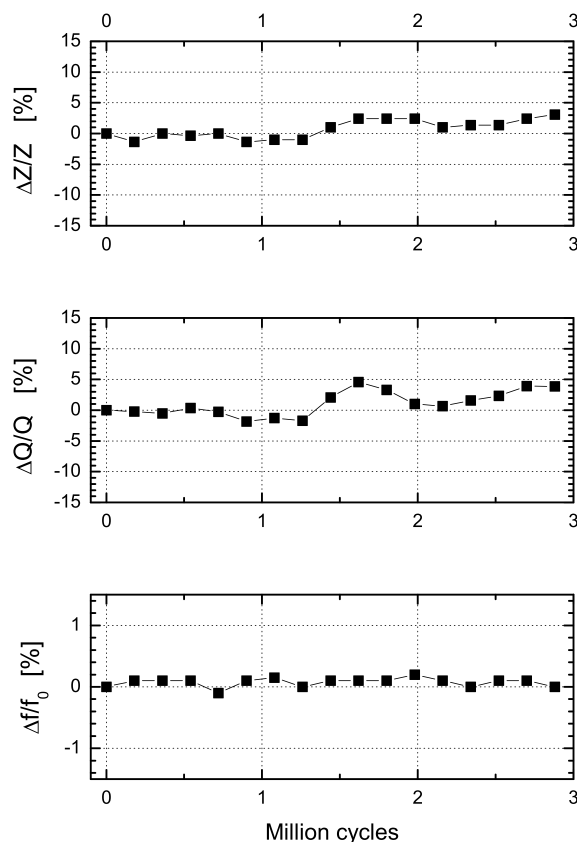

Figure 3.19. Reliability test results of the fabricated display. The device is kept at resonance for about 3 million cycles.

The realized display is tested by imaging different characters as shown in Fig. 3.20. As mentioned earlier, unilateral scanning is preferred while the nonlinear portions of the slow-scan sinusoidal signal is not used in order to obtain a non-distorted image. Consequently, approximately 8 mm×2.25 mm display which has a resolution of 20×40 pixels is acquired. In Fig. 3.20 (a), 1D array which consists of 20 individual LEDs is switched on without any actuation of FR4 scanner is depicted. The camera is set

to have a long exposure time to be able to capture the movable frame images which results in ghost images. In addition to that, a slight ghost brightness around the LED emitters is due to conical radiation of the light from the device. Next, an acronym, *MNL* is displayed in Fig. 3.20 (b). Subsequently, display is modulated to get a checker box image in Fig. 3.20 (c). A gray scale image which is acquired using pulse width modulation is depicted in Fig. 3.20 (d).

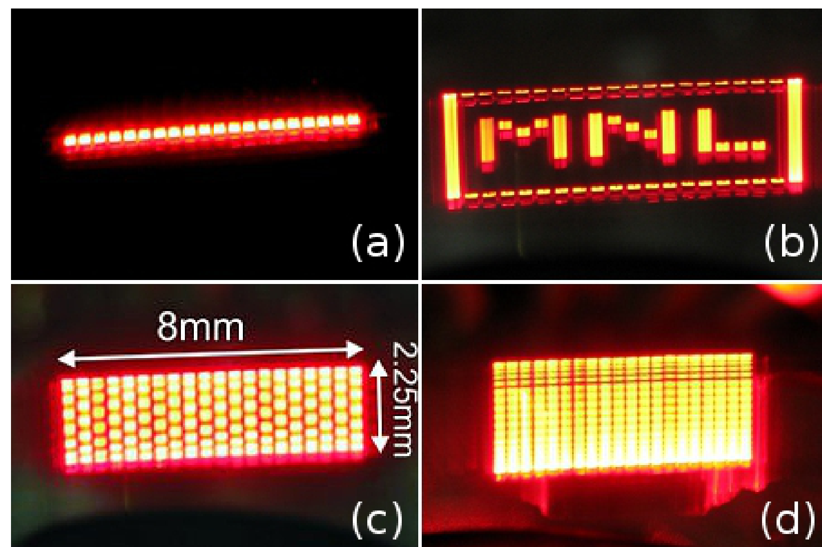

Figure 3.20. Some modulation examples: (a) With no actuation and modulation. (b) MNL (c) Checker box image. (d) Gray scale image.

3.2.7. Concluding Remarks and Discussion on Solid-State LED Array Integrated FR4 Scanner Based Displays

Proposed FR4 based displays have the advantage of having a low fundamental resonance frequency suitable to be used as refresh rate. Displacement at the slow-scan resonance enjoys the moderate quality factor of the mechanical structure. Simultaneous and precise control of this resonant movement along with the modulation of 1D LED array in perpendicular direction to the slow-scan axis enables the generation a 2D images. The scanner, fabricated using a Cu coated FR4 substrate is magnetically actuated. The display enters into its fundamental resonant movement at approximately 99 Hz and produces a peak displacement of 2.45 mm at a drive power of 85 mW. A display resolution of 20×40 pixel on a physical size of 8 mm$\times$ 2.25 mm is acquired. When considering only the LED array, the proposed display consumes 14% more power com-

pared to the conventional dot-matrix LED display of the same performance. However, when the advantage of using significantly less amount of LED devices is considered, it can be deduced that the present display offers a more reliable operation, in terms of less probable dead-pixel failure, easily controllable LED-to-LED variations. Furthermore, utilization of one-row of LED array reduces the cost arising from the usage of light sources. There are also scanning solid-state LED based displays and toys available in the market like propeller clock [89] but they are not in micro-scale and portable. Moreover, apart from being expensive, they generally require a DC motor and a large amount of power in order to work compared to our proposed display. Finally, the display is proven to be quite robust in the tests which lasted approximately 3 million cycles with no significant change (below 5%) in the performance parameters such as the quality factor, the peak resonant displacement and the resonance frequency.

3.3. Polymer LED Integrated FR4 Scanner-Based Display

Principles used in the design and realization of solid-state LED integrated FR4 scanners are also employed to form a fully polymer, scanner-based display. This time instead of solid-state LEDs, polymer LEDs (PLED) are preferred as the light sources.

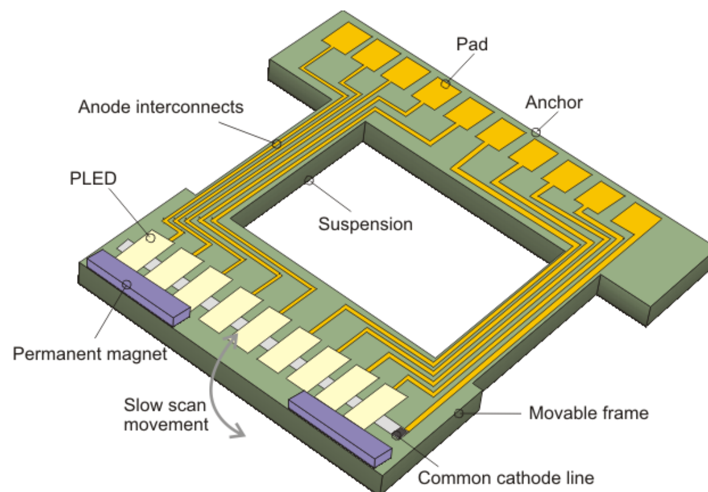

Figure 3.21. Schematics of the proposed PLED integrated FR4 scanner-based display.

Schematic of the proposed system is shown in Fig. 3.21, where an actuator suspended with two springs at the anchoring regions and an array of PLEDs placed on the

actuator surface can be identified. In the following subsections, especially the fabrication method and the experimental measurements of the targeted scanner-based display will be explained. Information on employed PLEDs will be also given in subsequent sections.

3.3.1. Design and Operation Principles of PLED integrated FR4 scanners

A design methodology very similar to the techniques that are explained in Section 3.2.1 are used while designing the targeted all-polymer, scanner based displays. Proposed FR4 scanner is making an out-of-plane displacement movement in the slow-scan axis. Related resonance frequency is designed to be 50 Hz for the refresh rate of the 2D displays. The dimensions of the proposed structure are determined as shown in Table 3.2 using the principles and equations derived in Section 2.2.2.

Table 3.2. Dimensions of the PLED integrated FR4 Scanner.

Parameter	t_f	L_f	L_t	L_{eff}	W_f	W_t
Dimension(mm)	0.23	18	15	33	4	27

The results of the finite-element analysis simulations are shown in Fig. 3.22 below. As it is desired, the fundamental resonant mode (out-of-plane bending) occurs at approximately 50 Hz. The unused adjacent mode is a torsional movement mode and it takes place at approximately 193 Hz.

3.3.2. Polymer LEDs

1D PLED arrays which are required in order to build the desired all-polymer, micro-scanner based displays, are fabricated by Prof. Mutlu's research group in Bogazici University MEMS Laboratory (BUMEMS) after our designs. Employed PLED fabrication process is briefly explained below and in some part of Section 3.3.3. More detailed information on PLED fabrication process can be found in [90].

Conjugated polymers are semiconductors that offer flexibility, simplicity, and

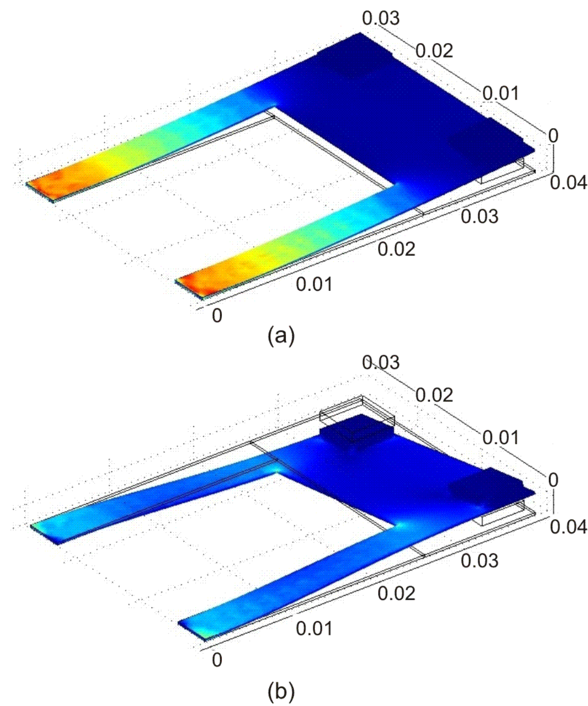

Figure 3.22. Finite-element analysis of the MEMS actuator. (a) Slow-scan (refresh rate at 49.8 Hz) movement as the fundamental mode. (b) Unused torsional movement mode at 193.4 Hz (dimensions in meter).

lower cost in the fabrication of LEDs [91], transistors [92], integrated circuits [93], charge-pumps [94], photo-detectors, and solar cells [95]. Their usage has a potential to realize monolithic integration of electronic, optoelectronic, MEMS, and sensory devices [96] altogether. In addition, polymer-based systems are amenable to roll-to-roll production [97]. However, when compared to their inorganic counterparts, current polymer semiconductor devices have lower performances, are less reliable, and have shorter lifetimes due to rapid degradation on exposure to oxygen and water vapor under ambient atmosphere [90].

1D PLED array is made with a structure of indium tin oxide (ITO), poly (3,4-ethylenedioxythiophene)poly (styrene sulfonate) (PEDOT:PSS), poly [2-methoxy-5-(2'-ethyl-hexyloxy)-1,4-phenylene vinylene] (MEH-PPV), and aluminum (Al). ITO forms a transparent anode electrode. PEDOT-PSS works as a hole-transporting layer. MEH-PPV is the light-emitting layer. Aluminum is used as a low-work function anode material. Electrons injected from Al and holes from ITO recombine on MEH-PPV to emit photons.

In contrast to typical fabrication process in literature, fabrication of the 1D PLED array is performed under standard room conditions without using glove boxes. Therefore, during each fabrication step, the polymer materials are degraded by humidity and oxygen in the environment. As a result, fabricated PLEDs do not emit light when forward biased. To remedy this situation, a novel two-step post-fabrication-treatment method, consisting of thermal and electric field treatments, is used to revive them [90]. Treatments are done on a hotplate inside a vacuum chamber with in situ packaging capability after the electrical wiring of the array is done. The PLED array is packaged with a millimeter-thick layer of a hot-melt silicone immediately after treatment without breaking vacuum. Thermal treatment restores the electroluminescent function of PLEDs by removing most of the oxygen and water vapors absorbed inside the devices. The electric field treatment following the heat treatment lowers their turn-on voltages and increases their stability, repeatability, and lifetime by reorienting and ordering polymer chains that have become mobile over their glass transition temperatures and lowering contact barriers at the interfaces of the films. Such a fabrication process is much easier and cheaper, since the equipment consisting of spin-coater, hotplate, stirrer, high-vacuum thin-film evaporator, wiring tools, and packaging tools used in the production of PLEDs does not have to be connected together inside a big glove box to secure an inert atmosphere. Fabricated PLEDs using these materials and methods typically have efficiency of around 0.1%, luminance of 5 cd/m^2, and lifetime of a couple of months.

3.3.3. Fabrication of PLEDs and PLED Integrated FR4 Scanners

MEMS actuator and 1D array of PLEDs are fabricated separately and then integrated to get the targeted 2D display. The fabrication process of the MEMS actuator is shown in Fig. 3.23. An FR4 substrate of 200 μm thickness which has 30 μm thick copper films on both sides is used as the starting material. The copper film on the front side is coated with a 4 μm thick Shipley 1828 photoresist layer. This layer is patterned lithographically, as shown in Fig. 3.23 (b).

The copper layer is then etched in HCl solution, and photoresist is stripped in

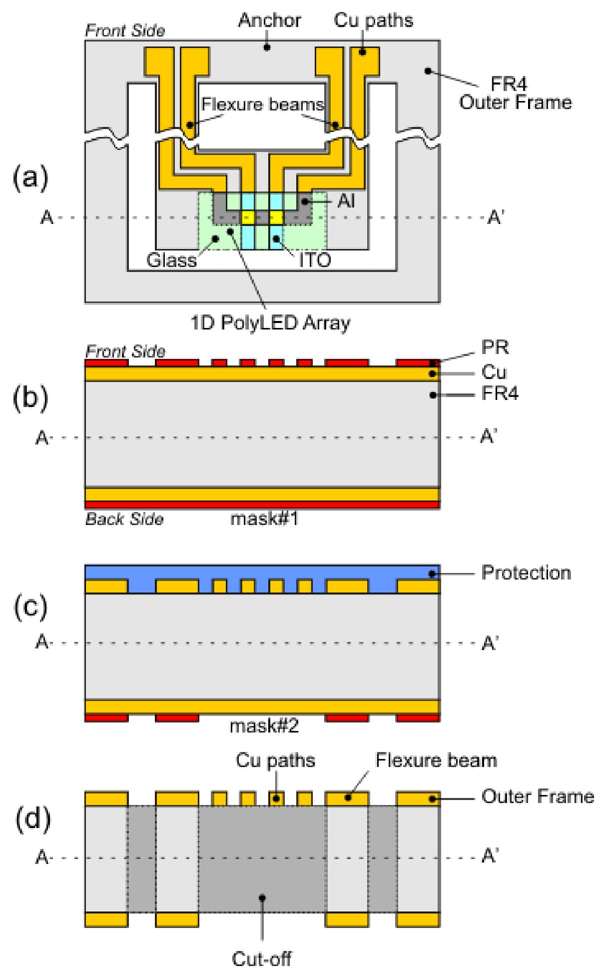

Figure 3.23. Process sequence of FR4 actuator fabrication.

order to produce the electrical paths to PLEDs. Subsequently, copper on the backside is patterned and etched in a similar way while protecting the front side of the substrate with a protection layer. Most of the copper on this side is not etched except for the paths for laser cutting, as shown in Fig. 3.24, in order to increase the stiffness and the quality factor of the MEMS actuator and also to alleviate the problem of metal fatigue in copper paths. Finally, the structure is cut by a laser cutter (Versa Laser Cutter, VLS2.30). Laser cannot cut through the copper film; hence, the pattern of the copper film on the backside forms the final shape the MEMS actuator. Window opened on the tip of the cantilever structure is required, since light generated on PLEDs can be viewed only through this window after the integration of the actuator and the PLED array.

All fabrication steps of PLEDs are performed under standard room conditions,

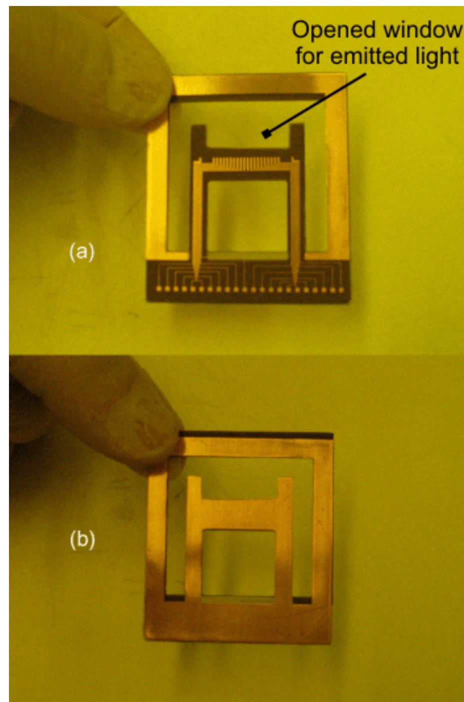

Figure 3.24. (a) Front-side and (b) backside views of FR4 actuator.

with a relative humidity level of 40%-50% and a temperature of 21°C-26°C. PLEDs are fabricated on ITO-coated polyethylene terephthalate (PET) sheets with a sheet resistivity of 35 Ω/square. The sheets are cut into circular wafer-shaped segments with diameters of 4 inch and attached to 1 μm thick glass wafers temporarily with silicone gel. They are cleaned in acetone, isopropyl alcohol, and deionized water consecutively for 3 min using an ultrasonic cleaner. The process sequence of PLED fabrication is shown in Fig. 3.25. ITO is patterned photo lithographically using 2.8 μm thick positive photo-resist and etched in a 1:1 HCl:H2O solution. To eliminate the hydrophobic nature of the PET surface against PEDOT:PSS, which is an aqueous solution, and to clean the surface of ITO from organic residuals, an oxygen plasma with a power of 20 W is used for 15 min in a 300 mtorr vacuum. PEDOT:PSS with a conductivity of 1 S/cm is purchased from Sigma as an aqueous solution. After the filtration of PEDOT:PSS with a 0.25μm syringe filter, a film approximately 80 nm in thickness is obtained on the wafer by spin-coating the solution at 2000 rpm for 30 seconds. PEDOT:PSS film is baked at 110°C under nitrogen atmosphere for 1-hr and then baked in a vacuum of 150 torr for 1-hr to remove its water content. In order to minimize thermal stress, temperature is increased and decreased gradually. This results in a PEDOT:PSS film

with a sheet resistivity of about 125 kΩ/square. Since PEDOT:PSS has four orders of higher resistivity than ITO, it is not necessary to pattern this film.

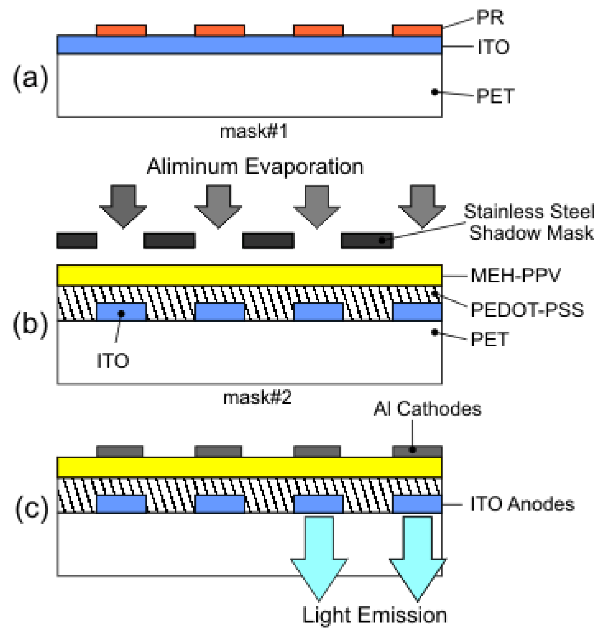

Figure 3.25. Process sequence of PLED fabrication.

Next, a 4 mg/mL MEH-PPV/toluene solution is stirred at 50°C on a hotplate for at least 4 hrs until the polymer is fully dissolved. After filtering the mixture with a 0.25 μm Teflon syringe filter, the MEH-PPV solution is spin-coated onto the wafer at 2000 rpm. Then, the film is baked at 65°C for 1 hour. This obtains a film thickness of approximately 80 nm. For the deposition of the aluminum electrodes, a shadow mask is prepared from a 100 μm thick stainless-steel (SS301) sheet. A photo-resist mask is patterned on steel surface using lithography,and then, steel is isotropically etched using electrochemical etching in 1:7 HCl:DI water solution [35]. A vacuum chamber with a base pressure of 10.6 torr is used to evaporate a 220 nm aluminum layer. The shadow mask is aligned perpendicular to the patterned ITO lines and forms 1D PLED array. Fabricated PLED array is composed of 20 PLEDs with pixel dimensions of 400 μm by 1500 μm separated by a 50 μm gap.

The increase of the second dimension of the PLED from the designed value of 800 to 1500 μm is due to the gap between the devices and the shadow mask during evaporation of aluminum. After the fabrication, one die of 1D PLED array out of

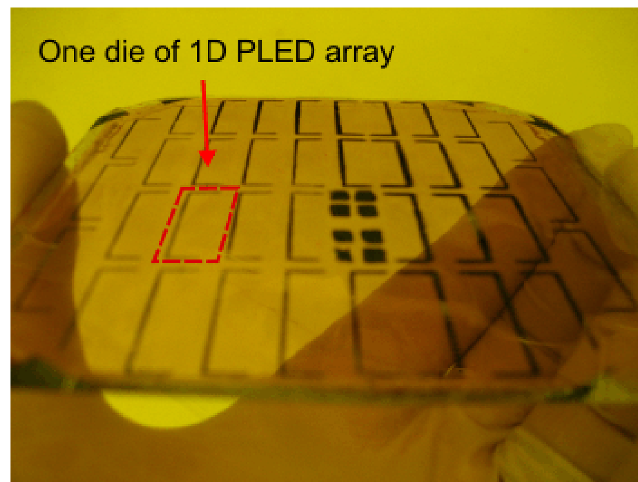

Figure 3.26. Photograph of fabricated dies of 1D array of PLEDs on PET substrate, temporarily attached to a glass wafer.

many dies on the wafer, as shown in Fig. 3.26, is cut simply using a blade and attached to the tip of the cantilever of the polymer scanner, where a window has been opened before, as shown in Fig. 3.27. Manual alignment between the array and the scanner is made such that copper lines and electrode lines of the array are matched. Silver epoxy is used to connect copper lines to the corresponding electrodes of the array, as shown in Fig. 3.27 (b).

Subsequently, post-fabrication treatments required for the PLED array are done. These are performed in a dark environment on a hotplate that is inside a vacuum of 100 mtorr. Heat treatment starts by heating the polymer system to 110°C. Temperature is changed gradually in stages to minimize the thermal stress between the layers. The duration of the heat treatment is 1 hr. Following the heat treatment, the devices are electrically reversed-biased at 0 V, meaning that anodes and cathodes are short circuited. By short circuiting an LED, its active area is reverse biased by its built-in potential, and an electric field is created across. The electric field treatment also continues for an hour at a temperature of 110°C.

At the end of treatment stages, the polymer system is packaged immediately without breaking vacuum. A layer of hot melted silicone approximately 1 mm thick is used to encapsulate only the area of the polymer system where the 1D PLED array

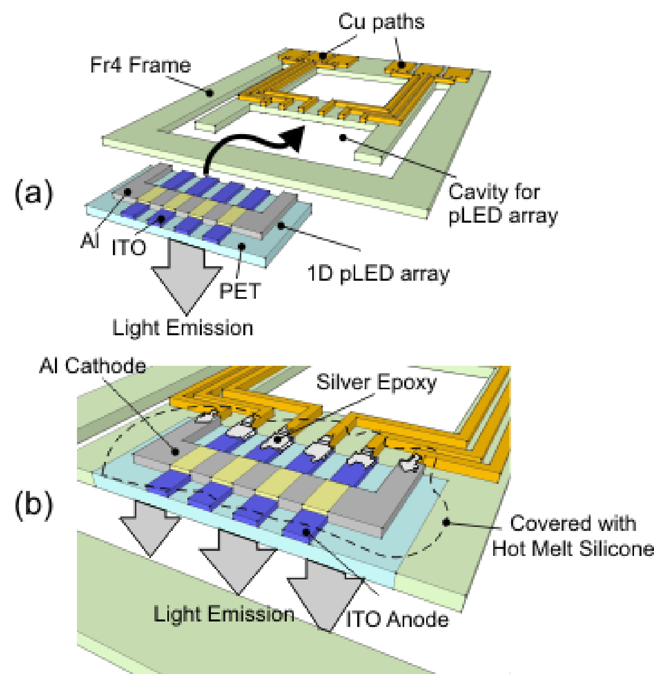

Figure 3.27. (a) Integration of 1D PLED array and MEMS actuator and (b) Zoomed view.

is attached. The silicone is melted above 90°C by turning on a separate custom-made heater, which holds solid silicone pieces. This heater is located on the surface of the hotplate. It is thermally isolated from the hotplate using glass supports. The whole setup is inside the vacuum chamber. The electrical controls for this custom-made heater and the hotplate are outside the chamber. Hot-melt silicone is preheated at 50 mtorr vacuum separately before it is used for encapsulation to remove the absorbed gasses inside. After the deposition of the melted silicone, a thin glass slide (100 μm thick) is pressed against the surface of the liquid silicone. Once the silicone cools and solidifies, it holds the glass slide and together forms a good encapsulation for the PLEDs working as diffusion barriers for water and oxygen. The light of the PLED comes out from the ITO/PET side of the substrate, and this was the reason of opening a window on the tip of the cantilever.

The fabricated MEMS display is shown in Fig. 3.28. In this figure, the cathode pads on the FR4 surface are connected together via silver epoxy, which is necessary for the coming electrical treatment of the PLEDs. These are cleaned and connected to an electronic driving circuit by soldering after post-fabrication treatments and packaging.

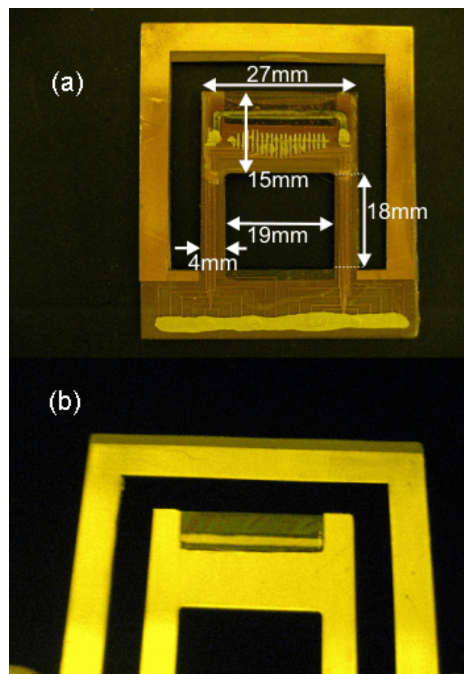

Figure 3.28. (a) Front-side and (b) backside views of MEMS display after integration with 1D PLED array.

On the front side of the display, as shown in Fig. 3.28 (a), all the electrical connections made between PLED array and copper lines of FR4 using silver epoxy can be seen. The backside of the device is shown in Fig. 3.28 (b). The aluminum pattern of the PLED array, which is on the front side, is visible on this backside view, since the PET and ITO patterns are transparent. Similarly, the emitted light of the PLEDs is visible from this side.

Implementation of the system is completed by permanently attaching two nickel-plated magnets which have the dimensions of 1 mm × 5 mm × 5 mm and a weight of approximately 220 mg onto the MEMS actuator in order to define a magnetization on the movable parts as described in the device-operation section. Subsequently, an off-the-shelf coil is optimally placed near the actuator to complete system setup.

3.3.4. Characterization and Experimental Results of PLED Array Integrated FR4 Scanner

A vibration-velocity characterization setup is again used to extract the frequency response of the MEMS actuator. In the experiments, both the coil excitation voltage (current) and the LDV output voltage are sinusoidal signals. For a given setting of the LDV, output voltage is converted to velocity by scaling it with a constant. Fig. 3.29 shows the mechanical transfer characteristics of the device as a function of the operation frequency. This plot is obtained by driving the electro-coil with a signal of constant power and varying frequency and collecting the vibration velocity by the LDV. The transfer function of the actuator is measured in ambient air for a drive level of 29 mW. As shown in Fig. 3.29, the slow-scan resonance peak is approximately at 49 Hz, which is very close to the designed value (50 Hz) of the out-of-plane bending resonance mode of the actuator. Quality factor of the device in this mode is measured as 25 in ambient air. The next resonance peak occurs at about 200 Hz, as expected from the finite-element simulation result shown in Fig. 3.22.

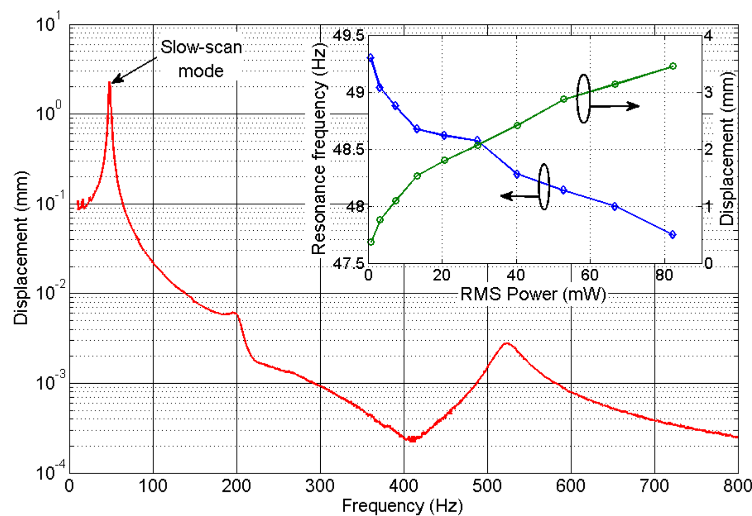

Figure 3.29. Displacement-frequency and power-resonance (inset) plots of MEMS display.

The frequency peak, present at 200 Hz, is related to the torsional movement of the actuator and is shown in Fig. 3.29. The related displacement is more than two orders of magnitude smaller than the fundamental mode, and there is safe frequency spacing

between these adjacent modes. Inset graph in Fig. 3.29 shows the displacement and resonance-frequency shift associated with the slow-scan mode as a function of the drive power level of the actuator. There is a square-root-like behavior of the displacement on the drive power. This is an expected outcome, since the magnetic actuation force as well as the displacement, according to the Hookes law, are linearly proportional to the electro-coil current. Drive power level is proportional to the square of the electro-coil current; thus, the displacement follows square-root-like characteristics. The shift in the resonance frequency is related both to the nonlinear Duffing effect and the spring-softening effect due to the behavior of the suspensions of the MEMS structure at large displacements [35]. In the slow-scan resonance mode, the actuator can generate a maximum displacement of 3.5 mm at a drive power of 84 mW, as can be read in the inset graph shown in Fig. 3.29.

The optical characteristics of PLEDs are acquired in a similar fashion to the characteristics of solid-state LEDs. They are measured using an optical setup composed of a fiber-optic spectrometer (Ocean Optics, USB 4000), integrating sphere (Ocean Optics, FOIS-1), and fiber-optic cables. For relative measurements, a bare fiber-optic probe with a 200 μm radius is used. The same fiber-optic probe is also used to determine the light spectra of the PLEDs. The luminance observed by the fiber-optic probe is measured with the spectrometer. For absolute measurements, the integrating sphere is used to capture the total luminous flux emitted from the device. Calibrations are performed with a calibrated light source (Ocean Optics, LS-1-CAL-INT). Electrical measurements of the device parameters are performed using a Semiconductor Characterization System (Keithley 4200SCS), a digital multimeter (Agilent 34410A), and adjustable dc power supplies (Hameg HM7042-5).

The emission spectrum of the fabricated PLEDs has a typical PLED spectrum shape with a peak at 600 nm in wavelength. Measured current.voltage and current.luminance characteristics of PLEDs are shown in Fig. 3.30. These devices start to emit light at 7.5 V. The difference between the thickness of MEH-PPV in this study and the one used in the aforementioned one is believed to cause this change in the results of the post-fabrication treatments. For this new fabrication conditions, post-

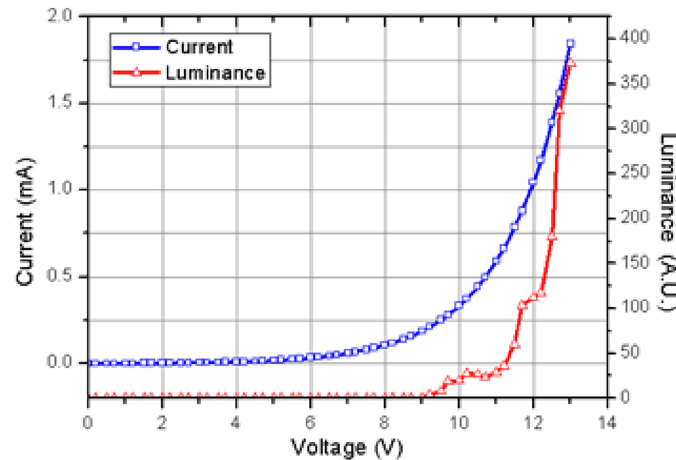

Figure 3.30. Luminance−current−voltage (L−I−V)characteristic of the fabricated PLEDs.

fabrication treatment voltages can be swept from −1 to −5 V to find the treatment voltage that gives the smallest turn-on voltage. Emitting area of an individual PLED is $400{\times}1500\ \mu m^2$. The increase of the second dimension of the PLED to 1500 μm is due to the gap between the devices and the shadow mask during evaporation of aluminum. Luminance increases as the applied voltage increases. Devices are operated at 13 V in the test of the polymer display system, each PLED consuming 1.1 mA of current. At this operation point, each PLED has a luminance of 0.3 cd/m^2. Similarly, luminance of PLEDs can be improved to our typical value of 5 cd/m^2. by changing the thickness of MEHPPV, optimizing post-fabrication treatments, and shortening the time between fabrication, system integration, and packaging.

The fabricated device can be used as a 2D display with a resolution of $M \times N$, where M is the number of light sources (PLEDs) in the array and N is the closest integer to the number defined by the ratio between the total excursion of the FR4 scanner and the 1D PLED array length. In this study, a 2D display of 9 mm × 3.4 mm is constructed as a representative device with a resolution of 20 × 7. Photograph of the display with no actuation is shown in Fig. 3.31, where a column of (1D) PLED array in emission is visible. When the actuator is excited at its slow-scan resonance mode, a 2D pattern as shown in Fig. 3.31 (b) is formed. This rectangular image, visible at the end of the cantilever, is generated by application of constant voltage to each PLED

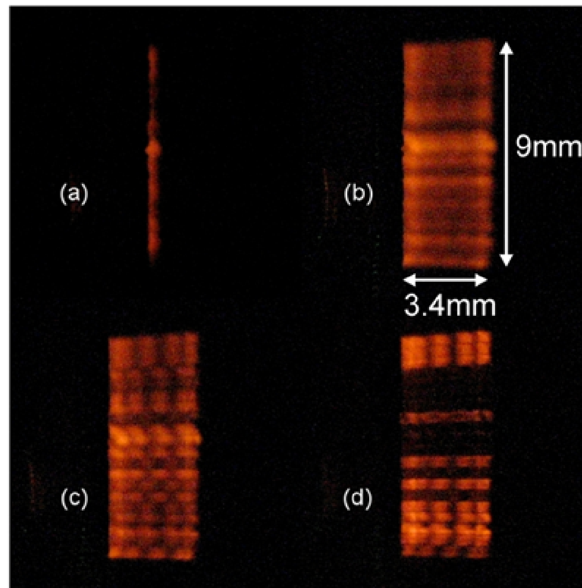

Figure 3.31. Generated MEMS display image examples. (a) No actuation and no modulation. (b) Actuated but no modulation. (c) PLED array is modulated to give a checkerboard image. (d) Pattern obtained by selectively turning off several PLEDs.

device; therefore, no compensation for LED-to-LED variation is present. As a result of that, there are brightness differences between the horizontal lines, since each PLED is responsible for scanning a single horizontal line. In addition to that, since the MEMS scanner velocity is maximized around the central portion of the image, pixels at the left and right rims of the pattern are brighter [25]. We have not programmed the pixel times to accommodate the local velocity variations of the FR actuator in this study.

Fig. 3.31 (c) shows a checkerboard pattern generated by applying a square wave signal and its 180° phase-shifted version to the neighboring PLEDs. Contrast of the display is shown in Fig. 3.31 (d) where several PLEDs in the array are turned off. As shown in Fig. 3.31, in general, basic functions of a 2D display can be implemented by using the polymer MEMS-PLED imaging system.

3.3.5. Concluding Remarks and Discussion on Scanner Based All-Polymer Display

Initial results show that this technology has the potential to implement medium resolution low-cost 2D displays. Virtual pixels of this novel display were implemented by linear vibration of the electronically modulated PLEDs in the direction that is perpendicular to the array. Two essential parts of the display, the MEMS actuator and the PLED array, were fabricated by using inexpensive processes. Characterization results of the MEMS actuator showed that peak-to-peak deflection of 3.4 mm is possible without reaching the plastic-deformation limit. PLEDs start to emit light at 7.5 V. Each PLED has a luminance of 0.3 cd/m^2 at 13 V, consuming 1.1 mA current. Resulting integrated display was tested to implement basic functions of an imaging system, and according to the initial results, it is proven that there is a great potential for a novel all-polymer medium-resolution inexpensive display.

4. STAINLESS STEEL TORSIONAL RASTER-SCANNING DISPLAYS

In the second part of this thesis work, torsional raster-scanning displays are designed and fabricated out of stainless steel. In the first part of this chapter, we present a two-dimensional mirror scanner which uses steel as the structural material. Distinctive to the present device, the scanner is fabricated by using conventional lithography and the electrochemical metal etching technique, making it different from the previously reported steel scanners along with its architecture giving better total optical scan angles (TOSA) [41]. Two different gimballed architecture is proposed, fabricated and characterized in this part.

In the second part of this chapter, a novel, self-terminating electrochemical etch process is proposed for the fabrication of scanning steel micro-mirrors. The process develops further the principles used in the first part of this chapter. It uses a single mask photolithography, and an etching step which is terminated automatically, by enabling at the same time the depth profile shaping of the fabricated structure. The proposed process is characterized and then used to fabricate two versions of 1D steel micro-scanners: one with selective thinning of the predefined parts and one without thinning. The fabricated devices are characterized and compared with respect to their resonance frequencies and mechanical quality factors.

4.1. Design and Fabrication of Two-Axis Micromachined Steel Scanners

4.1.1. Device Operation

Schematics of the proposed devices are sketched in Fig. 4.1 (a) and Fig. 4.1 (b), where a slow-scan axis which is orthogonal to the fast scan axis can be identified. The scanner in Fig. 4.1 (a) is a gimballed cantilever structure (Type-A) in which both cantilever structures generate an out of plane bending movement at their resonant

frequencies. The device in Fig. 4.1 (b), on the other hand, is a gimballed torsional structure (Type-B) where, both the mirror and the movable frame rotate about the fast and slow axis again at their resonant frequencies.

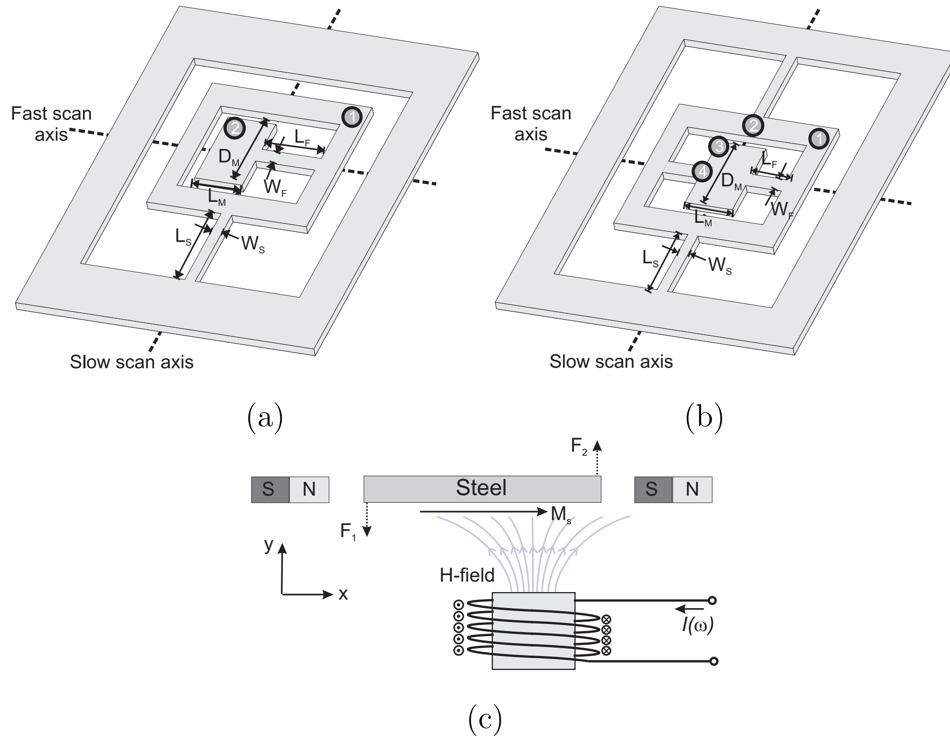

Figure 4.1. Schematics and operation of the 2D scanner devices. (a) Gimballed cantilever scanner (Type-A) (b) Gimballed torsional scanner (Type-B) (c) Magnetic actuation scheme used for both types of the devices.

The movable frame is suspended to the anchor through the springs with the length of L_S and the width of W_S, similar to a cantilever design. A mirror, with a size of $D_M \times L_M$, is gimballed to that movable frame by the suspension with a length of L_F and a width of W_F. The device given in Fig.4.1 (a), uses magnetic actuation forces to generate out-of-plane displacements. Since the electromagnetic field generating the actuation forces is varying, the most exact calculation would require point-by-point calculation or integration over the magnetic material boundaries.

However, considering the small size of the device with respect to the coil size, one can approximate these forces and use two concentrated lumped loads at point-1 (resulting in out-of-plane movement of the movable frame) and at point-2 (out-of-plane movement of the mirror). Thus, regarding the formulation that is developed in Sec-

tion 2.4, the magnitude of the induced force on the movable part can be approximated as

$$F_j(\omega) = M_s W t H_{j_\perp}(\omega) \quad j = 1, 2 \tag{4.1}$$

where M_s is the magnetization vector, W and t are the width and the thickness of the movable section being actuated by the frequency varying electromagnetic field vector $H_{j_\perp}(\omega)$, which is perpendicular to the magnetization vector. The magnetic field, marked as H-field in Fig. 4.1 (c), is generated by the electro-coil which is driven by an electrical current. The electro-coil has 7 mm inner core diameter with 2200 copper wire windings. There are two mechanically fixed permanent magnets, generating approximately 0.8 Tesla DC field, which yield a predefined magnetization of M_s in the steel section, shown as a vector in x-direction in Fig. 4.1 (c). Due to a net force difference, a moment is exerted on the steel scanner. If the rotation axis is in the middle of the lumped point forces of F_1 and F_2, the amount of the induced moment is approximately

$$T(\omega) \simeq (F_1 + F_2) L_{\text{eff}} \tag{4.2}$$

where L_{eff} stands for the length of the moment arm, calculated as the distance between the lumped force and the center of the rotation axis. There are several advantages associated with this actuation technique such as not having any joule heating due to the a.c. current on the scanner, fabrication simplicity and much greater conductor length that can be achieved by using an off-chip coil. Therefore we choose to use a miniature off-chip coil.

The most basic unit used in the realization of this raster-scanning display is the double-clamped beam with a central mass as illustrated previously in Fig. 2.2 (b). The micromechanics and the design principles of this structure is explained in a very detailed fashion through Section 2.2. Using the derived formulas in this section an excel sheet is created in order to design the structure. A sample sheet used for the design of the gimballed cantilever structure is shown in Fig 4.2.

INNER		Structure 2	Structure 1
Flexure width	2a	2.000E-04	4.000E-04
Flexure height	2b	1.000E-04	1.000E-04
Flexure length	Lf	2.000E-03	3.000E-03
Mirror thickness	tm	1.000E-04	1.000E-04
Mirror size	Dm	4.000E-03	4.000E-03
Mirror side	Lm	4.000E-03	4.000E-03
Young modulus	E	2.050E+11	2.050E+11
Poisson Ratio	v	2.900E-01	2.900E-01
Tortional Modulus	G	7.946E+10	7.946E+10
Material density	rho	7.850E+03	7.850E+03
Isotropy	mu	1.000E+00	1.000E+00
Torsional modulus-xz	Gyz	7.946E+10	7.946E+10
Torsional modulus-xy	Gyx	7.946E+10	7.946E+10
Effective inertia	Jeff	1.676E-11	1.677E-11
Mirror mass	Mm	1.256E-05	1.256E-05
Eff inertia of mirror	Jmyy	1.676E-11	1.676E-11
Flexure mass	Mf	3.140E-07	9.420E-07
Eff inertia of flexures	Jfyy	1.308E-15	1.335E-14
GK product	GK	3.634E-06	8.920E-06
Spring constant	ks	3.634E-03	5.946E-03
Resonance frequency	fr	2343.7	2997.3

OUTER		Structure 2	Structure 1
Flexure width	2A	1.000E-04	4.000E-04
Flexure height	2B	1.000E-04	1.000E-04
Flexure length	LF	5.000E-03	5.000E-03
Mirror thickness	t	1.000E-04	1.000E-04
Mirror size	D	1.200E-02	1.160E-02
Mirror side	L	6.000E-03	7.200E-03
Mirror Side	L1	5.000E-04	8.000E-04
Young modulus	E	2.050E+11	2.050E+11
Poisson Ratio	v	2.900E-01	2.900E-01
Tortional Modulus	G	7.946E+10	7.946E+10
Material density	rho	7.850E+03	7.850E+03
Isotropy	mu	1.000E+00	1.000E+00
Torsional modulus-xz	Gxz	7.946E+10	7.946E+10
Torsional modulus-xy	Gxy	7.946E+10	7.946E+10
Mass Region 1-4	M1	4.710E-06	7.285E-06
Inertia Region 1-4	Jxx1	1.130E-10	1.634E-10
Mass Region 2-3	M2		
Inertia Region 2-3	Jxx2	5.067E-14	2.618E-14
Mass Region 5-7	M5		
Inertia Region 5-7	Jxx5	7.467E-16	3.120E-15
Mass Region 6	M6	1.256E-05	1.256E-05
Inertia Region 6	Jxx6	1.676E-11	1.676E-11
Effective inertia	Jeff	1.299E-10	1.802E-10
Mirror mass	Mm	5.652E-05	6.556E-05
Eff inertia of mirror	Jmxx	6.783E-10	7.352E-10
Flexure mass	MF	3.925E-07	1.570E-06
Eff inertia of flexures	JFxx	6.542E-16	2.224E-14
GK product	GK	1.117E-06	8.920E-06
Spring constant	ks	4.469E-04	3.568E-03
Resonance frequency	fr	295.3	708.2

Figure 4.2. Automatized design sheet created in Excel. (SI units are used).

The force or the moment given in Eq. 4.1 and 4.2 displaces the movable parts of the scanner according to the Hooke's law. When the frequency of the a.c. current (thus the a.c. actuation force/torque) is around the resonance peaks of the vibration modes, the displacements are enhanced by the mechanical quality factors of the respective motion. At resonance, the displacement of the mirror can be calculated as the departure caused by the reacting spring force. Fig. 4.3 shows the finite-element analysis result of the device.

According to this analysis, movable frame's fundamental vibration mode (i.e. out of plane bending mode) can be used to generate angular displacements about the slow scan axis for Type-A scanner, as shown in Fig. 4.3 (a). This mode is designed to have a low resonance frequency since it corresponds to the refresh rate of the 2D display. The fast scan mode of the Type-A scanner has to generate a scan line that is orthogonal

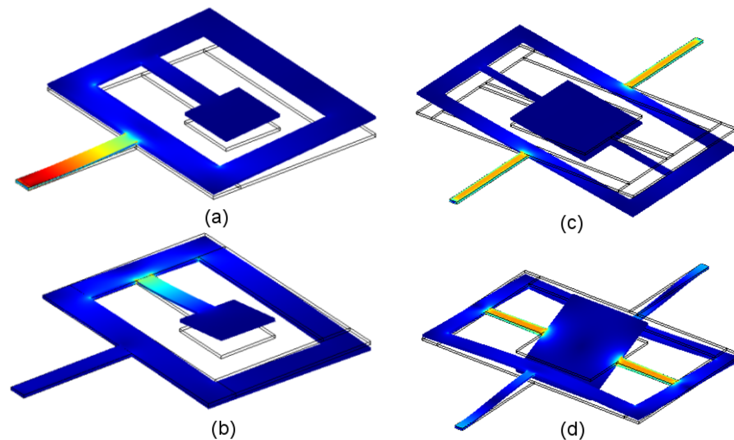

Figure 4.3. FEA results of the scanning mirrors (a) Type-A, movable frame bending mode (slow scan) (b) Type-A, Mirror bending mode (fast scan). (c) Type-B, movable frame torsion mode (slow scan)(d) Type-B, mirror torsion mode (fast scan).

to the slow-scan mode, and a suitable candidate is the out-of plane motion of the mirror as depicted in Fig. 4.3 (b). Torsional gimballed scanner (Type-B) device uses conventional torsion modes for both the movable frame and the mirror as shown in Fig. 4.3 (c) and Fig. 4.3 (d), respectively. Each of these two modes will generate scan patterns orthogonal to the other one. The slow and the fast scan modes are excited by supplying a.c. signal components at the center frequencies of the corresponding resonance peaks. The dimensions of the scanner structures are given in Table 4.1.

Table 4.1. Dimensions (in mm) of the Type-A and Type-B scanners.

Geometry	W_S	L_S	W_F	L_F	D_M	L_M	t
Type-A	1	7	3	1	3.5	3	0.1
Type-B	0.6	5	0.8	2	4	4	0.1

4.1.2. Fabrication of Stainless Steel Scanners

Application of electrochemical etching to microfabrication dates back to 1955 or even earlier, when it is used to etch germanium and silicon [98]. The cost effectiveness, reduced chemical wastes and effluents and achievable high precision make electrochemical etching increasingly popular in microsystems [99]. Many alloy compositions, such as stainless steel, can be easily etched by electro-chemical etching. Patterning of stainless steel using electrochemical etching can be serial like milling or in batch mode like

lithography. Precise electrochemical etching of stainless steel resulting in high-aspect ratio patterns with ultrashort (nano second) voltage pulses using a very sharp tip that is less than a micron away from the etched steel has been shown [100, 101]. Since this method is a serial process, machining of the work piece takes time, increasing cost. This is similar to mechanical milling, laser machining and electro discharge machining (EDM) used in industry to machine precise steel parts. A lithographic process is faster and cheaper since it is compatible with batch fabrication. Furthermore, its integration to microsystems is easier and simpler. That is why there have been research efforts to micro machine steel using a batch mode micro electro-discharge machining, where lithography and EDM is combined [102].

Similarly, in this part of the thesis, we use a novel fabrication method benefiting from the conventional lithography and electrochemical metal etching. A photoresist mask is patterned on steel surface using lithography and then steel is isotropically etched using electrochemical etching. This kind of batch mode electrochemical etching has been studied before [99]. However, it has not been used to fabricate two-axis steel scanners. Steel scanners fabricated so far are not batch fabrication compatible. They are fabricated using mechanical machining [41, 103].

The bulk fabrication method begins with a 100 μm thick, stainless steel 301 (SS301) substrate. The substrate is spin coated with a 6 μm thick Shipley 1828 photo resist mould which is soft-baked at 90°C for 60 seconds. The steel is then exposed to UV light where a nominal exposure time of 6 minutes is used with a UV light source that has a 1 mW/cm^2 power . Subsequently, the resist is developed in a developer for 60 seconds. After the development, the steel is hard-baked at 110°C for 30 minutes in order to make it more durable against the following electro-chemical etch process. To perform the electro-chemical etch, the steel layer is attached onto an insulator plate holder in order to protect the back side of the material from etching. The steel layer is immersed into an electro-chemical cell composed of 1:7 HCl:DI water solution and connected to a current source as it is depicted in Fig. 4.4 (b).

The parts to be etched form the anode electrode of the electrochemical cell.

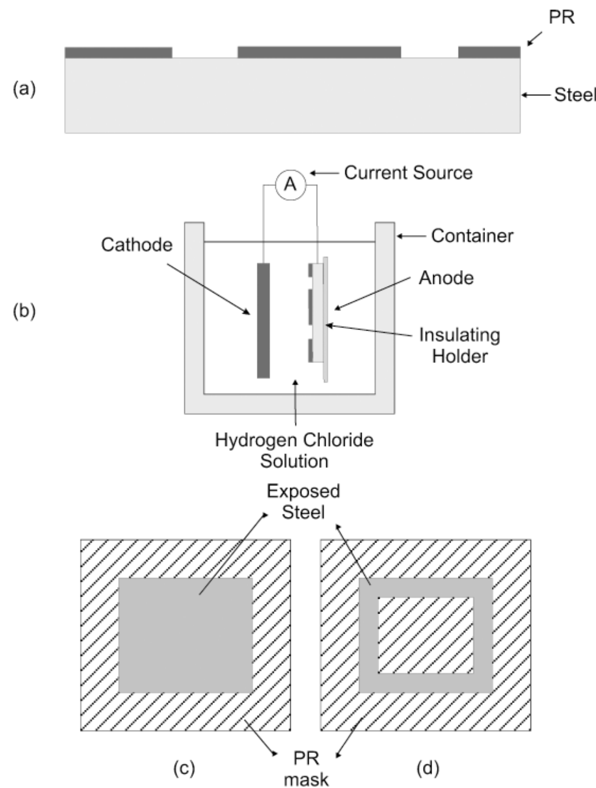

Figure 4.4. (a) 100 μm thick SS301, spin coated and patterned with 6 μm PR mould (b) Schematics of the electrochemical cell (c) Standard electrochemical etching mask (d) Electrochemical etching mask maximizing the current density.

Conversely, the counter plate, on which ions from electrolyte get deposited, is the cathode electrode and is also made of steel. They are both connected to a DC power supply which provides current to the cell. Ideally, anisotropic etching profile can be achieved by employing a slow etching, using a small current-density value. However, photoresist is not very durable in electrochemical etch solution and can be delaminated in time. Moreover, because of the poor adhesion of the photoresist on the steel substrate and insufficient post development bake, disintegration of the photoresist layer along with mask erosions occur. Consequently, these effects produce some unpredictability in the process, create surface roughness and unintentional etches on steel surface in various locations that result in poor pattern transfer. Therefore, a long period of hard baking should be preferred, HMDS adhesion promoter must be utilized and the exposure time of the resist to the HCl solution has to be diminished to get better etching results. As a result, a very quick and relatively isotopic etching process is preferred instead of slow and anisotropic one for this ultimate purpose of achieving

uniformity on the device.

The key of a quick etching process is to increase the current density. Current density can be increased by decreasing the area exposed to the solution or by simply increasing the current. Although, it is perfectly possible to use an etching mask as shown in Fig. 4.4 (c), eventually the current density would be decreased, making the process longer and destroying the etching uniformity of the device in the end. Moreover, due to the focusing of the electrolytic current distribution at the edges, non-uniform etch profiles in the form of W shape can occur in the patterns with wide openings [104, 105]. For a given maximum DC current (3.3 A in this case), and a given etch pattern, one solution would be to decrease the exposed area as depicted in Fig. 4.4 (d), which renders the same pattern as in Fig. 4.4 (c). The width of the exposed area in this mask is 100 μm but for better uniformity, smaller dimensions can be used with ease. It is important to note that this situation is only true for etch-through processes. This masking scheme enables the etching of 100 μm thick stainless steel plates with a current density of approximately 9 A/cm^2. This creates a 1-to-1 isotropy which means that approximately 100 μm undercut occurs for 100 μm depth. However, the undercut can be compensated with no trouble by simply drawing the masks accordingly. The devices are etched in just, 4 to 5 minutes with a rate of approximately 25 μm/min depending on the structure.

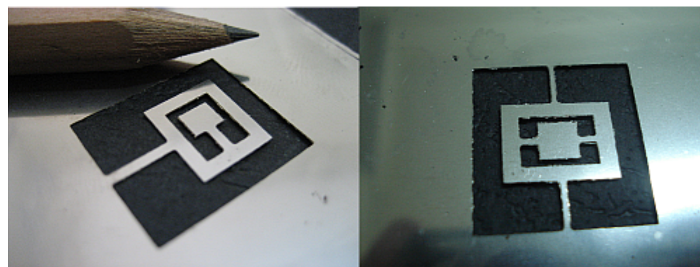

Type-A Type-B

Figure 4.5. Pictures of the two different designs. Type-A, gimballed cantilever scanner. Type-B, gimballed torsional scanner.

Finally, after electrochemical etch, the PR mould is stripped off. Produced devices are shown in Fig. 4.5. Two nickel-plated magnets which have the dimensions of

1 mm×5 mm×1.5 mm and weight of 55 mg are attached onto the anchor frames of the devices in order to be able to define a magnetization on the movable parts. An off-the-shelf coil is optimally placed near the steel mirror for actuation.

4.1.3. Test and Characterization Results

Fig. 4.6 shows the mechanical transfer characteristics of the Type-A device as a function of the operation frequency. This plot is obtained by driving the electro-coil with a constant magnitude current, varying the frequency and collecting the vibration displacement by the LDV (Polytec OFV 2500). As can be seen from this figure, there are two points of interest on the device, namely point-1 and point-2 (whereas the characterization of the torsional-torsional structure is made considering 4 different points in order to increase the accuracy of the results, refer to Fig.4.1 (a) and Fig. 4.1 (b) for the locations of these points), which indicate the slow-scan and the fast-scan operations respectively.

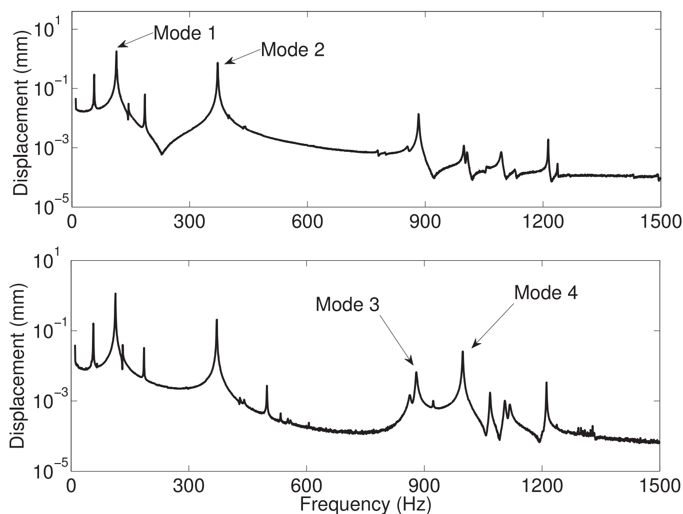

Figure 4.6. Vibration displacement of (a) the movable frame and (b) the mirror of the Type-A scanner as a function of frequency.

Mode-1 corresponds to the out of plane displacement of the movable frame at point-1, generating a scan line at 112 Hz. This resonance peak, given in Fig. 4.7 (a)

in detail, results in a quality factor of 287 in air. Mode-1 is chosen as the slow-scan mode for two-dimensional scanning. Mode-2 corresponds to the torsional movement of the movable frame which has a resonance frequency of 371 Hz. Subsequently, point-2 is used in the following measurements to define the characteristics of the fast-scan operation. The mirror produces the maximum scan line by making an out of plane displacement at 882 Hz which is defined as Mode-3 in Fig. 4.6 (b). This resonance peak generates a scan line that is orthogonal to the scan line produced by the Mode-1, thus can be chosen as the fast scan operation mode. Mechanical quality factor for this mode is measured to be approximately 200 in air. Mode-4 in Fig. 4.6 (b), depicts the torsional movement of the mirror. For the Type-A scanner, fast scan frequency (mode-3) to slow scan frequency (mode-1) ratio is 7.87 for resonant actuation of both modes. If non-resonant actuation is used for the slow-scan, e.g. 60 Hz refresh rate, the ratio between the fast scan frequency and the slow-scan frequency becomes 14.7, which implies that one can write approximately 15 lines in the vertical direction using the present device as a 2D display.

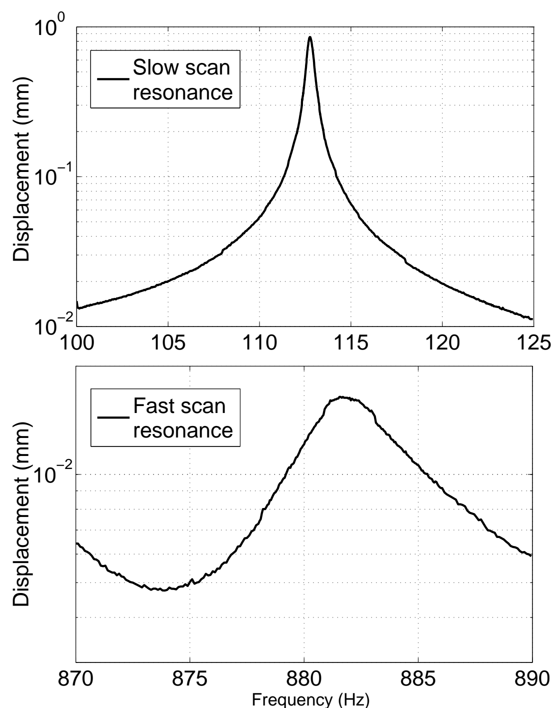

Figure 4.7. (a) Out of plane displacement resonant peak of the movable frame (b) Out of plane displacement resonant peak of the mirror for the Type-A device.

Fig. 4.8 shows the laser scanning experiments of the Type-A scanner. The laser beam is positioned on the mirror and the device is actuated in slow and fast scan resonances, respectively. A white, scaled metric screen is placed as a screen for the 2D scanner, where reflected laser beam generates one-dimensional scan line for each axis. As can be seen from Fig. 4.8 (a), the slow-scan motion produces a scan line corresponding to a total optical scan angle (TOSA) of 11.7° at the drive power of 42 mW. Similarly, the fast scan operation at the drive level of 30.6 mW results in a TOSA of 23.2°, as shown in Fig. 4.8 (b). Here, it is important to note that with large optical scan angles, steel mirror dynamic deformation, which produces slightly curved edges on the scan lines, is more apparent as shown in Fig. 4.8 (a) and (c). In order to characterize two dimensional scanning capability of the scanner, slow and fast scan drive signals are superimposed resulting in Lissajous pattern shown in Fig. 4.8 (c). Similar experiments are repeated for the Type-B device. As a result, slow-scan motion of the Type-B scanner has a TOSA of 76° at a drive power of 37 mW whereas the fast-scan motion has a TOSA of 5.9° at a drive power of 39 mW as it is shown in Fig. 4.9.

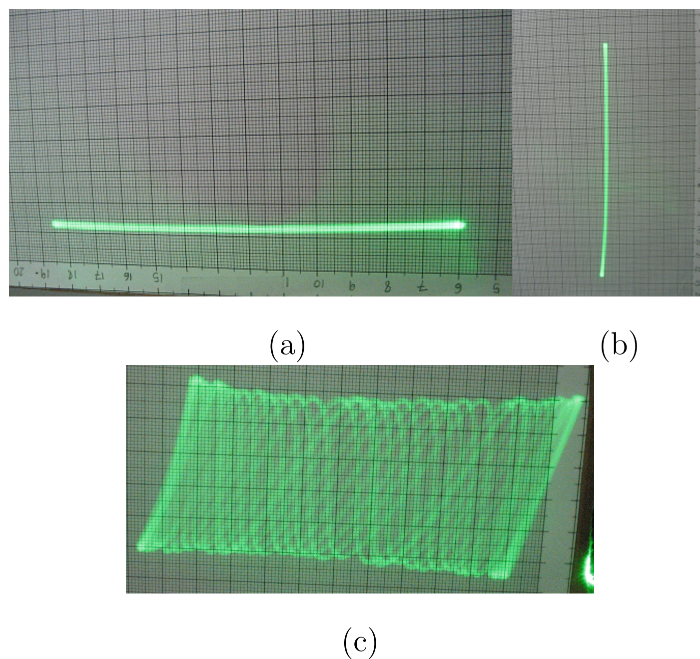

Figure 4.8. Scan line characterization results for Type-A device: (a) Horizontal total optical scan line is 11.7° at a drive power of 42 mW (b) Vertical total optical scan angle is 23.2° at a drive power of 30.6 mW(c) Lissajous pattern.

Actuation power linearity is studied for both types of scanners. The experiment is performed by cranking up the drive power of the coil and measuring the scan line (thus the optical scan angle) at each data point at the resonance peak of the mode. The result of this experiment is given in Fig. 4.9, where TOSA of the slow and fast scan modes are plotted versus the power of the driving alternative signal of the electro-coil. As can be seen from Fig. 4.9 (a), for the Type-B scanner, since the mirror displacement is linearly proportional to the magnetic flux (and therefore the coil current), there is a dependency resembling a square root relationship between the scan angle and the drive power. Since the mechanical quality factor of the device varies with the actuation power, there is no exact square root behavior. Fig. 4.9 (b) shows the characteristic for the fast axis of the Type-B scanner, where the drive power is changed in a smaller range, resulting in a similar behavior like the slow axis. As can be seen in Fig. 4.9, a maximum slow axis TOSA of 105° is possible with Type-B device. It is apparent from these experiments that the drive power is linearly proportional to the square of the TOSA.

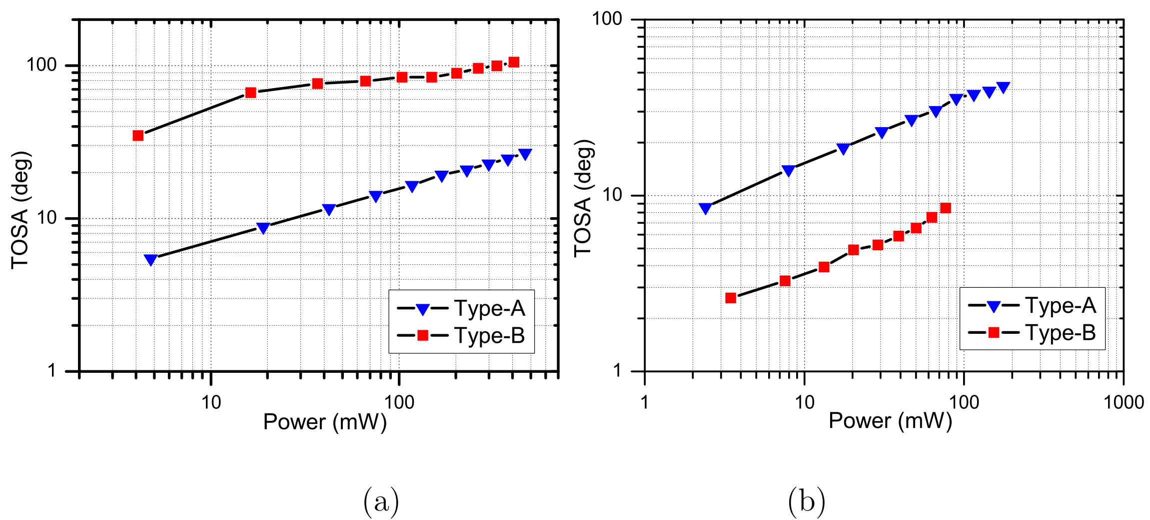

(a) (b)

Figure 4.9. Drive power versus total optical scan angle (TOSA) relationship for the cantilever type gimballed (Type-A) scanner and the torsional type gimballed (Type-B) scanner (a) Slow scan characteristics (b) Fast scan characteristics.

4.1.4. Simultaneous Actuation Control

Actuation of the scanner and modulation of the laser source is done via a control circuit whose schematic is shown in Fig. 4.10. The circuit is composed of a Spartan 3AN FPGA development board and additional active and passive components in order to convert data and drive the coil and laser diode. The FPGA board acts as the main control unit and generates both the modulation and actuation signals as digital words. The digital actuation signal, generated in the FPGA, is then converted to an analog signal via a digital-to-analog converter (DAC) which drives the electro-coil.

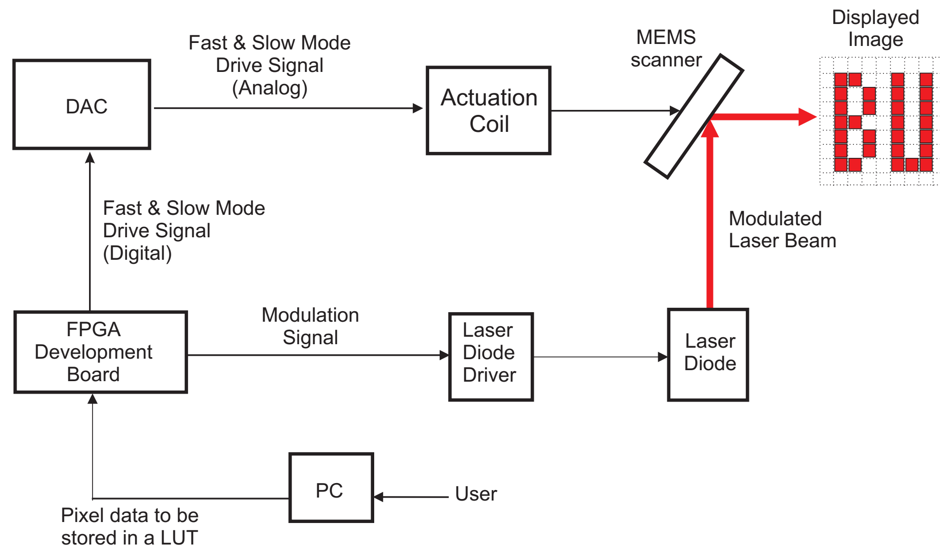

Figure 4.10. Test setup used for modulation of the light source and the drive control of the electro-coil.

The actuation signal is basically a combination of two individual signals, namely slow-scan mode and fast-scan mode actuation signals, which are superimposed by the FPGA set. Both the mode signals and the resulting superimposition have 8-bit depth. The frequency data that is employed for the generation of the signals is stored in the ROM of the development board and it can be adjusted by knobs and buttons of the board, in real time. The fast scan mode is driven to resonance, while off-resonance driving is applied for the slow-scan mode operation. The slow-scan mode signal comprise of a simple ramp signal at 100 Hz. The fast-scan modulation signal is a pure sinusoidal signal at 1.2 kHz and it is created by using sine values stored in a

look-up-table (LUT). Synchronizing the actuation signals appropriately and keeping a constant phase between them are crucial, since they define the position of the rows and columns of the display along with the contrast ratio of the image to be created. Two different methods can be pursued to accomplish this; (1) to make one of the actuation signals an integer multiple of the other (off-resonance actuation) [24] and (2) to use a synchronous pulse obtained from a feedback loop of one signal in order to start the other one (resonant actuation) [41]. The first method may need the amplification of the off-resonance signal. On the other hand, for the latter one, starting one signal abruptly may create harmonics which actuate unwanted modes of the scanner and the result of this can be a distorted image. In this work, the second method is used. The synchronization signal which starts the first fast scan operation is created when the slow scan mode operation is finished. The distortions are minimized by adjusting the slow-scan frequency accordingly.

4.1.5. Modulation of the Laser Source

The modulation of the light source is performed by a buffer, which drives the laser using an input signal from the FPGA board. Modulation signal is created from the information related to the fast scan and the slow scan actuation signals. The beginning of the fast scan signal corresponds to the creation of the first pixel for that particular row. Moreover, the value of the row counter located in the FPGA kit is increased at the beginning of each fast scan period until the end of the slow-scan period. The nonlinear portions of the fast scan mode sinusoidal signal are not used in order to obtain a non-distorted image. The number of pixel for one row is virtually limited by the laser spot size. The pixel clock frequency, which plays an important role in achievable resolution, is dependent on the physical characteristics of the laser diode, the performance of the modulation circuitry and the target contrast level [106].

Both, unilateral and bilateral scanning is possible for the MEMS scanners and they are investigated in detail in [41]. As it is mentioned earlier, the scanner velocity is highest at the center of the mirror and therefore the pixels at the center are larger. Some form of velocity compensation should be used to achieve the best image quality.

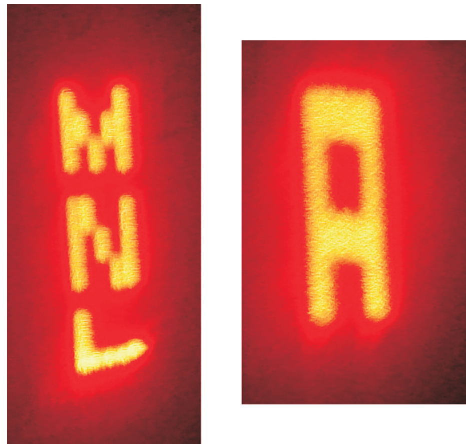

Figure 4.11. Two examples of the displayed character patterns; the left one is "MNL" text (size: 4 mm×12 mm) and the right one is the "A" character.

The characters shown in Fig. 4.11 are formed by applying unilateral scanning with no velocity compensation. The mirror under test is shown in Fig. 4.12. A hard-plastic holder, produced from a plexiglass substrate by employing a laser cutter, is implemented to prevent energy loss mechanism through the anchor points.

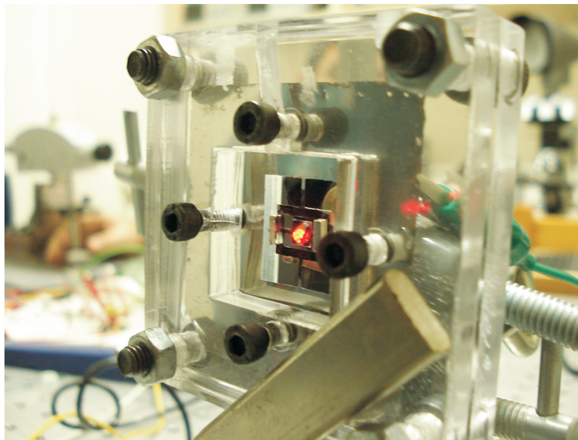

Figure 4.12. Photo of the experimental control setup.

4.1.6. Concluding Remarks on Two-Axis Micromachined Steel Scanners

In this part of my thesis, a new fabrication alternative is presented for steel micromachining. The fabrication method uses only one photomask and a single lithography step followed by an etch step. Reasonable etch uniformity with an etch rate of

25 μm/min is obtained. A family of scanners are fabricated and two of these scanners, afore mentioned gimballed cantilever (Type-A) and gimballed torsional (Type-B) devices, are presented and shown that they are capable of being used in the display applications. Presented devices in this work are the first two-dimensional steel micro mirrors. Type-A device gives a maximum TOSA of 11.7° in the slow scan axis and 23.2° in the fast scan axis in its resonance modes (112 Hz for slow scan movement and 882 Hz for fast scan movement) at a drive power of 42 mW and 30.6 mW, respectively.

On the other hand, Type-B device in resonance, generates a fast scan TOSA of 5.9° and a slow scan TOSA of 76° for drive powers of 39 mW and 37 mW, respectively. The scanner devices are operated in ambient air and resulting mechanical quality factors for the scan modes are sufficient ($Q > 100$) to have low power consumption. For the Type-A scanner, fast scan frequency to slow scan frequency ratio is 7.87 for resonant actuation of both modes. If non-resonant actuation is used for the slow-scan, e.g. 60 Hz refresh rate, the ratio between fast and slow scan frequencies becomes 14.7, which implies that one can write approximately 15 lines in the vertical direction using the present device as a 2D display. Experiments showed that the drive power is approximately proportional to the square of the total optical scan angle.A simple two dimensional display system is constructed by using the fabricated steel scanner and accompanying driving and signal processing circuitry. Obtained images shows the potential of the steel scanners in imaging applications.

4.2. Performance Enhancement in Micro-scanners Through Depth-Profile Shaping

Many different MEMS applications including optical micro-scanners require structures with varying thicknesses to improve their performances. Conventional micromachining technologies such as surface micromachining [107], bulk micromachining [59] and LIGA [108] are not always sufficient to shape the profile of micro structures and to fabricate curved 3D surfaces. A number of attempts have been reported to make out-of-plane curved surfaces on substrates like silicon, polymers and glass using methods such as inclined/rotated UV lithography [109], micro-stereo lithography [110], im-

age mirroring to create etch enhanced areas [111], femto-second laser microfabrication using direct laser writing and holographic recording [112] and electroplating fabrication [113]. However, these methods do not have the full ability to build complete and real 3D structures on metal substrates in a simple and cheap way.

Main focus of this part of my thesis work is to shape a stainless steel substrate to different depths using a simple and quick process in order to enhance their performances. A fabrication method that benefits from the conventional lithography and electrochemical metal etching to produce micromachined steel scanner is presented earlier throughout Section 4.1. We developed this method further and proposed a novel fabrication process which is self-terminating and uses stainless steel as the structural material. This method also enables having structures with different thicknesses on the same substrate using a single mask lithography step and utilizing electrochemical etch lag. The depth of etch is changing for different widths of mask openings due to etch lag [114]. An etch mask is designed such that openings defining the frame boundary of the mirror die have the fastest etch rate, whereas the openings for the areas where thinning is desired have slower rates. The etch stops automatically as soon as the frame of the device is etched through, which cuts electrical current to the piece. At that point, thinning of desired areas are obtained as well.

In order to get a correct set of process parameters to acquire spring beams and masses with the desired thicknesses, first, electrochemical etch lag of steel is characterized. Based on these results, a photomask is designed to realize devices with selective thinned areas. Devices that are fabricated using this method can be used as micro mirrors in resonant mode and also as inertial sensors.

Subsequent subsection explains the proposed electrochemical etching process and shares its characteristics. Moreover, it gives in-depth details on the fabrication of the targeted 1D steel scanner structure. Then the following subsection is dedicated to the characterization and experimental results of fabricated devices. Finally, concluding remarks and outlook are provided in the last subsection.

4.2.1. Self-Terminating Fabrication Process of Stainless Steel Scanners

In order to characterize the etch process, and to supply experimental data to device designs, a series of etch tests are performed. The etch rate and anisotropy of the process for various current density values and electrode gaps are the important parameters of the process to control the depth profile of the device. Test substrates (stainless steel type 301) given in Fig. 4.13 are prepared by first spin coating 15 μm of SPR 220-7.0 positive photoresist on them and then patterning the photoresist layer using photolithography. Square openings of various dimensions ranging from 30 μm$\times$30 μm to 3 mm $\times$3 mm are formed on this test wafer to investigate the feature size dependent etch rate.

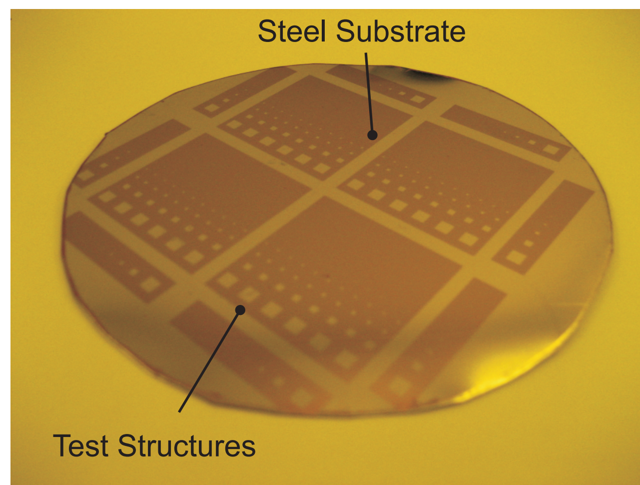

Figure 4.13. Test wafer used in the characterization of the etching process.

The electrochemical etch setup that is employed to etch the stainless steel substrate is depicted in Fig. 4.14. This setup is very similar to the setup depicted in Fig. 4.4 (b) which is used in Section 4.2.1 with some minor changes. In the first set of experiments, 1:7 HCl:DI water solution is used in the setup as the electrolyte. The sample to be etched and the counter electrode are both immersed into the solution as shown in the figure. The back side of the sample is protected against electrochemical etching using duct tape. Initially, the etch rate and the anisotropy of the process is characterized using different values of current densities for a constant electrode gap of 6 mm. A current density ranging from 1.5 A/cm^2 to 7.5 A/cm^2 is applied to the test

setup. Etch duration for each current density is adjusted such that the total amount of charges delivered to the electrochemical etch cell during the tests are equal to each other. Etch depth and the related undercut values of the square openings are carefully measured by using a measurement microscope (Nikon MM400L).

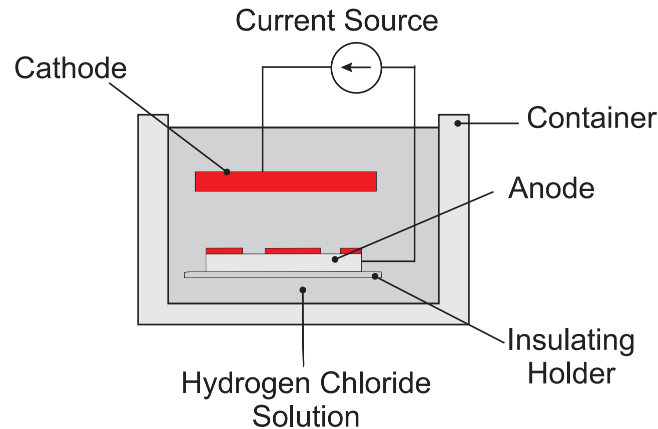

Figure 4.14. Electrochemical etch setup used in the proposed process.

The photoresist mask can stay stable for approximately 15 minutes in this HCl solution. Etch rate of stainless steel in this solution for 3 A/cm^2 current density is around 39 μm/min for a square opening of 500 μm $\times$ 500 μm and for an electrode gap of 3 cm. With this etch rate, it takes around 5 minutes to etch through a 200 μm thick steel substrate, which can be tolerated by the photoresist mask. Therefore, a 3 A/cm^2 can be considered as an optimum value of current density to minimize the etch-mask erosion. In the second set of experiments, 20% (by weight) NaCl:DI Water solution is used as a neutral electrolyte in the electrochemical etch setup to investigate the tolerance of the photoresist while immersed in the solution and to compare anisotropy and etch rate values of the setups. It is found that the etch rate of SS301 in this solution for a 3 A/cm^2 current density is around 41 μm/min again for a square opening of 750 μm $\times$ 750 μm and for an electrode gap of 3 cm. Moreover, photoresist mask stays stable for much longer time in the solution compared to HCl solution.

Etch tests reveal that average roughness goes down from a top value of 16 μm to 1 μm as the widths of the square openings decreases in HCl electrolyte. Similarly, the roughness is reduced from a top value of approximately 8 μm for a square opening of

750 μm $\times$ 750 μm to 0.5 μm as the widths of the openings decrease in NaCl neutral electrolyte. The improvement of the roughness with the decrease of opening size can be explained with enhancement of the electrolytic polishing effect inside smaller openings as discussed in [105].

One disadvantage of using NaCl solution in electrochemical etching compared to HCl solution is the formation of byproducts that do not dissolve during the etch process. This contamination becomes more pronounced if a smaller electrode gap and a small current density is used, since it gets more difficult to remove the byproducts from the locations where they are generated.

Following this experiment, a constant current density of 3 A/cm^2 is applied to the samples for 5 minutes with a DC current source in the rest of the process characterization tests. Different values of electrode gap ranging from 3 cm to about 22 cm between the steel sample and the counter electrode are also characterized in these tests. The data acquired from these experiments can be seen in Fig. 4.15.

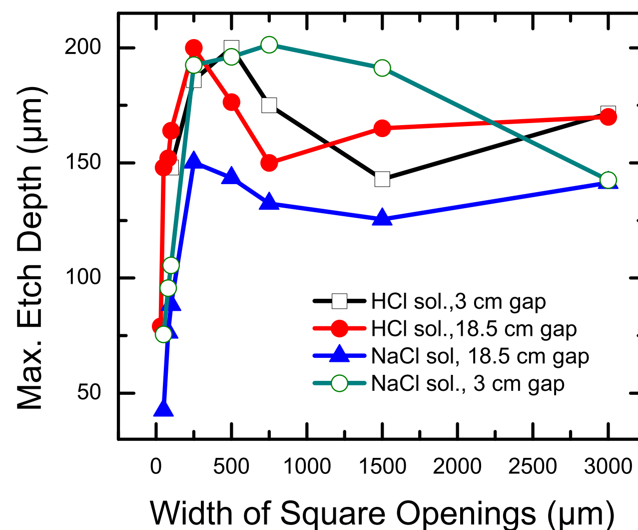

Figure 4.15. Etch depth as a function of square opening widths for different electrode gaps at a current density of 3 A/cm^2 and for an etch time of 5 min.

As can be seen from this plot, there is an optimum opening size of approximately 500 μm $\times$ 500 μm for HCl solution and 750 μm $\times$ 750 μm for NaCl solution that results in maximum etch rate in electrochemical etching. Almost the same behavior is noticed

in the experiments with different electrode gaps. Larger and smaller square dimensions than this optimum value result in significant reduction in etch rate. For dimensions smaller than 500 μm in HCl solution or 750 μm in NaCl solution, etch rates start to decrease, since etching becomes mass transport limited. The transport of chemical reactants and byproducts are getting increasingly difficult for smaller dimensions. Consequently, the etch rate decreases for smaller dimensions.

On the other hand, for dimensions larger than the optimum value, the edge effect which provides higher etch rates at the edges of the square openings due to higher electric field densities becomes negligible compared to the etch rates in the rest of the opening area. Current crowding at the edges is a well known concept which states that electrical field at the edges are stronger than the ones towards the center of opening. In other words, the etch rate at the edges is bigger than the rest of the etched areas. As the square dimensions get larger, this effect eventually becomes negligible. The ratio of edge surfaces to the overall area of the openings gets smaller and the etch rate of the center becomes dominant. Consequently, the overall etch rate decreases as the dimension increases from the optimum point.

Fig. 4.16 (a) and Fig. 4.16 (b) show etch depth and etch anisotropy, respectively, in NaCl solution as a function of current density for different opening widths with an electrode gap of 6 mm, respectively.

These results support the fact that the shaping of the wafer in the third dimension is possible by choosing the dimensions of the etch openings according to the etch rate data acquired. Fig. 4.17 depicts the profile of a sample when it is etched using a mask with two different opening sizes; one of them represents the optimum opening size and the other a smaller opening size to thin the thickness of the device.

This way, a substrate can be thinned down or curved surfaces can be formed by simply tailoring the etch openings accordingly. Fig. 4.17 (b) illustrates the resulting cross sectional profile, where a substrate is etched through at the locations of optimum openings, and thinning is performed in the same etch interval by forming much smaller

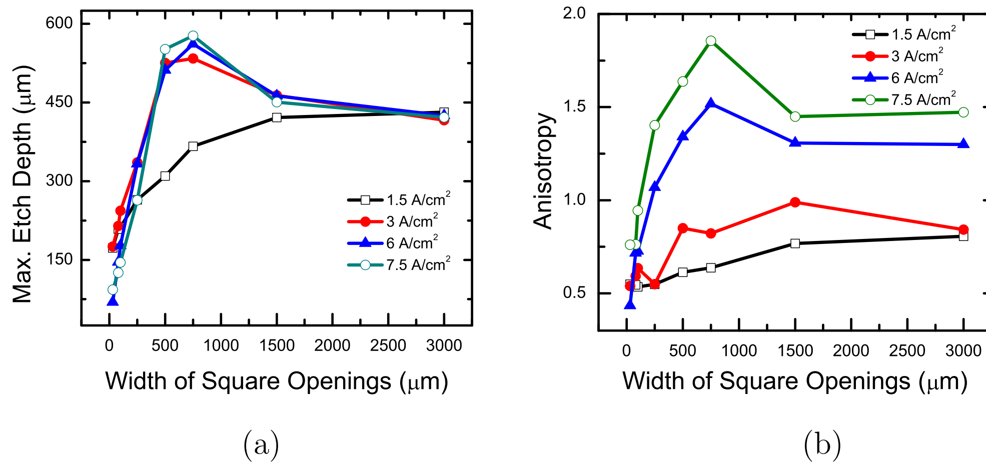

Figure 4.16. (a) Etch depth versus width of square openings for NaCl solution (b) Anisotropy versus width of square openings for NaCl solution for an electrode gap of 6 mm.

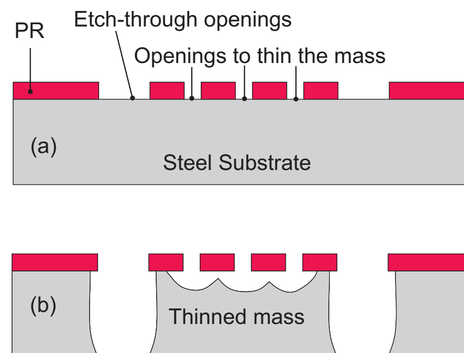

Figure 4.17. Process Profile, (a) openings in the photoresist (PR) mask are formed both to etch-through the substrate and to thin the mirror mass. (b) Profile of the device after electrochemical etching.

etch opening in the resist mask. In order to utilize this fact, a new masking scheme shown in Fig.4.18 (b) is proposed. The areas that are to be protected against standard electrochemical etching are covered with a resist mask (Fig.4.18 (a)) whereas in the proposed method shown in Fig. 4.18 (b), in addition to the conventional masking, most of the open-to-etch area is also protected to increase current density.

The gap W_2, shown in Fig. 4.18 (b) defines the mirror, and it is designed to be approximately 500 μm to ensure an etch rate greater than any other area of the sample. On the other hand, the gap W_1, which defines the frame of the mirror, is designed to be slightly smaller than W_2 to ensure that the inner gap between the flexures/mirror and

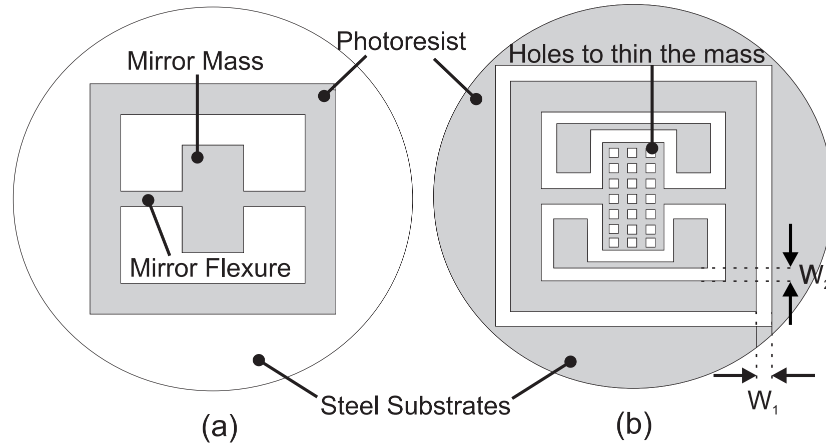

Figure 4.18. Masking schemes: (a) Typical electrochemical etching mask, (b) Proposed masking scheme.

the frame etched through first compared to the frame itself. Since electrical connection to the etching setup is made at the edge of the wafer, the complete etch of the gap W_1 cuts the electrical connection of the sample to the setup and automatically terminates the electrochemical etch process. It is important to note that while etch process at W_1 and at W_2 regions progress with a larger etch rate, the mirror mass is thinned down due to the smaller etch rate of 50 μm wide openings. Small holes on the mirror mass are connected to each other during the etch due to undercuts as shown in Fig. 4.17 (b).

4.2.2. Proposed Improvement in Device Operation

Two versions of micro scanners are designed to exploit the capability of the present technology, as shown in Fig. 4.19. The device that is depicted in Fig. 4.19 (a) has a uniform thickness of t, consisting of two narrow beams, with a length of L_f and a width of W_f, supporting a rectangular mirror mass with a size of $W_m \times L_m$. The beams are clamped at both ends and tailored to have a mechanical torsion motion about the rotation axis at the fundamental resonance mode (f_R). The device shown in Fig. 4.19 (b) has the same planar geometry as the device given in Fig.4.19 (a), but both the starting substrate thickness and the local topography of the mirror is different. Table 4.2 summarizes the dimensions of the devices as well as the finite element simulation results for the fundamental mode frequencies.

Table 4.2. Dimensions and simulated resonance frequencies of the test devices.

Description	Device-1	Device-2
Thickness (t)	170 μm	200 μm
Mirror width (W_m)	3 mm	3 mm
Mirror length (L_m)	4 mm	4 mm
Flexure width (W_f)	320 μm	320 μm
Flexure length (L_f)	6 mm	6 mm
Resonance frequency (f_R)	4380 Hz	6173 Hz

The scanner works on the principle that the mirror deflects according to the Hooke's law, when there is an electromagnetic actuation force acting on the device. Deflection of the mirror is increased substantially at the resonance frequency due to the high mechanical quality factor. If a light beam is shined on the reflecting mirror, a 1D scan line which is orthogonal to the torsion movement can be projected on a desired target.

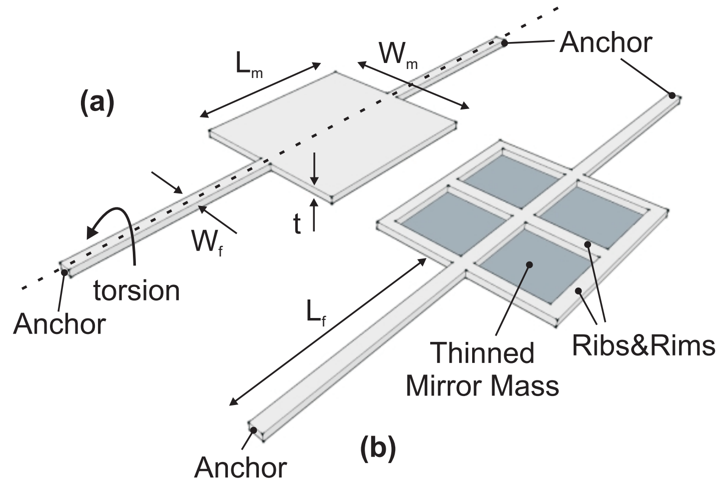

Figure 4.19. Schematic diagram of the targeted mirror structure (a) Device-1: a typical torsional micro-mirror with uniform thickness (b) Device-2: the proposed 1D micro-scanner with thinned mirror mass.

The mechanical computations to design such a micro-scanner are reported in Chapter 2. Following a similar design procedure, the dimensions of the device are determined for the targeted operation. Structural mechanics and frequency response behavior of the device is checked by finite element simulations as shown in Fig. 4.20,

where the torsional rotation at 4380 Hz is observed. In the inset of Fig.4.20, mode shape of the device operating at 4380 Hz can be seen.

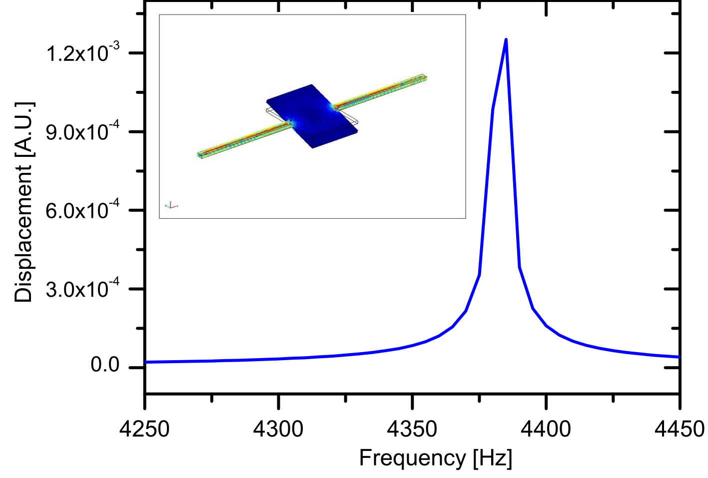

Figure 4.20. Finite element simulations of the designed micro-scanner showing the mode shape (inset) and the resonance peak of the torsional movement (fundamental mode) that occurs at 4380 Hz.

Increasing the resonance frequency of a 1D mirror is a major issue to attain a high number of resolvable pixels along the scan line. Resonance frequency of the torsional mode is given in Eq. 2.23. This resonance frequency can be increased by either increasing the stiffness or by reducing the effective moment of inertia. However, when stiffness is increased, the mechanical torque required to actuate the mirror also increases, leading to either higher power consumption or reduced scan angle. Therefore, it is preferred to reduce the mirror inertia to obtain a higher scan frequency as shown in Fig.4.19 (b). The moment of inertia of a generic 1D micro-mirror seen in Fig.4.19 (a) is given as

$$J_{m,u} = \frac{M_m}{12}\left(W_M^2 + t^2\right) \tag{4.3}$$

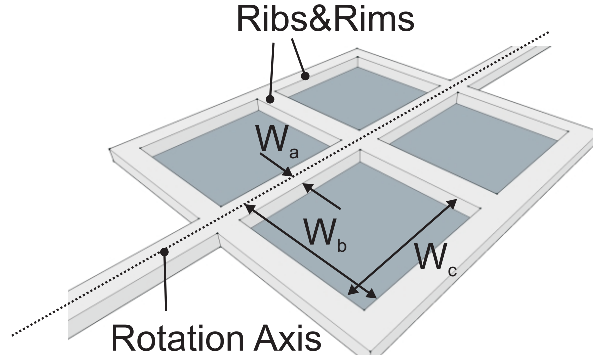

Figure 4.21. Close-up view of the thinned micro-mirror.

The moment of inertia of the thinned device can be computed as

$$J_{m,t} = J_{m,u} - \frac{4}{3} M_{m,t} \left(W_b^2 + W_a^2 + W_b W_a \right) \tag{4.4}$$

where, W_a is the width of the one of the thinned rectangular mass, W_a and W_b are the distances from the edges of the thinned region to the rotation axis of the scanner as depicted in Fig. 4.21 and having ρ as the density, $M_{m,t} = \rho t (W_b - W_a) W_c$ is the excluded mass of one thinned region. Therefore, with the help of the proposed fabrication method, shaping the device in the third axis and eventually increasing its resonance frequency by changing its moment of inertia becomes possible. In order to increase the integrity of the mirror and to reduce the dynamic deformation a cross-shaped rib and rims around the scanning mirror are used.

4.2.3. Experimental Results and Measurement

The proposed fabrication method is tested by implementing two steel micro-scanners: the device with a thinned mirror mass on a 200 μm thick steel starting substrate is processed by using the design explained above (Device-2). In order to make a comparison, the same design is also fabricated without thinning the mirror mass on a 170 μm thick steel substrate (Device-1). The electrode gap and the current density values of 3.25 cm and 3 A/cm^2 are employed through electrochemical etching, respectively. Fabricated steel micro-scanners can be seen in Fig. 4.22.

The mirror mass of the scanner in Fig. 4.22 (a) is thinned down for approximately 150 μm. As can be realized, a rim is deliberately formed around the mirror mass along with cross-ribs inside to minimize the dynamic mirror deformation.

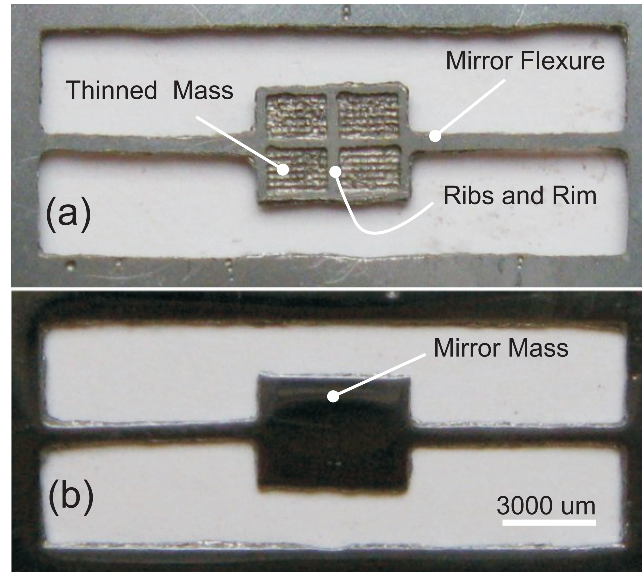

Figure 4.22. Closer view of the mirror masses of produced scanners (a) thinned device (b) unthinned device.

The bulk fabrication material (stainless steel 301) is a soft magnetic material. Thus, magnetic actuation can be directly used to exert torque on the mirror. The scanners are actuated by a stationary off-chip coil that provides a frequency dependent magnetic flux. As it is explained in Section 2.4, the flux created by the coil produces a magnetic moment that acts against the spring force resulting in deflection of the mirror. The frequency responses of the fabricated devices are plotted in Fig. 4.23.

The fundamental resonant mode of the unthinned steel mirror occurs at approximately 4210 Hz which is very close to finite element analysis result given in Fig. 4.20. This device has a quality factor of 420 in the ambient air. The torsional resonance frequency of the thinned version of the same device experiences a shift to 6060 Hz and it has a quality factor of 606. This indicates a 43% of absolute frequency shift. However, to make a fair comparison, if we consider the thickness difference between these two devices and set both of them to have an equal starting substrate thickness, we acquire a normalized frequency shift of 15%.

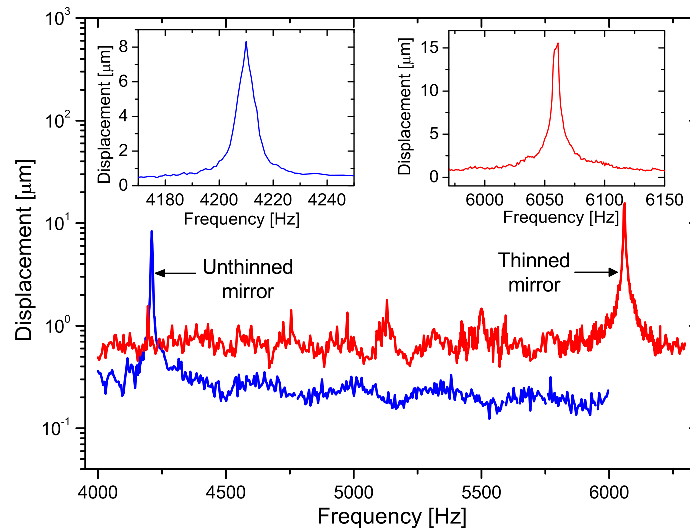

Figure 4.23. Frequency response of fabricated mirrors.

Since the resonance frequency is inversely proportional to the square root of the moment of inertia, there is an agreement between the theory and the experimental results shown in Fig. 4.23. Although the dynamics of the mechanical quality factor is heavily dependant on the damping and the vibration frequency, a first order approximation, assuming a mass-spring-damper model estimates an increase in the quality (Q) factor as the inertia is reduced for a fixed spring constant. Assuming a constant damping factor with respect to the frequency shift from 4210 Hz to 6060 Hz, experimental results show that the quality factor is increased by a factor of 1.45 for the thinned mass device. The ratio of the quality factors of device-1 and device-2 can be related to the ratio of the resonance frequencies.

4.2.4. Concluding Remarks on Self-Terminating Fabrication Method

An alternative, simple fabrication method which uses a single lithography step that is followed by electrochemical etching is presented. The proposed method enables patterning steel devices in the third axis and to form curved structures on the surface using the feature size dependent etch rates. The process is carefully tested and characterized by actually producing different micro-scanners. Scanner fabricated using the proposed method has reasonable etch uniformity with an etch rate of approximately 39 μm/min for HCl electrolyte and 41 μm/min for NaCl electrolyte, both measured

at the same electrode gap of 3 cm. The resonance frequency of the fundamental mode is increased approximately from 4210 Hz to 6060 Hz indicating a 43% of absolute frequency shift. Taking the thickness difference between the Device-1 and Device-2 into account, both devices are set to have equal starting substrate thicknesses, and a normalized frequency shift of 15% is calculated out of experimental data. Additionally, proposed method is batch fabrication compatible unlike traditional steel process methods such as electric discharge machining (EDM) or steel micro-milling. Such a fabrication process is especially useful for high resolution one dimensional and two dimensional micro-mirrors, where a thinned mirror mass and a set of thinned slow-scan suspensions result in a high fast-scan frequency and a low slow-scan frequency, respectively.

5. CONCLUSIONS AND FUTURE WORK

This research basically explored two different techniques mentioned to create scanner-based low-resolution projection display systems. In the first part of the thesis work a scanned 1D array of LEDs are used to create a 2D display. First solid-state LEDs and then polymer LEDs are integrated on a polymer (FR4) actuator. Proposed FR4 based displays have the advantage of having a low fundamental resonance frequency suitable to be used as refresh rate. Displacement at the slow-scan resonance enjoys the moderate quality factor of the mechanical structure. Simultaneous and precise control of this resonant movement along with the modulation of 1D LED array in perpendicular direction to the slow-scan axis enabled the generation a 2D images.

A scanner is fabricated using a Cu coated FR4 substrate. Magnetically actuated display entered into its fundamental resonant movement at approximately 99 Hz and produces a peak displacement of 2.45 mm at a drive power of 85 mW. A display resolution of 20×40 pixel on a physical size of 8 mm$\times$ 2.25 mm is acquired. When considering only the LED array, the proposed display consumed 14% more power compared to the conventional dot-matrix LED display of the same performance. However, when the advantage of using significantly less amount of LED devices is considered, it can be deduced that the present display offers a more reliable operation, in terms of less probable dead-pixel failure, easily controllable LED-to-LED variations. Furthermore, utilization of one-row of LED array reduces the cost arising from the usage of light sources. Finally, the display is proven to be quite robust in the tests which lasted approximately 3 million cycles with no significant change (below 5%) in the performance parameters such as the quality factor, the peak resonant displacement and the resonance frequency.

After the realization of a 2D display with solid-state LEDs, this time, a novel all-polymer integrated microsystem, which realize a 2D display by integrating a 1D array of PLEDs with a polymer scanner of microelectromechanical system and which uses the same operation principles is presented. Polymer scanner is fabricated again

on FR4 material with a double-sided process using lithography to pattern copper lines and laser micromachining to cut the scanner outline. PLEDs are fabricated on polyethylene terephthalate sheets. They have a thin-film structure of indium tin oxide, poly (3,4-ethylenedioxythiophene) poly (styrenesulfonate), poly [2-methoxy-5-(2'-ethyl-hexyloxy)-1,4-phenylene vinylene], and aluminum. Initial results showed that this technology has the potential to implement medium resolution low-cost 2D displays. Two essential parts of the display, the FR4 actuator and the PLED array, were fabricated by using inexpensive processes. Characterization results of the FR4 actuator showed that peak-to-peak deflection of 3.4 mm is possible without reaching the plastic-deformation limit. PLEDs start to emit light at 7.5 V. Each PLED has a luminance of 0.3 cd/m^2 at 13 V, consuming 1.1 mA current. Resulting integrated display was tested to implement basic functions of an imaging system, and according to the initial results, it is proven that there is a great potential for a novel all-polymer medium/low-resolution inexpensive display.

In the second part of thesis work, a one bidirectional raster-scanning mirror is used to create a 2D projection display. Proposed scanners are fabricated out of stainless steel 301 which is a soft magnetic material. A new fabrication alternative for steel micromachining using only one photomask and a single lithography step is proposed. With this new fabrication method a reasonable etch uniformity with an etch rate of 25 μm/min is obtained. A family of scanners are fabricated and two of these scanners are shown that they are capable of being used in the display applications. One device gave a maximum TOSA of 11.7° in the slow scan axis and 23.2° in the fast scan axis in its resonance modes (112 Hz for slow scan movement and 882 Hz for fast scan movement) at a drive power of 42 mW and 30.6 mW, respectively.

Second device that is fabricated out of stainless steel generated a fast scan TOSA of 5.9° and a slow scan TOSA of 76° for drive powers of 39 mW and 37 mW, respectively. The scanner devices are operated in ambient air and resulting mechanical quality factors for the scan modes are sufficient ($Q > 100$) to have low power consumption. When a non-resonant actuation is used for the slow-scan, refresh rate, the ratio between fast and slow scan frequencies becomes 14.7, which implies that one can

write approximately 15 lines in the vertical direction using the present device as a 2D display. Experiments showed that the drive power is approximately proportional to the square of the total optical scan angle. After the fabrication, a simple two dimensional display system is constructed by using the fabricated steel scanner and accompanying driving and signal processing circuitry. Obtained images showed the potential of the steel scanners in imaging applications.

However, fabricated and tested scanner systems showed that their performance are not enough to create 2D projection displays with higher resolution values. Therefore, previously proposed fabrication method is ameliorated further and a gimballed mirror based system is fabricated out of the stainless steel to create a raster-scanned 2D display together with this novel, self-terminating electrochemical etch process. This process uses single mask photolithography, and the etching step is terminated automatically, which at the same time enables the depth profile shaping of the fabricated structure. The proposed process is characterized and then used to fabricate two versions of 1D steel micro-scanners, one being with selective thinning of the predefined parts and one being without thinning.

The fabricated devices are characterized and compared with respect to their resonance frequencies and mechanical quality factors. The thickness of the starting substrate is selectively thinned down in order to decrease the mass of the mirror and eventually to increase the resonance frequency of the fundamental mode. Scanner fabricated using the proposed method has reasonable etch uniformity with an etch rate of approximately 39 μm/min for HCl electrolyte and 41 μm/min for NaCl electrolyte, both measured at the same electrode gap of 3 cm. The resonance frequency of the fundamental mode is increased approximately from 4210 Hz to 6060 Hz indicating a 43% of absolute frequency shift. Taking the thickness difference between the first and second device into account, both devices are set to have equal starting substrate thicknesses, and a normalized frequency shift of 15% is calculated out of experimental data. Additionally, proposed method is batch fabrication compatible. Such a fabrication process is especially useful for high resolution one dimensional and two dimensional micro-mirrors, where a thinned mirror mass and a set of thinned slow-scan suspensions

result in a high fast-scan frequency and a low slow-scan frequency, respectively.

Several different things can be described as future work. Firstly, it is possible to fabricate a light-source integrated polymer composite scanner based display with higher-resolution by integrating LED driver integrated circuits (ICs) on actuators. Initial tests are completed using MAXIM's 6949 diver IC. This LED driver uses I^2C interface to drive the LED array through an FPGA development board. It is possible to drive 10 LEDs using just 3 lines of electrical copper paths. 4 of these drivers are put on an polymer composite actuator to perform the job of driving a 1D LED array consisting of 40 light-sources. This job is accomplished using again 20 copper electrical path using a very similar design to the previous one. MAX6949 IC has an area of $3mm \times 3mm$ and enables pulse width modulation. However, the driving clock frequency of this IC was not sufficient for the targeted application. It is possible to increase the vertical resolution of the display up to 100 by designing and integrating an aim specific integrated circuit (ASIC) with faster clock frequencies. Having many drivers on the tip of the actuator also decreases the resonance frequency of the structure regarding Eq. 2.28. To compensate this decrease, one should scale down and tailor the structure accordingly, which at the end will create a trade-off by putting a constraint on the area and decreasing the vertical displacement of the structure.

Secondly, as a future work, light-source integrated polymer composite scanners can be and should be designed in a way to produce color images. This can be accomplished using LEDs with different emission wavelength and a different kind of integration scheme. Alternative methods of accomplishing this job are proposed but not tested during this thesis work. One of them involve purchasing and integrating a R,G and B LED arrays on the actuator. Simultaneous and precise control of light-sources and the actuator can definitely create a color display.

One other job that can be done in the future is the usage of SS420 material to fabricate 2D laser scanning stainless steel micro-mirrors SS420 has better magnetic properties than the preferred fabrication material SS301. One can thin-down the structure properly using the proposed self-terminating electrochemical etch method and cut

it using electric discharge machining to define better and uniform profile walls. With an effective mirror design it is possible to create a VGA resolution projection display.

APPENDIX A: FPGA Code

```
library IEEE;
use IEEE.STD_LOGIC_1164.ALL;
use IEEE.STD_LOGIC_ARITH.ALL;
use IEEE.STD_LOGIC_UNSIGNED.ALL;

entity test is
    Port ( CLK_50MHZ:in STD_LOGIC;
    ENABLE:in STD_LOGIC;
    LED1:out STD_LOGIC;
    oSCL1,oSCL2,oSCL3,oSCL4:out STD_LOGIC;
    oSDA1,oSDA2,oSDA3,oSDA4:inout STD_LOGIC;
    oOSCL:out STD_LOGIC
);
end test;

architecture Behavioral of test is
type td_vec is array (0 to 4) of STD_LOGIC_VECTOR(0 to 29);
signal sda_v:td_vec:=(
    ("001000000Z00010000Z00000001Z01"),
    ("001000000Z00001000Z00000111Z01"),
    ("001000000Z00000111Z00011111Z01"),
    ("001000000Z00000110Z01111111Z01"),
    ("001000000Z00000101Z11110000Z01")
);

signal main_counter:integer range 0 to 50000000:=200;
signal LED_1:STD_LOGIC:='0';
signal ioSCL:STD_LOGIC:='1';
signal ioSDA:STD_LOGIC:='0';
```

```
begin
--Checker modulation test
checker: process(CLK_50MHZ)
    variable count:integer range 0 to 1000:=0;
    variable iic_count:integer range 0 to 100:=0;
    variable sda_count:integer range 0 to 100:=0;
    variable scl_count:integer range 0 to 100:=0;
    variable reset:boolean:=false;
    variable command_no:integer range 0 to 10:=0;
    variable all_count:integer range 0 to 50000000:=0;
    variable wait_count:integer range 0 to 50000000:=0;
    variable total_count:integer range 0 to 1000000:=0;
    variable wait_for_a_while:boolean:=false;

begin
    if( CLK_50MHZ='1' and CLK_50MHZ'event) then
    if (enable = '1') then
    if count <= main_counter then
    count := count + 1;
else
----------------------------------------------------------------
    if (all_count >= 5 AND iic_count < 29) then
    if (scl_count >= 1) then
        ioSCL<= not ioSCL;
        scl_count := 0;
    else
        scl_count := scl_count + 1;
    end if;
    else
        ioSCL <='1';
    end if;
```

```
----------------------------------------------------------------
if(sda_count >= 3) then
if( command_no < 5) then
    ioSDA<= sda_v(command_no)(iic_count);
else
    ioSDA<='1';
end if;
    sda_count := 0;
if (iic_count>=29) then
if( command_no < 4) then
    command_no:=command_no+1;
else
    command_no:=6;
end if;
    wait_for_a_while:=true;
    iic_count:=0;
    sda_count:=1;
    scl_count:=0;
    all_count:=0;
else
    iic_count := iic_count + 1;
end if;
else
    sda_count := sda_count + 1;
end if;
----------------------------------------------------------------
    all_count:=all_count + 1;
    total_count:=total_count + 1;
    count:=0;
end if;
else
    LED_1<='0';
```

```
    ioSDA<='1';
    ioSCL<='1';
    count:=0;
    iic_count:=0;
    sda_count:=0;
    scl_count:=0;
    all_count:=0;
end if;
end if;
end process checker;
    oSCL1 <= ioSCL;
    oSCL2 <= ioSCL;
    oSCL3 <= ioSCL;
    oSCL4 <= ioSCL;
    oSDA1 <= ioSDA;
    oSDA2 <= ioSDA;
    oSDA3 <= ioSDA;
    oSDA4 <= ioSDA;
LED1<=LED_1;
    oOSCL <= '0';
end Behavioral;
```

APPENDIX B: List of Publications

In the course of Ph.D. studies, following journal and conference papers have been published.

B.1. Journal Publications

1. A.D. Yalcinkaya, **Y.D. Gokdel** and B. Sarioglu, "One Dimensional LED Array Integrated FR4 Scanner for 2D Imaging" *Sensors and Actuator A: Physical*, vol. 168, pp. 195-201, Jul. 2011.
2. **Y.D. Gokdel**, S. Mutlu and A.D. Yalcinkaya, "Self-Terminating Electrochemical Etching of Stainless Steel for the Fabrication of Micro-Mirrors", *J. Micromechanics and Microengineering*, Vol.20, No.9, 2010.
3. **Y.D. Gokdel**, A.O. Sevim, S. Mutlu and A.D. Yalcinkaya, "Polymer MEMS Based Optoelectronic Display", *IEEE Transactions on Electron Devices*, Vol. 57, Issue 1, pg. 145-152, Jan. 2010.
4. **Y.D. Gokdel**, B. Sarioglu, S. Mutlu and A.D. Yalcinkaya, "Design and Fabrication of Two-Axis Micromachined Steel Scanners", *J. Micromechanics and Microengineering*, Vol. 19, No. 7, pg. 1-8, July 2009.

B.2. Conference Publications

1. **Y.D. Gokdel**, B.Sarioglu and A.D. Yalcinkaya, "2D Imaging with 1D LED Array Integrated FR4 Actuator", accepted to *Transducers 2011*, 5-9 June 2011, Beijing, China.
2. **Y.D. Gokdel**, A.O. Sevim, B. Kucukakarsu, S. Mutlu and A.D. Yalcinkaya, "PLED integrated FR4 MEMS Display", *The 22nd Annual Meeting of the IEEE Photonics Society*, 4-8 October 2009, Antalya, Turkey.
3. **Y.D. Gokdel**, B. Sarioglu, S. Mutlu, A.D. Yalcinkaya, "Two-Axis Micromachined Steel Scanners", *Proceedings of MME 2008*, pp. 93-97, September 28-30 2008, Aachen, Germany.

4. B. Sarioglu, **Y.D. Gokdel**, A.D. Yalcinkaya, "1.5D Display with FR4 Actuator and LEDs", *Proceedings of Eurosensors 2008*, September 7-10 2008, Dresden, Germany.
5. **Y.D. Gokdel**, B. Sarioglu, A.D. Yalcinkaya, "LED Integrated Miniaturized Polymer MEMS Display", *Proceedings of IEEE PRIME 2008*, pp. 93-97, June 22-25 2008, Istanbul, Turkey.

REFERENCES

1. Motamedi, M., “Merging Microoptics with Micromechanics:MOEM Devices”, *Proc. SPIE*, Vol. CR49, pp. 303–328, 1993.

2. Kessel, P. V., L. Hornbeck, R. Meier and M. Douglass, “A MEMS-Based Projection Display”, *Proc. IEEE*, Vol. 86, No. 8, pp. 1687–1704, Aug. 1998.

3. Bloom, D., “Grating Light Valve: Revolutionizing Display Technology”, *Proc. SPIE Projection Displays III*, Vol. 3013, pp. 165–171, 1997.

4. Perreault, J. A., T. Bifano, B. Levine and M. Horenstein, “Adaptive Optic Correction Using Microelectromechanical Deformable Mirrors”, *Opt. Eng.*, Vol. 41, pp. 561–566, 2002.

5. Chen, R., H. Nguyen and M. Wu, “A High-Speed Low-Voltage Stress-Induced Micromachined 22 Optical Switch”, *IEEE Photonic Tech. L.*, Vol. 11, No. 11, pp. 1396–1398, Nov. 1999.

6. Ataman, C. and H. Urey, “Compact Fourier Transform Spectrometers using FR4 Platform”, *Sensors and Actuators: A. Physical*, Vol. 151, pp. 9–16, 2009.

7. Ferhanoglu, O., H. Seren, S. Lttjohann and H. Urey, “Lamellar Grating Optimization for Fourier Transform Spectrometers”, *Optics Express*, Vol. 17, pp. 21289–21301, 2009.

8. Kumar, K., K. Hoshino and X. Zhang, “Handheld Subcellular-Resolution Single-Fiber Confocal Microscope Using High-Reflectivity Two-Axis Vertical Combdrive Silicon Microscanner”, *Biomedical Microdevices*, Vol. 10, pp. 653–660, 2008.

9. Hofmann, U., S. Muehlmann, M. Witt, K. Doerschel, R. Schuetz and B. Wagner, “Electrostatically Driven Micromirrors for a Miniaturized Confocal Laser Scan-

ning Microscope", *Proc. SPIE*, Vol. 3878, p. 2938, Miniaturized Systems with Micro-Optics and MEMS, Santa Clara, CA, Sep. 1999.

10. Yalcinkaya, A., O. Ergeneman and H. Urey, "Polymer Magnetic Scanner for Barcode Reader Applications", *Sensors and Actuators: A. Physical*, Vol. 135, No. 1, pp. 236–243, 2007.

11. Conant, R., P. Hagelin, U. Krishnamoorthy, M. Hart, O. Solgaard, K. Lau and R. Muller, "A Raster-Scanning Full-Motion Video Display Using Polysilicon Micromachined Mirrors", *Sensors and Actuators A*, Vol. 83, pp. 291–296, 2000.

12. Lewis, J., "In the Eye of the Beholder", *IEEE Spectrum*, Vol. 41, pp. 21–28, 2004.

13. Hornbeck, L., "From Cathode Rays to Digital Micromirrors: A History of Electronic Projection Display Technology", *Texas instruments technical journal*, pp. 7–44, July-September 1998.

14. Zworykin, V., "Television with Cathode-Ray Tube for Receiver", *Radio Engineering*, Vol. IX, pp. 38–41, 1929.

15. Abramson, A., *Electronic Motion Pictures*, Arno Press, New York, 1974.

16. Glenn, W., "Principles of Simultaneous-Color Projection Television Using Fluid Deformation", *J. of SMPTE*, Vol. 79, pp. 788–794, 1970.

17. Bauman, E., "The Fischer Large-Screen Projection System", *J. of SMPTE*, Vol. 60, pp. 344–356, 1953.

18. Robinson, D., "The Supersonic Light Control and Its Application to Television with Special Reference to the Scophony Television Receiver", *Proc. IRE*, pp. 483–486, Aug. 1939.

19. Thomas, R., J. Guldberg, H. Nathanson and P. Malmberg, "The Mirror Matrix Tube: A Novel Light Valve For Projection Displays", *IEEE Trans. Electron*

Devices, Vol. 22, No. 9, pp. 765–775, 1975.

20. Petersen, K., “Micromechanical Light Modulator Array Fabricated On Silicon”, *App. Phys. Letter*, Vol. 31, No. 18, pp. 521–523, 1977.

21. Hagelin, P. and O. Solgaard, “Optical Raster Scanning Displays Based on Surface-Micromachined Polysilicon Mirrors”, *IEEE Journal of Selected Topics in Quantum Electronics*, Vol. 5, No. 1, pp. 1233–1235, 1999.

22. Torashima, K., T. Teshima, Y. Mizoguchi, S. Yasuda, T. Kato, Y. Shimda and T. Yagi, “A Micro-Scanner with Low Power Consumption Using Double Coil Layers on a Permalloy Film”, *Proc. IEEE-LEOS Conf. Opt. MEMS*, pp. 192–193, Takamatsu City, Japan, May 2004.

23. Yang, H.-A., T.-L. Tang, S. Lee and W. Fang, “A Novel Coilless Scanning Mirror Using Eddy Current Lorentz Force and Magnetostatic Force”, *J.MEMS*, Vol. 16, No. 3, pp. 511–520, Jun. 2007.

24. Wang, W.-C. and P. Reinhall, “Scanning Polymeric Waveguide Design of a 2-D Display System”, *IEEE J. Disp. Technol.*, Vol. 4, pp. 28–38, 2008.

25. Yalcinkaya, A. D., H. Urey, T. Montague, D. Brown and R. Sprague, “Two-axis electromagnetic Microscanner for High Resolution Displays”, *J. Microelectromech. Syst.*, Vol. 15, No. 4, p. 786794, Aug. 2006.

26. Isikman, S. O., O. Ergeneman, A. Yalcinkaya and H. Urey, “Modeling and Characterization of Soft Magnetic Film Actuated 2-D Scanners”, *J. Sel. Top. Quantum Elec.*, Vol. 12, pp. 283–289, Mar./Apr. 2007.

27. Yan, J., S. Luanava and V. Casasanta, “Magnetic Actuation for MEMS Scanners for Retinal Scanning Displays”, *SPIE Proceedings 4895, MOEMS Display and Imaging Systems*, San Jose, CA, Jan. 2003.

28. Ji, C.-H., M. Choi, S.-C. Kim, K.-C. Song, J.-U. Bu and H.-J. Nam, “Electromag-

netic Two-Dimensional Scanner Using Radial Magnetic Field", *J.MEMS*, Vol. 16, No. 4, pp. 989–996, Aug. 2007.

29. http://www.microvision.com.

30. Urey, H., D. Wine and T. Osborn, "Optical Performance Requirements for MEMS-Scanner Based Microdisplays", *Proc. SPIE*, Vol. 4178, pp. 176–185, Conf. on MOEMS and Miniaturized Systems, Santa Clara, California, 2000.

31. M.Sayinta, S. Isikman and H. Urey, "Scanning LED Array Based Volumetric Display", *Proc. of*, p. 2938, 3DTV Conference, Istanbul, Turkey, Jun. 2008.

32. A.Nakai, K. M., K.Hoshino and I. Shimoyama, "Double-sided Scanning Micromirror Array for Autostereoscopic Display", *Sensors and Actuators: A. Physical*, Vol. 135, pp. 80–85, 2007.

33. Gokdel, Y., A. Sevim, S. Mutlu and A. Yalcinkaya, "Polymer MEMS Based Optoelectronic Display", *IEEE Trans. on Electron Devices*, Vol. 57, No. 1, pp. 145–152, Jan. 2009.

34. Yalcinkaya, A., Y. Gokdel and B. Sarioglu, "One-Dimensional LED Array Integrated Polymer Composite Scanner for 2D Imaging", *Sensors and Actuators A: Physical*, Vol. 168, No. 1, pp. 195–201, Jul. 2011.

35. Gokdel, Y., B. Sarioglu, S. Mutlu and A. Yalcinkaya, "Design and Fabrication of Two-Axis Micromachined Steel Scanners", *J. Micromech. Microeng.*, Vol. 19, No. 7, pp. 1–8, Jul. 2009.

36. Gokdel, Y., S. Mutlu and A. Yalcinkaya, "Self-Terminating Electrochemical Etching of Stainless Steel for the Fabrication of Micro-Mirrors", *J. Micromech. Microeng.*, Vol. 20, No. 9, 2010.

37. Urey, H., D. W. Wine and J. R. Lewis, "Scanner Design and Resolution Tradeoffs for Miniature Scanning Displays", *Proc. SPIE*, Vol. 3636, pp. 60–68, Conference

on Flat Panel Displays, San Jose, California, Jan. 1999.

38. Solgaard, O., *Photonic Microsystems: Micro and Nanotechnology Applied to Optical Devices and Systems*, Cambridge University Press, 1th edn., 2008.

39. Hagelin, P., *Micromachined Mirrors for Raster-Scanning Displays and Optical Fiber Switches*, Ph.D. Thesis, UC Davis, 2000.

40. Motamedi, M. E. (Editor), *MOEMS: Micro-Opto-Electro-Mechanical Systems*, SPIE Publications, Washington, USA, 2005.

41. Urey, H., "Torsional MEMS Scanner Design for High-Resolution Display Systems", *Proc. SPIE*, Vol. 4773, pp. 27–37, Optical Scanning II, Seattle, Washington, Jul. 2002.

42. Dickensheets, D., *A Microfabricated Scanning Confocal Optical Microscope For In Situ Imaging*, Ph.D. Thesis, Stanford University, 1997.

43. G.Marshall (Editor), *Optical Scanning*, Marcel Dekker, New York, 1991.

44. Young, W. and R. Budynas, *Roark's Formulas for Stress and Strain*, McGraw-Hill Professional, 7th edn., 2001.

45. Muhlstein, C., S. Brown and R. Ritchie, "High-Cycle Fatigue of Single-Crystal Silicon Thin Films", *J. MEMS*, Vol. 10, No. 4, pp. 593–599, 2001.

46. Timoshenko, S. and J. Goodier, *Theory of Elasticity*, McGraw-Hill, 3rd edn., 1970.

47. Liu, C., *Foundations of MEMS*, Prentice Hall, Upper Saddle River, New Jersey, 2005.

48. Maluf, N. and K. Williams, *An Introduction to Microelectromechanical Systems Engineering*, Artech House, Norwood,MA, 2nd edn., 2004.

49. Kovacs, G., *Micromachined Transducers Sourcebook*, McGraw-Hill, 1998.

50. Beer, F., E. Johnston and J. DeWolf, *Mechanics of Materials*, McGraw-Hill, 4th edn., 2005.

51. Urey, H., C. Kan and W. Davis, "Vibration Mode Frequency Formulae for Micromechanical Scanners", *J. Micromech. Microeng.*, Vol. 15, pp. 1713–1721, 2005.

52. Jain, A., A. Kopa, P. Yingtian, G. Fedder and X. Huikai, "Two-Axis Electrothermal Micromirror for Endoscopic Optical Coherence Tomography", *IEEE J. Sel. Top. Quantum Electron.*, Vol. 10, No. 3, pp. 636–642, May-Jun 2004.

53. Torun, H., K. Sarangapani and F. Degertekin, "Fabrication and Characterization of Micromachined Active Probes With Polymer Membranes for Biomolecular Force Spectroscopy", *J. MEMS*, Vol. 19, No. 5, pp. 1021–1028, Oct. 2010.

54. Miyajima, H., N. Asaoka, M. Arima, Y. Minamoto, K. Murakami, K. Tokuda and K. Matsumoto, "A durable, Shock-resistant Electromagnetic Optical Scanner with Polyimide-Based H inges", *J. Microelectromech. Syst.*, Vol. 10, No. 3, pp. 418 – 424, 2001.

55. Hendrickx, N., J. V. Erps, G. V. Steenberge, H. Thienpont, and P. V. Daele, "Laser Ablated Micromirrors for Printed Circuit Board Integrated Optical Interconnections", *IEEE Photonics Technology Letters*, Vol. 19, No. 11, pp. 822–824, Jun. 2007.

56. Urey, H., S. Holmstrom and A. Yalcinkaya, "Electromagnetically Actuated FR4 Scanners", *IEEE Photonics Technology Letters*, Vol. 20, No. 1, pp. 30–33, Jan. 2008.

57. Kaajakari, V., *Practical MEMS*, Small Gear Publishing, 2009.

58. Judy, J., *Batch-Fabricated Ferromagnetic Microactuators with Silicon Flexures*, Ph.D. Thesis, UC Berkeley, 1996.

59. Petersen, K., “Silicon as a Mechanical Material”, *Proc. IEEE*, Vol. 70, No. 5, pp. 420–457, May 1982.

60. Callister, W., *Material Science and Engineering, An Introduction*, John Wiley and Sons, New York, 4th edn., 1997.

61. Cugat, O., J. Delamare and G. Reyne, “Magnetic Micro-Actuators and Systems (MAGMAS)”, *IEEE Tran. on Magnetics*, Vol. 39, No. 5, pp. 3607 – 3612, Nov. 2003.

62. Bell, D., T. Lu, N. Fleck and S. Spearing, “MEMS actuators and sensors: observations on their performance and selection for purpose”, *J. Micromech. Microeng.*, Vol. 15, No. 7, pp. 153–164, Jun. 2005.

63. Bernstein, J., W. Taylor, J. Brazzle, C. Corcoran, G. Kirkos, J. Odhner, A. Pareek, M. Waelti and M. Zai, “Electromagnetically Actuated Mirror Array for Use in 3-D Optical Switching Applications”, *J. Microelectromech. Syst.*, Vol. 13, No. 3, pp. 526–535, Jun. 2004.

64. Liu, C. and Y. W. Yi, “Micromachined Magnetic Actuators Using Electroplated Permalloy”, *IEEE Tran. on Magnetics*, Vol. 35, No. 3, pp. 1976–1985, May 1999.

65. Liu, C., T. Tsao, G. bin Lee, J. T. S. Leu, Y. W. Yi, Y. chong Tai and C. ming Ho, “Out-of-Plane Magnetic Actuators with Electroplated Permalloy for Fluid Dynamics Control”, *Sensors and Actuators A:Physical*, Vol. 78, No. 3, pp. 190–197, May 1999.

66. Yi, Y. W. and C. Liu, “Magnetic Actuation of Hinged Microstructures”, *J. Microelectromech. Syst.*, Vol. 8, No. 1, pp. 10–17, Mar. 1999.

67. Cho, H. and C. Ahn, “A Bidirectional Magnetic Microactuator Using Electroplated Permanent Magnet Arrays”, *J. Microelectromech. Syst.*, Vol. 11, 2002.

68. Ahn, C., Y. Kim and M. Allen, “A Planar Variable Reluctance Magnetic Micro-

motor with Fully Integrated Stator and Coils", *J. Microelectromech. Syst.*, Vol. 2, No. 4, pp. 165–173, Dec. 1993.

69. Ruan, M., J. Shen and C. Wheeler, "Latching Micromagnetic Relays", *J. Microelectromech. Syst.*, Vol. 10, No. 4, pp. 511–517, Dec. 2001.

70. Wagner, B., M. Kreutzer and W. Benecke, "Permanent Magnet Micromotors on Silicon Substrates", *J. Microelectromech. Syst.*, Vol. 2, No. 1, pp. 23–29, 1993.

71. Spaldin, N., *Magnetic Materials, Fundamentals and Device Applications*, Springer, New York,NY, 1th edn., 2003.

72. http://vtuphysics.blogspot.com/.

73. Tilmans, H. A., "Equivalent Circuit Representation of Electromechanical Transducers: I. Lumped-Parameter Systems", *J. Micromech. Microeng.*, Vol. 6, pp. 157–176, 1996.

74. Senturia, S. D., *Microsystem Design*, Springer, 2000.

75. Judy, J. W. and R. S. Muller, "Magnetic Microactuation of Torsional Polysilicon Structures", *Sensors and Actuators A: Physical*, Vol. 53, No. 1-3, pp. 392–397, May 1996.

76. Judy, J. W. and R. S. Muller, "Magnetically Actuated Addressable Microstructures", *J. Microelectromech. Syst.*, Vol. 6, No. 3, pp. 249–256, 1997.

77. Isikman, S., *Electromagnetically Actuated Optical Micro-Mechatronic Systems Integrated on PCB*, Master's Thesis, Koc University, July 2008.

78. Judy, J., R. Muller and H. Zappe, "Magnetic Microactuation of Polysilicon Flexure Structures", *J. MEMS*, Vol. 4, No. 4, pp. 162–169, Dec. 1995.

79. http://www.supermagnete.de.

80. Kijima, Y., N. Asai, N. Kishii and S. Tamura, “RGB Luminescence from Passive-Matrix Organic LEDs”, *IEEE Trans. Electron Devices*, Vol. 44, No. 8, pp. 1222–1228, Aug. 1997.

81. Mizukami, M., N. Hirohata, T. Iseki, K. Ohtawara, T. Tada, S. Yagyu, T. Abe, T. Suzuki, Y. Fujisaki, Y. Inoue, S. Tokito and T. Kurita, “Flexible AM OLED Panel Driven by Bottom-Contact OTFTs”, *IEEE Electron Device Lett.*, Vol. 27, No. 4, pp. 249–251, Apr. 2006.

82. Wen, S.-W., M.-T. Lee and C. H. Chen, “Recent Development of Blue Fluorescent OLED Materials and Devices”, *J. Display Tech.*, Vol. 1, No. 1, pp. 90–99, Sep. 2005.

83. Zhou, L., A. Wanga, S.-C. Wu, J. Sun, S. Park and T. N. Jackson, “All-Organic Active Matrix Flexible Display”, *Appl. Phys. Lett.*, Vol. 88, No. 8, p. XXX, Feb. 2006.

84. Baek, J. H., M. Lee, J. H. Lee, H. S. Pae, C. J. Lee, J. T. Kim, C. S. Choi, H. K. Kim, T. J. Kim and H. K. Chung, “A Current-Mode Display Driver IC Using Sample-and-Hold Scheme for QVGA Full-Color AMOLED Displays”, *IEEE J. Solid-State Circuits*, Vol. 41, No. 12, p. 29742982, Dec. 2006.

85. Ashtiani, S. J. and A. Nathan, “A Driving Scheme for Active-Matrix Organic Light-Emitting Diode Displays Based on Feedback”, *J. Display Technol*, Vol. 2, No. 3, pp. 258–264, Sep. 2006.

86. Apte, R. B., *Grating Light Valves For High Resolution Displays*, Ph.D. Thesis, Stanford University, 1994.

87. Schubert, E., *Light-Emitting Diodes*, Cambridge University Press, New York, 2nd edn., 2006.

88. Lun, W.-K., K. Loo, S.-C. Tan, Y. Lai and C. Tse, “Bilevel Current Driving

Technique for LEDs", *IEEE Transactions on Power Electronics*, Vol. 24, No. 12, pp. 2920–2932, 2009.

89. http://www.bobblick.com/techref/projects/propclock/propclock.html.

90. Sevim, A. O. and S. Mutlu, "Post-Fabrication Electric Field and Thermal Treatment of Polymer Light Emitting Diodes and Their Photovoltaic Responses", *Org. Electron.*, Vol. 10, No. 1, p. 1826, Feb. 2009.

91. Burroughes, J. H., D. D. C. Bradley, A. R. Brown, R. N. Marks, K. Mackay, R. H. Friend, P. L. Burns and A. B. Holmes, "Light-Emitting Diodes Based on Conjugated Polymers", *Nature*, Vol. 347, No. 6293, p. 539541, Oct. 1990.

92. Brown, P. J., H. Sirringhaus and R. H. Friend, "Electro-Optical Characterization of Field Effect Devices with Regioregular Poly-Hexylthiophene Active Layers", *Synth. Met.*, Vol. 101, No. 1, p. 557560, Oct. 1999.

93. Drury, C. J., C. M. J. Mutsaers, C. M. Hart, M. Matters and D. M. de Leeuw, "Low-Cost All-Polymer Integrated Circuits", *Appl. Phys. Lett.*, Vol. 73, No. 1, p. 108110, Jul. 1998.

94. Mutlu, S. and I. Haydaroglu, "Realization of Polymer Charge Pump Circuits Using Polymer Semiconductors", *Org. Electron.*, Vol. 12, No. 2, pp. 312–321, 2011.

95. Yu, G. and A. J. Heeger, "High Efficiency Photonic Devices Made With Semiconducting Polymers", *Synth. Met.*, Vol. 85, No. 1, p. 11831186, Mar. 1997.

96. Yu, G. and A. J. Heeger, "Recent Developments in Polymer MEMS", *Adv. Mater.*, Vol. 19, No. 22, p. 37833790, 2007.

97. Forrest, S., P. Burrows and M. Thompson, "The dawn of organic electronics", *IEEE Spectr.*, Vol. 37, No. 8, p. 2934, Aug. 2000.

98. Uhlir, A., “Electrolytic Shaping of Germanium and Silicon”, *J. Bell Tech.*, Vol. 35, pp. 333–347, 1956.

99. Datta, M. and D. Landolt, “Fundamental Aspects and Applications of Electrochemical Microfabrication”, *Electrochim. Acta*, Vol. 45, pp. 2535–2558, 2000.

100. Kim, B., S. Ryu, D. Choi and C. Chu, “Micro Electrochemical Milling”, *J. Micromech. Microeng.*, Vol. 15, pp. 124–129, 2005.

101. Kirchner, V., L. Cagnon, R. Schuster and G. Ertl, “Electrochemical Machining of Stainless Steel Microelements with Ultrashort Voltage Pulses”, *Appl. Phys. Lett.*, Vol. 79, pp. 1721–1723, 2001.

102. Richardson, M. and Y. Gianchandani, “Achieving Precision in High Density Batch Mode Micro-Electro-Discharge Machining”, *J. Micromech. Microeng.*, Vol. 18, p. 015002, 2008.

103. Akedo, J., J.-H. Park and H. Sato, “High-Speed Metal-Based Optical Microscanners Using Stainless-Steel Substrate and Piezoelectric Thick Films Prepared by Aerosol Deposition Method”, *Sensors Actuators A*, Vol. 135, p. 8691, 2007.

104. West, A., C. Madore, M. Matlos and D. Landolt, “Shape Changes During Through-Mask Electrochemical Micromachining of Thin Metal Films”, *J. Electrochem. Soc.*, Vol. 139, No. 2, p. 499506, 1992.

105. Mineta, T., “Electrochemical Etching of a Shape Memory Alloy Using New Electrolyte Solutions”, *J. Micromech. Microeng.*, Vol. 14, pp. 76–80, 2004.

106. Wine, D., M. Helsel, L. Jenkins, H. Urey and T. Osborn, “Performance of a Biaxial MEMS-Based Scanner for Microdisplay Applications”, *Proc. SPIE*, Vol. 4178, pp. 186–196, Conf. on MOEMS and Miniaturized Systems, San Clara, California, 2000.

107. Bustillo, J., R. Howe and R. Muller, “Surface Micromachining for Microelectrome-

chanical Systems", *Proc. IEEE*, Vol. 86, pp. 1552–1574, 1998.

108. Guckel, H., "High Aspect Ratio Micromachining via Deep X-ray Lithography", *Proc. IEEE*, Vol. 86, pp. 1586–1593, 1998.

109. Han, M., W. Lee, S.-K. Lee and S. Lee, "3D Microfabrication with Inclined/Rotated UV Lithography", *Sensors Actuators A*, Vol. 111, pp. 14–20, 2004.

110. A, A. B., H. Lorenz and P. Renaud, "3D Microfabrication by Combining Microstereolithograpy and Thick Resist UV Lithography", *Sensors Actuators A*, Vol. 73, p. 1423, 1999.

111. P.K. Kim, M. K. and G. Lim, "3D Glass Fabrication Utilizing Electric Field and Heat Treatment Induced Image Mirroring", *Sensors Actuators A*, Vol. 139, pp. 287–292, 2007.

112. Kondo, T., K. Yamasaki, S. Juodkazis, S. Matsuo, V. Mizeikis and H. Misawa, "Three Dimensional Microfabrication by Femtosecond Pulses in Dielectrics Thin Solid Films", *Thin Solid Films*, Vol. 550, No. 6, p. 453454, 2004.

113. Cohen, A., G. Zhang, F. Tseng, U. Frodis, F. Mansfield and P. Will, "EFAB: Low Cost Automated Electrochemical Batch Fabrication of Arbitrary 3D Microstructures", *Proc. SPIE*, Vol. 3874, p. 236247, 1999.

114. Chou, T. and K. Najafi, "Fabrication of Out of Plane Curved Surfaces in Si by Utilizing RIE Lag", *Proc. IEEE*, pp. 145–148, 15th Int. Conf. Micro Electro Mechanical Systems (MEMS), Las Vegas, USA, 2002.